OPTOFLUIDICS FOR PROGRAMMABLE MATTER AND SOLAR-POWERED MOBILE MICROFLUIDICS FOR GLOBAL HEALTH

A Dissertation

Presented to the Faculty of the Graduate School

of Cornell University

In Partial Fulfillment of the Requirements for the Degree of

Doctor of Philosophy

by

Li Jiang

May 2014

OPTOFLUIDICS FOR PROGRAMMABLE MATTER AND SOLAR-POWERED MOBILE MICROFLUIDICS FOR GLOBAL HEALTH

Li Jiang, Ph. D.

Cornell University 2014

During my PhD studies I have worked on developing a number of optofluidics-based technologies with a primary emphasis on creating systems that maintain a relatively simple design and infrastructure while achieving a high level of functionality in their ability to perform complex tasks. Generally speaking my projects fall into two categories: programmable matter and global health. Programmable matter is the concept of creating a substance that can be reprogrammed and reconfigured to perform different tasks when the need arises. I developed an assembly technique that utilizes laser heating to create bubbles in a microfluidic environment, which are then used to connect microscale components. By granting the user control over placement of these "bubble latches," arbitrary structures can be formed and reconfigured *in situ*. My other projects have revolved around developing mobile microfluidic technologies, particularly for global health applications. This is driven by the fact that for all the significant advancements in lab-on-a-chip (LOC) technologies, consumer level uptake of such devices has been limited. This is primarily due to the need for a large number of external components (power source, computer, pump, etc.) to support the microfluidic chip, thus confining most technologies to lab settings. In my work I addressed some of the major overarching limitations of current LOC systems by exploiting the ubiquity of solar energy and

smartphone technology to enable new microfluidic-based diagnostics. For example, by using an external light source such as sunlight, I demonstrated the ability to control flow in a microfluidic device without the need for powered pumps or valves. I have also invented a smartphone-assisted solar thermal method to perform polymerase chain reaction, a biochemical technique for amplifying nucleic acids. These novel technologies provide a means to perform complex diagnostics while dramatically reducing the reliance on external power and infrastructure. Such innovations could in the coming years help transform the healthcare landscape, particularly in the developing world.

BIOGRAPHICAL SKETCH

Li Jiang received his Bachelors of Science degree in Applied Mathematics, Engineering and Physics from the University of Wisconsin – Madison in 2009. He first became interested in microfluidics in junior year of college when a guest speaker of a MEMS course presented on the subject. He was particularly fascinated by the incredible number of biological applications that microfluidics could to offer. Li was accepted into the Mechanical Engineering Department at Cornell University in 2009 and joined Professor David Erickson's lab shortly thereafter. In his first years, as Li developed the bubble-based assembly technique, he became known as the "bubble guy" to some of his dear friends, who were clearly jealous. Perhaps because of this, or perhaps because his true passion lied elsewhere, Li decided to explore biological applications of microfluidics instead. Li has worked extensively with the Cornell Nanofabrication Facility (CNF) and the Nanobiotechnology Center (NBTC) during his time at Cornell. With support from DARPA, the National Institute of Health (NIH) and the National Science Foundation (NSF), Li developed several unique optofluidic technologies with applications in microscale assembly and global health diagnostics. His goal is to continue advancing diagnostic technologies with applications in the developing world.

To the love of my life, Rebecca (wowowewowe)

ACKNOWLEDGEMENTS

My time at Cornell has provided some of my most rewarding experiences so far, and I could not have done any of it alone. First and foremost I must thank Professor Erickson for being not only a tremendous advisor but also a visionary who has helped guide me along all the right paths. I never imagined that I could have learned so much from him, and I continue to learn to this day. I have always wanted my research to be innovative, risky, and impactful, and the Erickson Lab is all that and much, much more.

Professor Cesarman has been an integral part of my success as well, thanks to her support and eagerness to answer all of my questions. In addition, without her involvement in the project, I may not have been able to travel to Africa to test my research, which is certainly one of the highlights of my PhD career. Although I missed the lions and zebras, I will always remember the three of us drinking tusker and trying to figure out just how many menus the hotel restaurant had, and of course trying to convince airport security that we're not carrying dangerous equipment (no batteries).

My colleagues in the Erickson Lab have been phenomenal in providing an environment in which I feel intellectually challenged and excited. In particular, I wish to thank (in order of seniority) Bernardo Cordovez, Mekala Krishnan, Michael Kalontarov, Michael Mak, Vlad Oncescu, Matthew Mancuso, Lars Nielsen, Seoho Lee, and the rest of Erickson Lab for having offered valuable feedback throughout my years in the lab. I want to thank certain guilty members of the group for the incredible, incessant mess of our lab (you know who you are). I also wish to

thank the guilty members for never telling me when we run low on supplies, but as soon as we run out they talk like they've been waiting for weeks (you know who you are).

The friends that I've made here could fill my whole thesis. Very briefly: Thanks to Vlad for helping me break out of my shell and always being up for a good time. Thanks to Big Ben, who's one of the most wholesome guys I know. Thanks to Beg for being Beg. Thanks to Juan and Mike for Rock Lobster. Thanks to Matt for being my Rebecca when my Rebecca was Karen's Matt. And of course to Karen, my sister and my best friend, for being there every step of the way.

I acknowledge the funding sources and facilities that have made my research possible, specifically the Defense Advanced Research Projects Agency, the National Science Foundation, the National Institute of Health, the Clinical and Translational Science Center, the Cornell Nanoscale Science and Technology Facility, and the Nanobiotechnology Center.

I sincerely thank my family for being supportive of all of my endeavors. My parents, in-laws, grandparents, aunts, uncles, and cousins have continued to cheered me on and never miss a chance to tell me how proud they are.

Finally, I would have died by now or at least be in critical health if I did not have my amazing wife to support me over the years. Rebecca has truly been my anchor in these turbulent waters called graduate research. It takes a strong woman to make the sacrifices she has made and on top of that to put up with me. Incredible things are in store for us and I can't imagine discovering them with anyone else. I love you babe!

TABLE OF CONTENTS

Biographical Sketch……iii

Dedication……iv

Acknowledgement……v

Table of Contents……vii

List of Figures……viii

List of Tables……x

Chapter 1. Introduction……1

Chapter 2. Directed self-assembly of microcomponents enabled by laser-activated bubble latching……7

Chapter 3. Light-Governed Capillary Flow in Microfluidic Systems ……30

Chapter 4. Solar thermal polymerase chain reaction for smartphone-assisted molecular diagnostics……56

Chapter 5. KS-Detect: Implementation of an integrated solar thermal PCR system in preliminary trials in Africa……87

Chapter 6. Conclusions……98

LIST OF FIGURES

Figure 2.1 Laser-activated bubble latching.....11
Figure 2.2 "Controlled disassembly" 14
Figure 2.3 Bubble growth analysis.....16
Figure 2.4 Characterizing bubble latching strength.....19
Figure 2.5 Rigid-to-flexible transition of assembled structures.....21
Figure 2.6 Tetromino reconfiguration of assembled structures.....22
Figure 2.S1 Bubble growth data for confined and unconfined bubbles.....26
Figure 2.S2 Tiles used for reconfiguration demonstrations and force measurements.....26
Figure 2.S3 Gas generation in PDMS due to laser heating.....27
Figure 3.1 Light-governed flow actuation and manipulation.....36
Figure 3.2 PNIPAAm grafted onto PDMS surfaces.....39
Figure 3.3 Flow rate characterization at various temperatures.....41
Figure 3.4 Thermal characterization using Rhodamine B.....43
Figure 3.5 Flow actuation and valving demonstration.....45
Figure 3.6 Lamp-guided flow.....46
Figure 3.S1 Dynamic contact angle change over time.....52
Figure 3.S2 Grafting effectiveness at different UV exposures.....52
Figure 4.1 Solar thermal PCR system.....62
Figure 4.2 Thermal characterization and demonstration of solar thermal PCR.....65
Figure 4.3 Characterization of simulated cloud coverage.....66
Figure 4.4 Fluorescence detection of human biopsy samples.....68
Figure 4.S1 Disassembled view of electronic components.....82
Figure 4.S2 Measurements of fluorescence intensities.....82
Figure 4.S3 Comsol simulation of solar thermal PCR chip.....83
Figure 4.S4 Analysis of band intensity versus time of day.....83
Figure 4.S5 Availability of sunlight compared to PCR requirements.....84
Figure 4.S6 Solar simulator system.....84

Figure 5.1 Advantages of smartphone based lab-on-a-chip technology. ……..91
Figure 5.2 KS-Detect prototype.……..93
Figure 5.3 Preliminary testing in Africa.……..94
Figure 5.4 Gel images of samples tested in Africa. ……96

LIST OF TABLES

Table 3.S1 Comparison of light-guided flow technique to others……..53

Table 4.S1 Projected battery life of PCR devices using smartphone/tablet battery……..81

Table 4.S2 Probe and target sequences for KSHV……..81

Table 5.1 Sample results obtained in Africa……..95

CHAPTER 1

INTRODUCTION

1.1 Programmable and Reconfigurable Microscale Assembly

Fantastical but also ideal visions for programmable matter can be found in a number of science fiction movies, comic books and other outlets for imagination. The core concept is a material that can morph into any desired shape to perform any required task, all at the snap of one's fingers. As researchers explore potential avenues for making such materials into reality, there is significant interest in pushing programmable matter to small scales, with the vision that a large number of micro- or nanoscale elements can collectively form arbitrary structures at high resolution. Unfortunately, a number of complications arise as the assembly components reduce in size, and traditional pick-and-place assembly techniques become extremely difficult to implement. Currently, the majority of micro- and nanoscale assembly techniques rely on self-assembly, which exploit nature's tendency to reach a low energy state as the driving force behind creating desired structures. Such techniques however are relatively deterministic in the final forms that structures take and do not exhibit the characteristics of programmable matter.

Through the use of fluidic forces in microfluidic environments, another category of assembly techniques has recently emerged, including for example railed microfluidics[1] and directed fluidic assembly[2]. Such techniques utilize fluidic forces for guidance and solid mechanical forces for latching, thereby allowing the creation of a wide range of arbitrary structures. Unfortunately, after a structure has been made, reconfiguration becomes very difficult if not

impossible due to the quasi-permanent nature of the latches, which restricts the ability to reposition or disassemble the components post-assembly.

In Chapter 2, I describe my approach to addressing this issue by giving the user control over placement of the latches. This is done through "laser activated bubble latching," which combines the advantages of self-assembly through the use of a bubble's surface tension forces and directed fluidic assembly by performing the assembly in a microfluidic environment. Through this process, components can be directed to connect at arbitrary location by simply using a laser to heat the desired locations. In addition, I exploit the compressibility and flexibility of gas bubbles to demonstrate a range of reconfiguration capabilities, including rigid-to-flexible quasi-phase transition and structural transformation of assembled systems.

1.2 Light-controlled flow in microfluidic systems

In working on the laser-activated bubble latching project, I gained an appreciation for developing techniques that support an array of functions, but do not necessarily require complex fabrication and infrastructure. Moving forward I wanted to create microfluidic technologies that retain these characteristics and are usable outside of the lab setting. In particular, I wished to create a platform that would have general utility for microfluidics in the field. With this in mind, I decided to investigate the ability to control flow without needing to fabricate pumps, valves, electrical components, or power. This was interesting because although controlling microfluidic flow is a heavily studied area with an immense number of developed techniques, very few of them are practical outside of laboratory settings. Ones that

are feasible for point-of-care settings, such as lateral flow techniques, are often limited to a 1-step process, preventing analysis of more complex samples.

In order to achieve a simple and power-free system for microfluidic flow manipulation, I developed a technique that uses photothermal energy to guide flow. Details of this work are discussed in Chapter 3. This is done by grafting the microfluidic channel surface with a thermo-sensitive polymer called poly(N-isopropylacrylamide) (PNIPAAm)[3], which changes its surface properties based on the environmental temperature. In this case, the surface becomes increasingly hydrophobic as the temperature rises above 32°C. By shining a light on the microfluidic device and using a black film to convert that light into heat at specific locations, channels are made hydrophobic to valve off flow, while neighboring hydrophilic channels passive draw flow through. Using this system, I characterized the flow rate as a function of temperature, which showed that in addition to on/off valving, this technique can also be used to control the flow rate. After having characterized the system, I achieved flow guiding again by removing the majority of the infrastructure to leave only the chip and a lamp. This demonstrates the ability for such a device to be used in the field with sunlight as the heat source.

1.3 Solar-powered mobile microfluidic for global health

After gaining a fair amount of expertise on photo-thermal microfluidic systems over my past projects, it became clear to me that this type of technology has significant potential in point-of-care diagnostic applications due to the possibility of using sunlight as the energy source when

there may not be alternatives. In terms of diagnostics, polymerase chain reaction (PCR) emerged as perhaps the most potentially impactful application of solar thermal microfluidics. PCR is a heavily used biochemical technique for amplifying trace amounts of nucleic acids in a sample, but remains mostly unavailable in the developing world due to its high infrastructure and power requirements. Ultimately, however, PCR requires heating of the sample. Therefore, a simple system that can perform PCR using solar heating could have major implications for developing world diagnostics.

In Chapter 4, I describe my work in developing the solar thermal PCR system. This is achieved through a relatively simple platform, in which a lens concentrates sunlight onto a microfluidic chip, and the light is subsequently converted into heat to drive the PCR reaction. Traditionally, PCR requires cycling a sample through up to 3 temperatures in order to denature and duplicate the target DNA. In our device, sunlight is masked to produce the same temperatures at different locations along the radius of the chip. A microfluidic channel is then designed to repeatedly pass through these regions. Therefore, as a sample moves through the channel, it experiences the same temperature cycling as it would in a PCR machine. The temperatures in each zone are measured by thermocouples and read by the user *via* a smartphone app. Several parameters were characterized for this system, including detection limits in terms of initial concentration and cycling speed. I also demonstrated that tests can be successfully performed for most of daylight hours (12 hours per day in July in Ithaca, NY). Additionally, the effect of clouding was analyzed to show that minimal amounts of cloud cover would not dramatically affect PCR efficiency, however efficiency drops quickly as the duration of clouding increases.

Finally, I used the solar thermal PCR system to analyze human tissue biopsies infected with Kaposi's sarcoma herpesvirus (KSHV) and mycosis fungoides and demonstrated the ability to discern between Kaposi's sarcoma-positive samples and KS-negative ones using fluorescence-based detection. By eliminating the heating energy required for PCR, we reduce the total power needed in the system by 2 orders of magnitude as compared to commercial PCR machines.

Through further advancement of the solar PCR technology, I developed a portable prototype called the KS-Detect, which is discussed in Chapter 5. This system was taken to Kenya and Uganda in February 2014 to begin preliminary testing of human biopsies. The process includes performing HotSHOT sample lysing for DNA extraction from tissue, solar thermal PCR using lyophilized reagents for DNA amplification, and smartphone-aided fluorescence detection. In the updated prototype, smartphones are more heavily integrated into the system to include thermal sensing, micro-pump control, and fluorescence analysis. Based on our experiences on site and feedback from local clinicians and doctors, I am making improvements within the system towards building a 2nd generation prototype. My hope is that this technology will help create a product that can soon be deployed to limited infrastructure settings and make PCR a widely available method for developing world diagnosis.

REFERENCES

1 Chung, S. E., Park, W., Shin, S., Lee, S. A. & Kwon, S. Guided and fluidic self-assembly of microstructures using railed microfluidic channels. *Nature Materials* **7**, 581-587 (2008).

2 Tolley, M. T., Krishnan, M., Erickson, D. & Lipson, H. Dynamically programmable fluidic assembly. *Applied Physics Letters* **93** (2008).

3 Sun, T. & Qing, G. Biomimetic Smart Interface Materials for Biological Applications. *Advanced Materials* **23**, H57-H77 (2011).

CHAPTER 2

DIRECTED SELF-ASSEMBLY OF MICROCOMPONENTS ENABLED BY LASER-ACTIVATED BUBBLE LATCHING[1]

2.1 Abstract

This paper introduces a method for microscale assembly using laser-activated bubble latching. The technique combines the advantages of directed fluidic assembly and surface tension-driven latching to create arbitrarily complex and irregular structures with unique properties. The bubble latches, generated through the laser degradation of the tile material, are created on the fly, reversibly linking components at user-determined locations. Different phases of latching bubble growth are analyzed and shear force calculations show that each bubble is able to support a tensile force of approximately 0.33μN. We demonstrate that by exploiting the compressibility of bubbles, assembled objects can be made to switch between rigid and flexible states, facilitating component assembly and transport. Further, we show reconfiguration capabilities through the use of bubble hinging. This novel hybrid approach to the assembly of microscale components offers significant user control while retaining a simplistic design environment.

2.2 Introduction

Directed assembly methods, such as robotic pick-and-place, have been the essential manufacturing process for constructing complicated multi-component systems at large scales.

[1] Reprinted with permission from Li Jiang and David Erickson, "Directed Self-Assembly of Microcomponents Enabled by Laser-Activated Bubble Latching," *Langmuir* 27 (17), 11259-11264. Copyright (2011) American Chemical Society.

These are methods that require some form of energy input into the system, such as robotic or manual assembly of buildings and cars. Once the sizes of the components reach down to the sub-millimeter scale, these serial assembly methods begin to become prohibitively slow and expensive due to the need for high positioning accuracy and the presence of obstructive adhesion forces[1]. Self-assembly techniques that are driven by a system's tendency to reach an equilibrium state, termed static self-assembly[2], represent an alternative that overcomes the limitations of serial assembly at the micro- and nanoscales[1-4].

Surface tension forces are frequently used as a latching method for self-assembly at the microscale[4-6]. In such systems, a liquid-gas interface will tend to a low energy configuration by minimizing its surface area. In early works, components were placed in a large water reservoir and assembled based on the geometric properties or wettability characteristics of their faces[7-9]. Subsequently, droplet latching techniques were developed as a more targeted assembly approach. Small liquid droplets of solders[6,10-17], resin[18] and water[19-21] were used to make site-specific connections between components. These two-phase methods have achieved highly accurate alignment[19], alignment in specific orientations[11,15], 3D structures[10-12], and formation of electrical networks[10,12,14,16]. Using large substrates as receptor platforms, assembly through surface tension techniques can be massively parallel[13,14,17], and therefore potentially faster and cheaper than directed assembly approaches. Thus far, surface tension has primarily been employed to achieve self-assembly, which carries several drawbacks. Assembly is achieved probabilistically, and therefore assembly yield is not yet as high as that of deterministic approaches. Additionally, in most cases the final structure's shape and size is critically

constrained by the initial design and the number of sub-elements used in the experiment, making arbitrary structures difficult to generate.

Recent directed fluidic assembly techniques such as railed microfluidics[22,23] and dynamically programmable fluidic assembly[24-26], in which the fluidics is the main force for manipulating components, exploit microscale fluidics to circumvent adhesion problems of other microscale directed assembly methods and provide the user with more control than self-assembly techniques in the generation of structures. Unfortunately, the latches used in these works, along with the surface tension-based methods mentioned previously, all share characteristics that restrict the level of control given to the user. For example, the latches must be predefined during the fabrication process and are permanently on during use. This restricts the assembly of individual pieces to linking at specific locations. In addition, the quasi-permanent nature of the latches restricts the ability to reconfigure structures once they are assembled. Some work has been done to add switching capability to soldering sites using microheaters[13]. In that work, the switching mechanism was integrated on a large substrate, and there was no switching capability on a component-to-component level.

In this paper, we introduce laser-activated bubble latching, a new directed self-assembly method that combines surface tension-driven self-assembly with directed fluidic assembly and provides a much higher level of control than other latching methods. As illustrated in Fig. 2.1, bubble latches are created at generation hubs on SU-8 microtiles by the user through directed laser heating post-fabrication (See Movie 2.S1). The tile must be fabricated using a

hydrophobic material to facilitate latching between it and the bubble. This process allows the components and the hubs to be designed in a general scheme while giving the user control over the placement of the actual latches, allowing the user to treat each hub as a "switch" that activates latching at arbitrary times and locations. The fluidic properties of bubble latching also facilitate greater structural flexibility of an assembled structure. We demonstrate a "controlled disassembly" approach to create arbitrary structures that are not constrained by the initial component design. We explore the growth process of the bubbles and the maximum latching force of these bubble latches as a means of understanding this system. The maximum latching force was found to be in a range that enables structural integrity while also facilitating reversibility. Finally, we exploit the compressibility of the bubbles to induce rigid-to-flexible transitions of assembled objects, allowing for large deformations without unlatching, and demonstrate that the basic components can be quickly and deterministically reconfigured by using the bubbles latches as hinges.

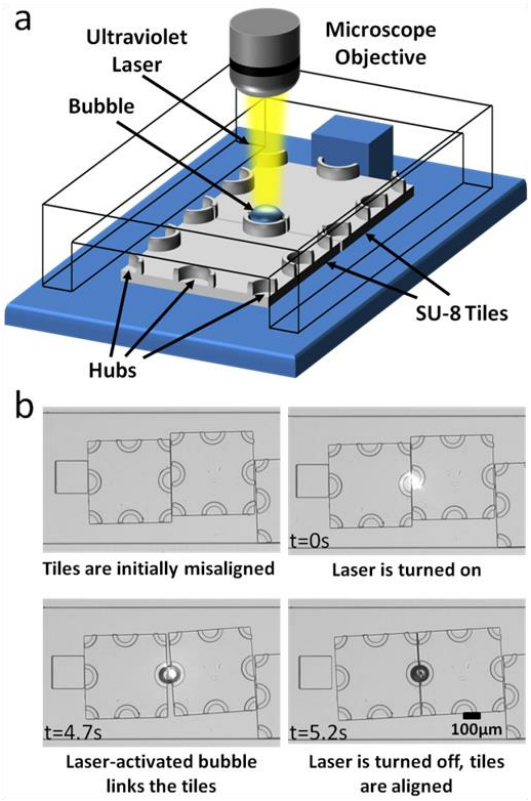

Figure 2.1. Laser-activated bubble latching and demonstration of self-alignment. (a) Schematic showing how laser light is used to create a bubble that links two components. In the actual experiments this would represent a view from the bottom. (b) Two SU-8 tiles are initially misaligned. After exposure to the laser light, a latching bubble is generated. The surface tension of the newly formed bubble aligns the components into a rigid unit. (See Movie 2.S1)

2.3 Materials and Methods

2.3.1 Fabrication

The 500×500 μm^2 SU-8 microtiles and the polydimethylsiloxane (PDMS) channels were fabricated with standard photolithography techniques[27]. Moulds were made by spinning SU-8 2050 photoresist (Microchem) on silicon wafers at 1900 rpm for 30 seconds to obtain a 90 μm thick film. The wafers were then soft baked at 65°C for 2 minutes and at 95°C for 10 minutes, patterned through a chrome photomask using the ABM Contact Aligner at the Cornell Nanoscale Science and Technology Facility and hard baked at 65°C for 2 minutes and at 95°C for

10 minutes. After cooling to room temperature, unexposed SU-8 was removed with SU-8 developer. A 10:1 ratio of PDMS (Sylgard 184) base and curing agent was poured over the SU-8 mould and cured at 80°C for two hours. A 1.9mm diameter punch was used to make a hole at the inlet of the microchannel structure to facilitate placement of tiles, while a 0.8mm diameter punch was used to create the holes at all other fluidic ports (Fig. 2.2a). The PDMS and glass slide were plasma treated for 30s and permanently bonded. Because the microtiles tended to get stuck on a hydrophobic PDMS surface, the channels were used immediately after bonding to maintain the hydrophilic property of the PDMS.

For the microtile fabrication, Omnicoat, an organic polymer solution, was spin-coated onto a silicon wafer at 3000 rpm for 30 seconds and baked at 200°C for 1 minute. SU-8 2025 was spin-coated on top of this at 2500 rpm for 30 seconds to achieve a film thickness of 30 μm. This was then exposed and developed using standard procedures as stated previously. To create the hubs to confine the bubbles, a second layer of SU-8 2025 was spin-coated onto the wafer at 2000 rpm to achieve an additional thickness of 30 μm and again exposed and developed. Finally, the wafer was placed in Microposit MF 321 for 24 hours to dissolve the Omnicoat layer. The released tiles were then stored on a sheet of Whatman filter paper until use.

2.3.2 Experimental Technique

An inverted microscope mounted with a CCD camera (pixeLINK) was used to record videos of the experiments at 14 frames per second. A 0.5 mm diameter metal rod bent into an L shape was used to pick up individual tiles. Its tip was wetted with DI water and put in contact with a

tile. The tile is picked up via surface tension and then inserted into the microfluidic chamber. Due to the different geometry between the top and bottom surfaces of the tiles, they must all be inserted with the same side facing up. This was done by inspecting the tile's reflection under white light, and choosing to only pick up tiles in the correct orientation. The microfluidic chips were placed upside down with the PDMS layer below the glass slide for the experiments due to sticking problems observed between the tiles and the PDMS (see Supplementary information). The bubbles were created through heating of the tiles by a UV laser (40mW, 405nm) directed at the hubs. Tygon tubing was used to connect the inlet and all outlets to syringes, while syringe pumps were used for flow injection.

2.4 Results and Discussion

2.4.1 Bubble Formation and Controlled Disassembly of Components

Bubble generation hubs in the form of 100 μm-inner diameter, 125 μm-outer diameter SU-8 rings act as walls to confine the bubbles. As the SU-8 absorbs the laser energy, its temperature rises and eventually reaches the degradation temperature at 380°C[28], where carbon dioxide, carbon monoxide and other gases are generated[29]. When confined in water, the gases produced from the etched SU-8 form a bubble. The bubble latches to the SU-8 due to its surface hydrophobicity[30,31]. As the laser continues to heat the tile, the water near the bubble may also evaporate if it reaches boiling temperature.

As Fig. 2.2 shows, we use the ability to arbitrarily place individual bubble latches in order to realize a "controlled disassembly" approach for creating complex structures with simple flow

controls. The tiles are first assembled in the chamber by injecting flow through the top and drawing it out through specific ports on the bottom and sides of the chamber. With some minor tapping to the microfluidic chip, the fluid flow pushed the tiles into packed arrays. Laser-activated bubbles are then created between specific tiles, both linking them and securing them in place due to the additional adhesion between the bubbles and the chamber floor. At this point, the flow directions of the ports are simply reversed, and unconnected tiles become released, leaving behind the assembled structure (see Movie 2.S2). We demonstrate the creation of "hanging" structures with a carved out interior (Fig. 2b), multiple structures created in parallel (Fig. 2.2c) and multi-step assembly to create voids, as shown by a stick figure (Fig. 2.2d). The ability to assign arbitrary latching locations uniquely enables the creation of these complex structures (i.e. with voids and carved out regions), in contrast to other directed fluidic assembly techniques, where structures must be built in a bottom-up fashion.

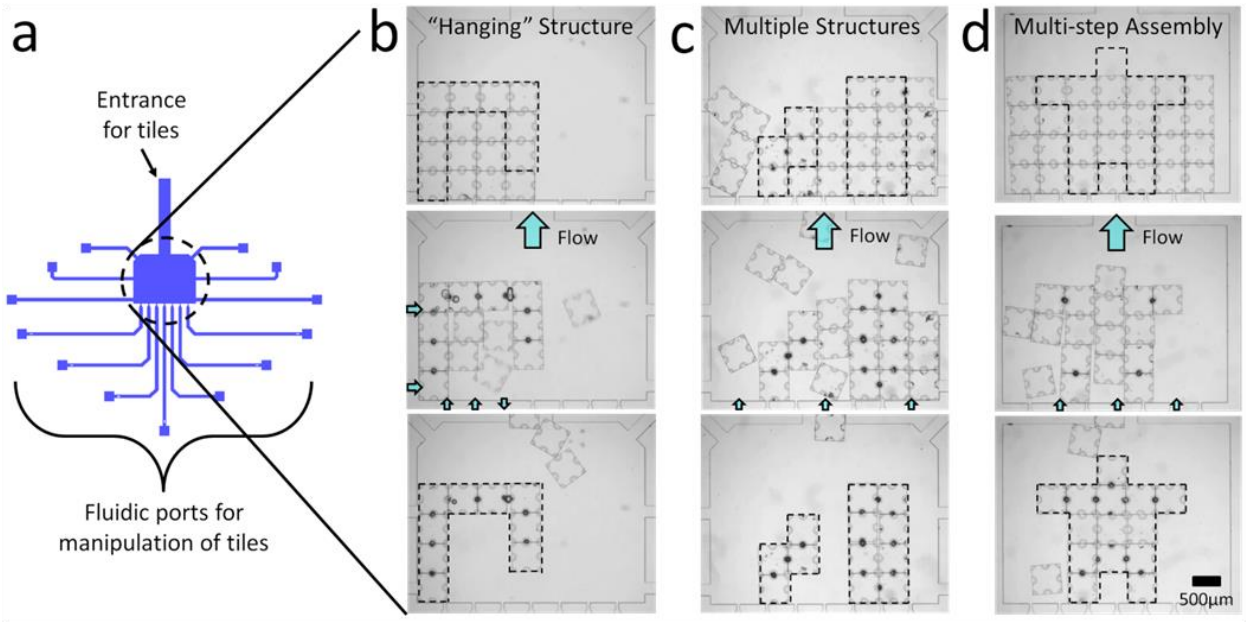

Figure 2.2. Complex structures created via "controlled disassembly" using bubble latching (a) Design of the microfluidic chamber used to create the structures. (b) The formation of a hanging structure demonstrates the ability to create carved out shapes. (c) Separate structures

are created in parallel in the same chamber. (d) A stick figure is created in multiple steps by first latching tiles to make the arms and legs, then internally reconfiguring the structure by pushing up the middle column to make the head and body, and finally latching the entire structure. The arrows in the center row of images represent the ports used and the direction of the flow through the ports during the "controlled disassembly" step. (See Movie 2.S2)

2.4.2 Characterization of bubble growth and latching strength

The growth behaviors of bubbles both confined within the hubs and unconfined are compared in Fig. 2.3. For each test, we found the frames at which the laser is turned on and also when the tile reaches the degradation temperature, accompanied by a sudden burst of light. In all cases, after being exposed to the laser, the SU-8 reaches its degradation temperature after about 3s. This creates a small deformed region on the tile that is visible if the laser is turned off. The images following this frame are analyzed in Matlab using custom code to mark and calculate the diameter of the bubble. The bubble diameters and the corresponding frame numbers are collected and plotted in Excel. We found that the growth of the bubble can be divided into two stages, as illustrated by Fig. 2.3. At first, the bubble expands steadily until it reaches about 50μm in diameter, at which point it comes in contact with the PDMS surface. This contact changes the interfacial energies, leading to a second stage where the bubble spreads out rapidly, representing a change in the bubble geometry from a spherical shape to cylindrical. When confined inside the hubs, the sudden expansion is stopped by the ring borders at around 100μm in diameter. When the bubble is generated in the center of the tile, and therefore unconfined, it continues to grow beyond 100μm. The bubble growth times, shown in Fig. 2.3b, are affected by minor changes in external conditions such as the angle of the laser light incident on the surface and slight movement of the tile when it is excited by the

laser, and therefore vary from 5s to 30s. Conversely, the sizes of the bubbles at the different transition points remained consistent throughout all experiments and are marked by dashed lines in Fig. 2.3b (see Section 2.7 and Fig. 2.S1).

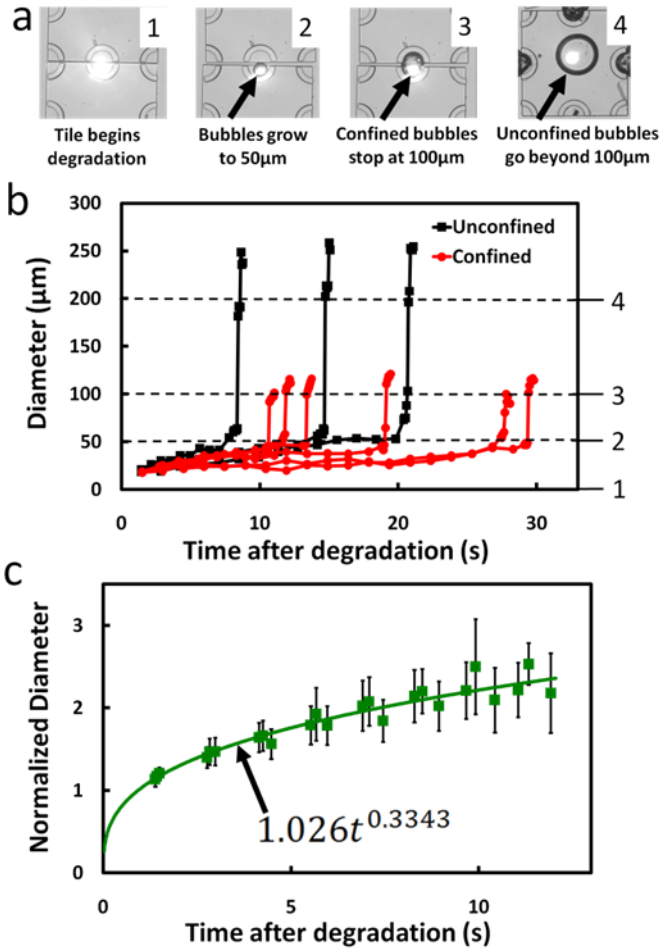

Figure 2.3. Analysis of bubble growth dynamics (a) The bubble growth process showing (1) the tile reaching the degradation temperature (time = 0), (2) the bubble growing to 50µm before the sudden expansion, (3) the expansion stopping at 100µm for confined bubbles, and (4) growing beyond 100µm for unconfined bubbles. The black arrows point to the bubbles. (b) Graph of bubble growth, showing 9 tests out of 34, representing the range of growth times. Numbers on the right represent the bubble sizes at various transition points during growth and correspond to the numbers in the images. (b) For each experiment, the data points before the sudden expansion are averaged and fitted to a power function. The average values are then normalized by their respective coefficient and plotted, showing a radial growth proportional to time to the 1/3 power. Error bars represent one standard deviation.

Despite some inconsistencies in the growth time, analysis of the bubble size as a function of time can still produce a reasonable characterization of the volumetric growth rate. In Fig. 2.3b, the diameter growth data before the sudden expansion was averaged and fitted to an equation of the form $D = \alpha t^{\beta}$, where D is the bubble diameter, t is the time and α and β are empirical values. The average diameters were then divided by their respective coefficient α to normalize the data. Finally, the first eight normalized data points from each set were fitted to weigh the sets equally and are plotted in Fig. 2.3b. Through this analysis, we find $\beta = 0.3343$, which suggests that the bubble diameter increases proportionally to approximately $t^{1/3}$, and that the volumetric growth is approximately linear with time. This finding matches recent measurements of laser-induced bubble growth on metal pads[32], though we note that in our system, bubbles are produced from material degradation instead of liquid vaporization.

Several unknowns including the pressure inside the bubble, the rate at which the tile material is degraded, the temperature profile, and the interfacial tensions of our water-gas-SU-8 system preclude us from calculating the bubble volume using solely its observed diameter. In spite of this, a close estimate can be produced by recognizing that because the hub layer of SU-8 is 30µm tall, the bubble should also be 30µm tall when it makes contact with the channel. This, coupled with the fact that each bubble grows to 50µm in diameter at the time of contact, suggest that the bubble is close to hemispherical in shape. Therefore, the volume can be approximated as $\pi D^3/12$. Measurements have shown that the contact angle of an air-water interface on SU-8 is close to 90°[30,31]. Even though the gases in the bubble do not have the same composition as air, this result shows that the surface energy of this system behaves similarly to

air-water systems. A current limitation of the work is that the tiles are damaged during the creation of bubbles, and therefore each tile has a limited cycle of uses. We believe this can be resolved by fabricating the tiles out of a material with a high enough melting/degradation temperature such that the bubbles are created through liquid vaporization before any material is damaged. This is done recently by Zhang et al[32], who showed that bubbles produced in this manner do not collapse after the laser is turned off, demonstrating the potential to create components that can be reused indefinitely.

Characterizing the range of forces that the bubbles can sustain is important for defining the conditions under which an assembled structure remains connected or will disassemble. To do this here, we designed new tiles to allow for approximations to the flow profile in the channel and the shear force experienced by the tile, while keeping the size and properties of the bubble consistent (See Section 2.7 and Figure 2.S2). In the experiment, we cause one tile to stick to the PDMS wall through laser heating (see Supporting information and Figure 2.S3). As shown in Fig. 2.4a, another tile is then latched to it and a constant flow rate is maintained for five minutes. If the tiles stay latched during this period, the flow rate is increased by 1μL per minute. This process repeats until the free tile breaks off, and the final flow rate is recorded, which is used to calculate F_{max}, the maximum force that a bubble can sustain before unlatching. We estimate the hydrodynamic shear force applied to the tile with a simplified model taken from work developed by Krishnan *et al.*[33]. At the highest flow rate (30μL/min), the Reynolds Number is of the order 1. This, along with the simple channel geometry, allows us to assume that the flow over the tile takes a Poiseuille flow profile (Fig. 2.4b) of the form

$$\mathbf{v} = 3\mathbf{Q}/(2A_{c,t})[1-(y/H)^2] \qquad (2.1)$$

where H is 15µm, half the distance between the tile surface and the channel ceiling, y is the vertical position variable defined in Fig. 2.4b, $A_{c,t}$ is 2.4×10^4 µm^2, the cross sectional area of the channel minus the cross sectional area of the tile, and $\boldsymbol{Q}$ is the flow rate. This can then be related to the viscous shear force $\boldsymbol{F_v}|_{y=H}$ on the tile using

$$\mathbf{F_v}|_{y=H} = \mu(d\mathbf{v}/dy)A_t \qquad (2.2)$$

where A_t is 0.25mm^2, the area of the face of the tile. Evaluating this equation, we find $\boldsymbol{F_v}|_{y=H} = 0.035\boldsymbol{Q}$, where $\boldsymbol{Q}$ is in µL/min and $\boldsymbol{F_v}$ is in µN.

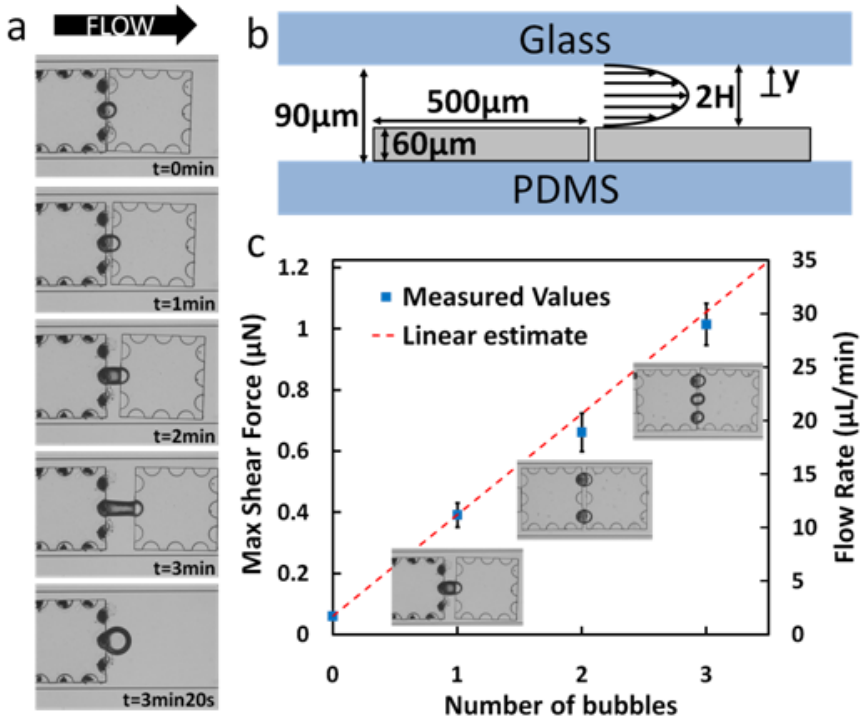

Figure 2.4. Breaking force measurements for bubble latches. (a) Sequence of images showing tiles linked by one bubble being pulled apart and ultimately unlatching. (b) Side view schematic of flow profile over tiles used to estimate shear force. (c) Plot of maximum flow rate and calculated force for tiles connected by 0, 1, 2, or 3 bubbles. Data matches well with the expectation that n bubbles can support n time as much force as one bubble latch. Error bars represent one standard deviation.

Experiments were performed with one, two, or three bubbles latching the tiles. With no latching, we find that a force of about 60nN is required to overcome the friction between the tile and the channel wall to move the tile. Subtracting off this static friction F_f, we find that one bubble is able to support a maximum force F_{max} of about 0.33μN. When multiple bubbles are used, they act in parallel, and therefore we anticipate latching with n bubbles to result in a maximum force equal to nF_{max}. The experimental relation between the maximum breaking force and the number of bubbles is plotted in Fig. 4*c* and shows good agreement with the linear estimate. This study shows that the user is able to adjust for the latching strength of the system through managing the number of bubbles generated. From these results, we nondimensionalize F_{max} using the equation $(nF_{max})/F_f$. Values above 1 indicate that the bubble system should be able to overcome the frictional force of the cargo. In this instance, we obtain a value of 5.5 for a single bubble latch, implying that it is enough to perform transportation and manipulation of the tile, which we subsequently demonstrate. In the majority of cases, we observe that when a bubble link breaks, the bubble does not split into two, but separates from one of the hubs cleanly. This suggests that the maximum force that a bubble can currently support is limited by the adhesion force between the bubble and the SU-8, and does not correspond to the surface tension force of the bubble itself.

2.4.3 Rigid-to-flexible transition and structural reconfiguration

Bubbles hold another important advantage over droplet latching mechanisms in that they are highly compressible and can easily expand or contract according to external stimuli such as heat or pressure. This allows for an object to be able to transition between states of rigidity and

flexibility without the need to disassemble. As Fig. 2.5 shows, when first assembled, a system is aligned and in its most compact form, but also stiff. When presented with a 90° bend in the channel geometry, it becomes stuck, prohibiting any further transport. By reducing the pressure inside the channel, the bubbles expand, causing the chain of tiles to loosen and allowing the structure to snake around the turn. After the tiles pass the corner, the pressure is increased, contracting the bubbles to their original size. The tiles realign, transforming back into its rigid and compact form before continuing down the channel (see Movie 2.S3).

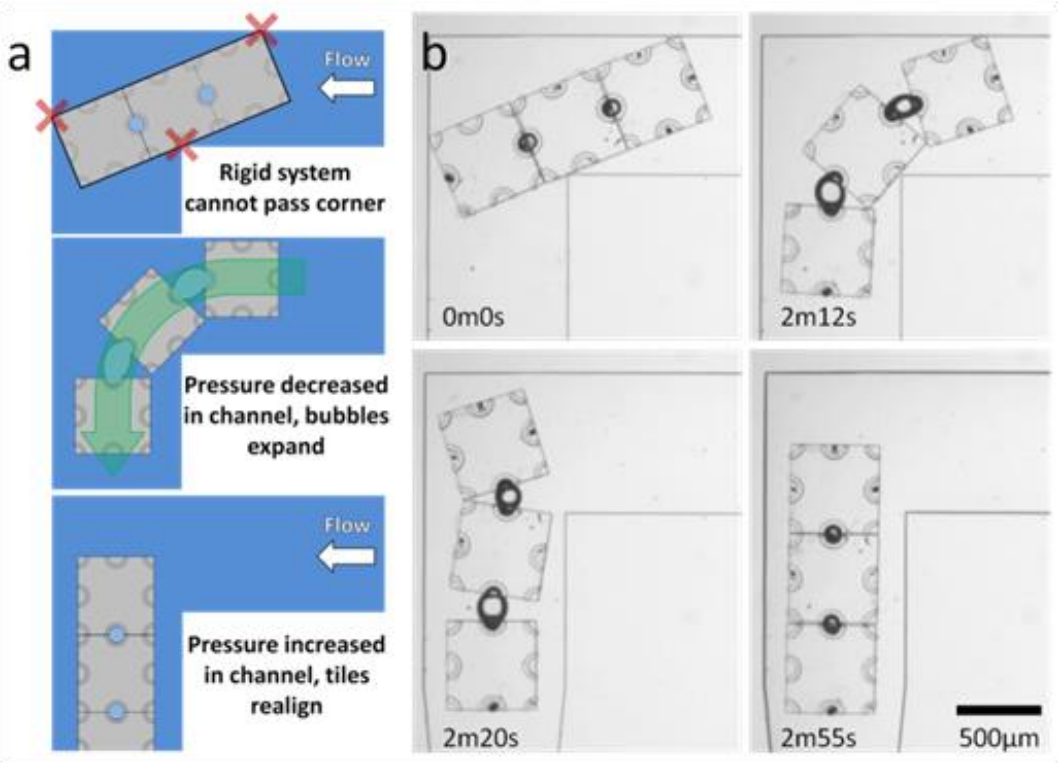

Figure 2.5. A rigid-to-flexible transition allows structure to pass through an obstruction. (a) Schematic diagram showing the rigid-to-flexible transition of an assembled object as it passes around a corner. (b) The tiles are stopped at the sharp 90° turn. By decreasing the pressure, the bubble latches expand to add flexibility, allowing the chain to bend around the turn. By raising the pressure, the bubbles contract to make the system rigid again. (See Movie 2.S3)

By creating a bubble hinge at the appropriate corners of adjacent tiles, we are able to deterministically reconfigure a structure without disassembly. We demonstrate this by reconfiguring a structure between the five tetromino shapes found in the original Tetris video game. By starting with four tiles in a row (the "I" shape), we map out a sequence with which to achieve each subsequent shape (Fig. 2.6a). In the experiments, each tile sits in front of a microfluidic port that the user can control to either inject or extract fluid and the laser is used to selectively create bubble hinges. In Fig. 2.6b-e and Movie 2.S4, each of the reconfiguration steps illustrated in Fig. 6*a* are demonstrated. In Movie 2.S4, the demonstrations are compared to reconfigure experiments done without creating a bubble hinge, which results in disassembly of the original structure.

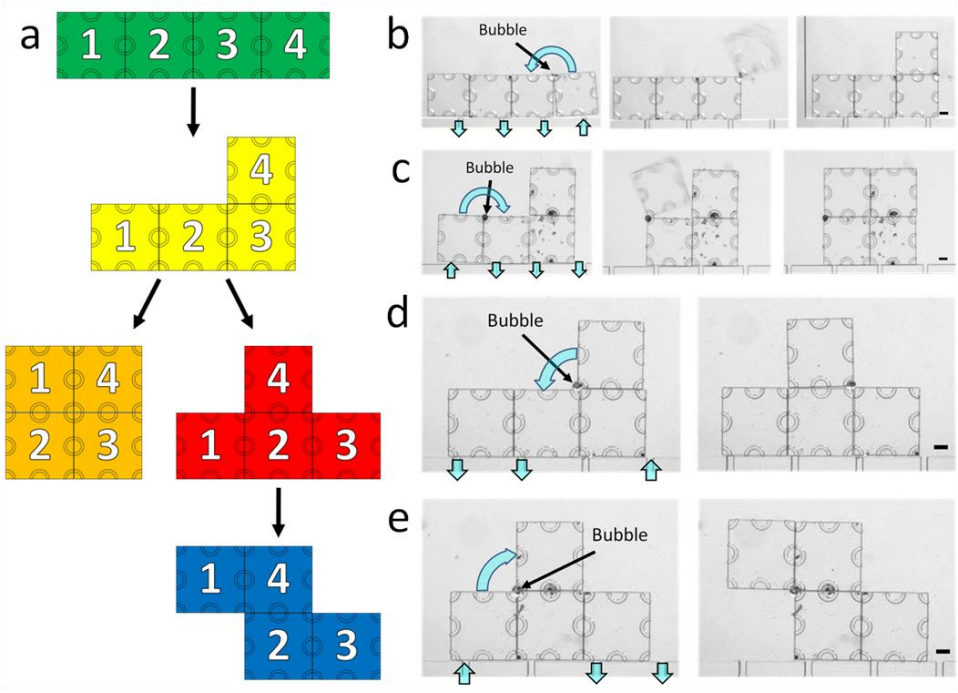

Figure 2.6. Tetromino reconfiguration demonstrations (a) Schematic of the sequence that one can take to reconfigure from the "I" shape to each subsequent form. Experimental demonstrations show (b) I-to-L, (c) L-to-O, (d) L-to-T and (e) T-to-Z reconfigurations. Arrows at the bottom of the images show the direction of flow through the ports. Scale bars 100µm. (See Movie 2.S4).

Performing various functions in a system requires the assembled structure to balance flexibility, where components are linked by a single bubble, with structural integrity, where they are linked by multiple bubbles. As demonstrated, both the bending and reconfiguration demonstrations are easily achieved when only one bubble is used to link the components. Therefore, relatively low fluid forces as identified by our force analysis are needed for transporting, bending, or reconfiguring structures as to avoid accidentally break a bubble link. At the same time, if disassembly of a structure is desired, higher forces can be applied to separate the tiles without damaging them, unlike systems with mechanical latches, where structural damage may be a problem. In the technique's current state, the ability to create the bubbles on command still allows for any bending, reconfiguration, or reassembly steps to be taken first, and then the system can be made more robust by adding more bubbles. In this sense, a structure can still be both flexible and structurally robust at different points in time.

2.5 Conclusions

In this article, we have characterized and demonstrated laser-activated bubble latching as a novel technique for assembling, transporting, and reconfiguring microstructures. This method brings together the advantages of both surface tension-driven self-assembly and microfluidically-directed assembly and presents several new functionalities. The control over latching locations affords a large degree of freedom in the assembly of components into arbitrary and complex structures. Utilizing the compressibility of bubbles allows for rigid/flexible transition of objects, which is particularly useful for structures that need to navigate through complex channel geometries. Bubble hinging at tile corners provides a quick

and accurate way to reconfigure structures post-assembly. Laser-activated bubble latching supports a simple design, provides significant assembly control to the user, and demonstrates novel capabilities not seen in other techniques.

2.6 Acknowledgements

The authors acknowledge funding from the Defense Advanced Research Projects Agency (DARPA). The authors also appreciate access to the Cornell Nanoscale Science and Technology Facility (CNF). We thank Mekala Krishnan, Michael Kalontarov, Michael Tolley, and Lars Nielsen for helpful discussions.

2.7 Supporting Information

2.7.1 Bubble growth data

All bubble growth measurements are shown in Fig. 2.S1a. Red data points represent bubbles that were confined within the hubs and blue data points represent bubbles that were not confined. Fig. 2.S1b shows the average bubble sizes taken from frames immediately before and immediately after the sudden expansion. We see that in both the confined and unconfined cases, the bubble first grows steadily to 50µm before the expansion. After the expansion, while the confined bubbles average at 100µm, the unconfined bubbles grow to about 150µm.

2.7.2 Design of different tiles

For the force experiments a different tile design is used for two purposes, as shown in Fig. 2.S2. One, the second layer of the tile fills the entire square, as opposed to being only the rings that

make up the hub as in the first design. This way, we can assume there is negligible flow under the tile as compared to above it, and therefore a Poiseuille flow profile can be adopted between the top of the tile and the channel. Second, each side of the tile houses three hubs, also 50μm in radius, so that force calculations can be easily done with multiple bubble latches. Dimensions of the tiles and the thickness of the layers were kept consistent between the two designs. Taking the density of SU-8 2025 as 1.22g/cm^3 and the dimensions of the tile to be 500μm × 500μm × 30μm, we find the gravitational force to be 18.3μN and the buoyancy force to be 15μN, resulting in a net downward force of 3.3μN.

2.7.3 Problems with sticking between SU-8 and PDMS

During initial experiments, we observed that through generating a bubble on the SU-8, the heated tile often came into contact with the PDMS wall. The PDMS was subsequently heated, as shown by bubbles created inside the wall (Fig. 2.S3). The heating of the two materials while in contact caused the SU-8 tile to become stuck to the PDMS such that the tile would not move even at high flow rates. For the bending and reconfiguration experiments, this issue was avoided by flipping the microfluidic device upside down after the tiles are inserted so that the heated region of the tile never comes in contact with the PDMS. For force measurement experiments, the chips were also flipped upside down to maintain the same procedure throughout. However, now we are able to selectively secure one tile to the channel wall while allowing another to be dragged by the flow, giving sensible values for the flow rates at which the bubble links break.

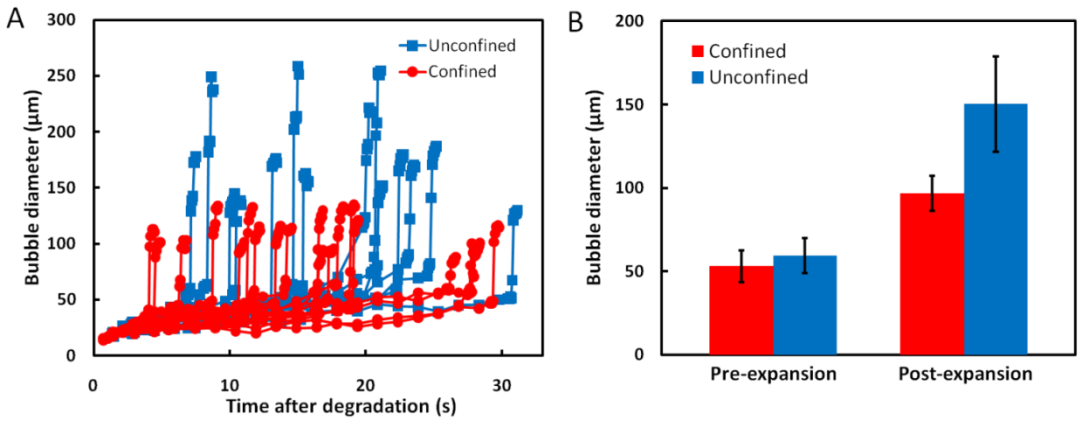

Figure 2.S1. Growth data of confined and unconfined bubbles. (a) Plot of 34 total measurements of the bubble size. (b) The average diameter of the bubble immediately before and after the expansion for both confined and unconfined cases. Before the expansion, both cases reach about 50µm, while after the expansion, the unconfined bubbles grow much larger than confined ones. Error bars represent one standard deviation.

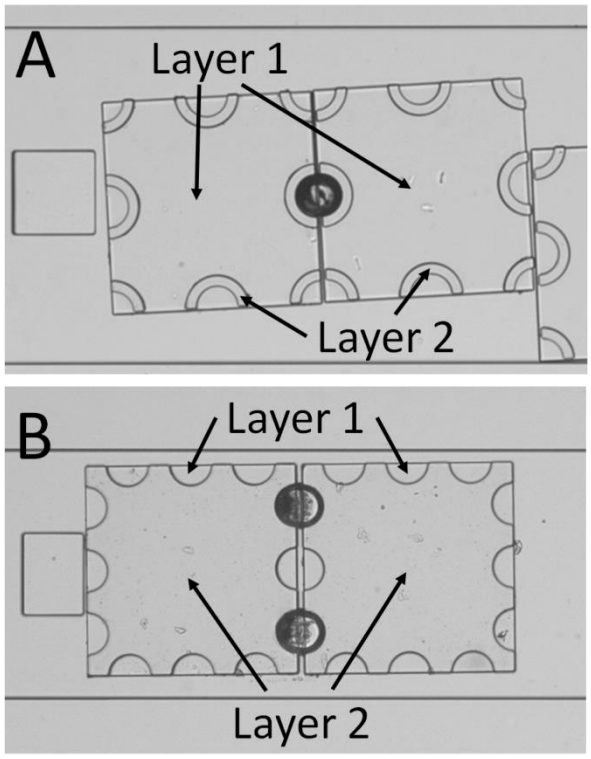

Figure 2.S2. Tiles used for demonstrations and force measurements. (a) Tiles used for bubble growth experiments and all demonstrations. The second layer of SU-8 makes up only the rings. (b) Tiles used for force measurements. The second layer fills the entire square except for the hub locations.

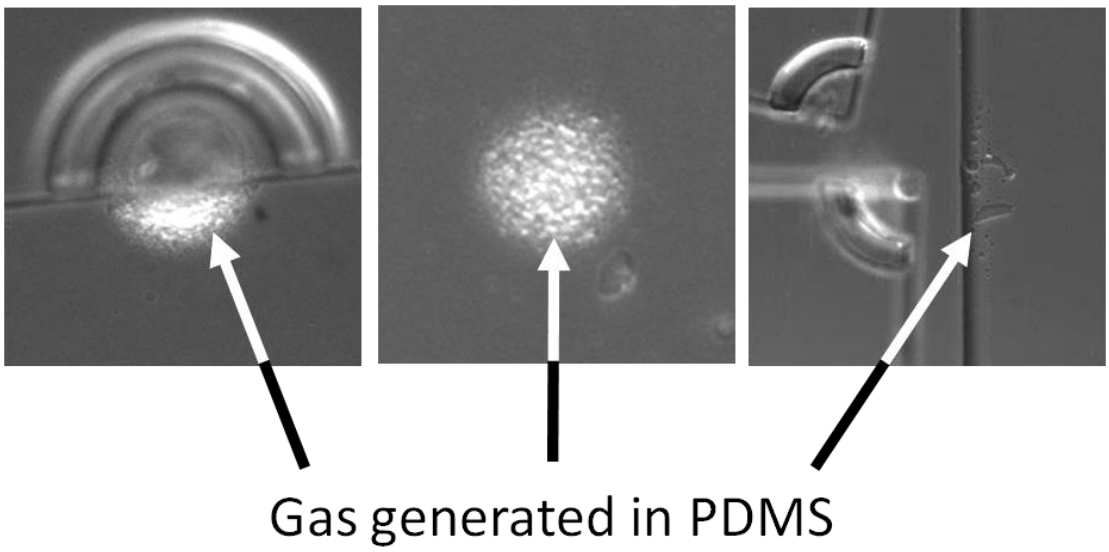

Figure S3. Heat from SU-8 creates what appears to be bubbles in PDMS. If the laser is kept on for long enough, the tile becomes stuck on the PDMS wall.

2.8 Supplementary videos

Movie 2.S1. Connecting components through laser-activated bubble latching. Two initially misaligned tiles are linked and aligned by a bubble created through laser heating. Tile docking is also shown, in which the bubble is produced on only one tile. A second tile is then brought into contact with the bubble. The two tiles are linked and transported together.

Movie 2.S2. Complex structures created via "controlled disassembly" using bubble latching. We create a hanging structure, where the inner tiles are removed after producing bubbles to latch the outer tiles. Next, we show the assembly of multiple structures in parallel. Lastly, we demonstrate multi-step assembly to create voids in structures.

Movie 2.S3. Rigid/flexible transition of an assembled structure. First, four tiles are loosely connected and misaligned. By decreasing the pressure in the chamber, the bubbles are compressed, realigning the structure. Second, rigidly connected tiles are unable to pass a corner. Decreasing the pressure in the channel expands the bubbles, which transitions the structure to become flexible, allowing it to bend around the corner. Afterwards, pressure is increased to realign the tiles.

Movie 2.S4. Bubble hinge reconfiguration demonstrations. Beginning with the "I" shape, we demonstrate reconfiguration into subsequent "L," "O," "T," and "Z," shapes. We also show a failed "L" to "T" reconfiguration attempt when a bubble hinge is not used. Finally, we show the motion of a latched "O" structure compared to an "O" shape that is not latched, in which case the tiles spread away from each other.

REFERENCES

1 Morris, C. J., Stauth, S. A. & Parviz, B. A. Self-assembly for microscale and nanoscale packaging: Steps toward self-packaging. *IEEE Trans. Adv. Packag.* **28**, 600-611 (2005).

2 Whitesides, G. M. & Grzybowski, B. Self-assembly at all scales. *Science* **295**, 2418-2421 (2002).

3 Ariga, K. *et al.* Challenges and breakthroughs in recent research on self-assembly. *Sci. Technol. Adv. Mater.* **9** (2008).

4 Mastrangeli, M. *et al.* Self-assembly from milli-to nanoscales: methods and applications. *J. Micromech. Microeng.* **19** (2009).

5 Syms, R. R. A., Yeatman, E. M., Bright, V. M. & Whitesides, G. M. Surface tension-powered self-assembly of micro structures - The state-of-the-art. *J. Microelectromech. S.* **12**, 387-417 (2003).

6 Harsh, K. F., Bright, V. M. & Lee, Y. C. Solder self-assembly for three-dimensional microelectromechanical systems. *Sensor. Actuat. a-Phys.* **77**, 237-244 (1999).

7 Hosokawa, K., Shimoyama, I. & Miura, H. Two-dimensional micro-self-assembly using the surface tension of water. *Sensor. Actuat. a-Phys.* **57**, 117-125 (1996).

8 Bowden, N., Terfort, A., Carbeck, J. & Whitesides, G. M. Self-assembly of mesoscale objects into ordered two-dimensional arrays. *Science* **276**, 233-235 (1997).

9 Terfort, A., Bowden, N. & Whitesides, G. M. Three-dimensional self-assembly of millimetre-scale components. *Nature* **386**, 162-164 (1997).

10 Gracias, D. H., Tien, J., Breen, T. L., Hsu, C. & Whitesides, G. M. Forming electrical networks in three dimensions by self-assembly. *Science* **289**, 1170-1172 (2000).

11 Linderman, R. J., Kladitis, P. E. & Bright, V. M. Development of the micro rotary fan. *Sensor. Actuat. a-Phys.* **95**, 135-142 (2002).

12 Cannon, A. H., Hua, Y. M., Henderson, C. L. & King, W. P. Self-assembly for three-dimensional integration of functional electrical components. *J. Micromech. Microeng.* **15**, 2172-2178 (2005).

13 Chung, J. H., Zheng, W., Hatch, T. J. & Jacobs, H. O. Programmable reconfigurable self-assembly: Parallel heterogeneous integration of chip-scale components on planar and nonplanar surfaces. *J. Microelectromech. S.* **15**, 457-464 (2006).

14 Morris, C. J. & Parviz, B. A. Micro-scale metal contacts for capillary force-driven self-assembly. *J. Micromech. Microeng.* **18** (2008).

15 Lin, C., Tseng, F. G. & Chieng, C. C. Orientation-specific fluidic self-assembly process based on a capillary effect. *J. Micromech. Microeng.* **19** (2009).

16 Reynolds, K., O'Riordan, A. & Redmond, G. Self-assembly of a functional electronic circuit directed by capillary interactions. *Appl. Phys. a-Mater.* **98**, 203-209 (2009).

17 Knuesel, R. J. & Jacobs, H. O. Self-assembly of microscopic chiplets at a liquid-liquid-solid interface forming a flexible segmented monocrystalline solar cell. *Proc. Natl. Acad. Sci. U. S. A.* **107**, 993-998 (2010).

18 Kim, J. M., Yasuda, K. & Fujimoto, K. Resin self-alignment processes for self-assembly systems. *J. Electron. Packaging* **127**, 18-24 (2005).

19 Martin, B. R., Furnange, D. C., Jackson, T. N., Mallouk, T. E. & Mayer, T. S. Self-alignment of patterned wafers using capillary forces at a water-air interface. *Adv. Funct. Mater.* **11**, 381-386 (2001).
20 Srinivasan, U., Liepmann, D. & Howe, R. T. Microstructure to substrate self-assembly using capillary forces. *J. Microelectromech. S.* **10**, 17-24 (2001).
21 Tsai, C. G., Hsieh, C. M. & Yeh, J. A. Self-alignment of microchips using surface tension and solid edge. *Sensor. Actuat. a-Phys.* **139**, 343-349 (2007).
22 Chung, S. E., Park, W., Shin, S., Lee, S. A. & Kwon, S. Guided and fluidic self-assembly of microstructures using railed microfluidic channels. *Nat. Mater.* **7**, 581-587 (2008).
23 Park, W., Lee, H., Park, H. & Kwon, S. Sorting directionally oriented microstructures using railed microfluidics. *Lab Chip* **9**, 2169-2175 (2009).
24 Tolley, M. T., Krishnan, M., Erickson, D. & Lipson, H. Dynamically programmable fluidic assembly. *Appl. Phys. Lett.* **93** (2008).
25 Krishnan, M., Tolley, M. T., Lipson, H. & Erickson, D. Hydrodynamically Tunable Affinities for Fluidic Assembly. *Langmuir* **25**, 3769-3774 (2009).
26 Kalontarov, M., Tolley, M. T., Lipson, H. & Erickson, D. Hydrodynamically driven docking of blocks for 3D fluidic assembly. *Microfluid. Nanofluid.* **9**, 551-558 (2010).
27 McDonald, J. C. *et al.* Fabrication of microfluidic systems in poly(dimethylsiloxane). *Electrophoresis* **21**, 27-40 (2000).
28 Feng, R. & Farris, R. J. Influence of processing conditions on the thermal and mechanical properties of SU8 negative photoresist coatings. *J. Micromech. Microeng.* **13**, 80-88 (2003).
29 MicroChem. (2009).
30 Xu, B. J., Lee, Y. K., Jin, Q. H., Zhao, J. L. & Ho, C. M. Multilayer SU-8 based microdispenser for microarray assay. *Sensor. Actuat. a-Phys.* **132**, 714-725 (2006).
31 Walther, F. *et al.* Stability of the hydrophilic behavior of oxygen plasma activated SU-8. *J. Micromech. Microeng.* **17**, 524-531 (2007).
32 Zhang, K. *et al.* Laser-induced thermal bubbles for microfluidic applications. *Lab Chip* **11**, 1389-1395 (2011).
33 Krishnan, M., Tolley, M. T., Lipson, H. & Erickson, D. Increased robustness for fluidic self-assembly. *Phys. Fluids* **20**, 073304-073301 - 073304-073316 (2008).

CHAPTER 3

LIGHT-GOVERNED CAPILLARY FLOW IN MICROFLUIDIC SYSTEMS[2]

3.1 Abstract

One of the current constraints of point-of-care diagnostics for low-resource settings is the difficulty in creating tools that are both simple to fabricate and use and also able to perform complex tasks. On one end, inexpensive and easy to use devices such as paper-based microfluidics have limited capability in processing relatively complex samples. Conversely, sophisticated microfluidic systems that can perform multistep processing require power and complex infrastructure. Light-based flow systems are of interest because, in principle, sunlight could be used to operate these tools, potentially allowing for increased functionality with minimal device complexity and expense. Here, we introduce a simple light-driven method to actuate and valve capillary based flow using poly(N-isopropylacrylamide) (PNIPAAm), a "smart" polymer that changes wettability as a function of temperature. It is grafted onto a carbon black-polydimethylsiloxane (PDMS) surface, which converts incident light into spatially modulated on-chip thermal patterns. We use this to create switchable hydrophobic and hydrophilic regions inside a microfluidic system that respectively stop and activate the flow, allowing for different chambers in the device to be filled at user-defined locations and times. We demonstrate thermally-tunable flow rates ranging from 4 μL min^{-1} at 25°C to 0.1 μL min^{-1} at 40°C. We also characterize the flow switching dynamics and show a response time of less than

[2] Reprinted with permission from Li Jiang and David Erickson, "Light-Governed Capillary Flow in Microfluidic Systems," Small 9: 107–114. Copyright (2012) Wiley-VCH

4 s following illumination. Light-operated capillary flow could provide both the simple design architecture and advanced functionality needed in low-resource point-of-care devices.

3.2 Introduction

For point-of-care diagnostics to become widely adopted in the developing world, devices must be low-cost and easy to use, yet multifunctional and capable of processing complex samples.[1-4] These goals are frequently in conflict with each other. This is partly caused by the inherent dichotomy between the approaches that researchers have taken to date. On one hand, disposable and low-cost devices[1-2] such as paper-based microfluidics[5-6] and other lateral flow assays[7] are excellent for performing detection assays on relatively simple samples such as urine[6] and serum.[8] They cannot however work with more complex sample matrices to detect rarer targets.[7,9] For example, the state-of-the-art mChip developed by Chin *et al*.[10] detects antibodies against HIV and *Treponema pallidum*, which can be captured from whole blood without preprocessing steps because they reside mainly in the serum. Devices like this would not be able to detect rare DNA found inside the blood cells without introducing steps to first lyse and process the sample. Conversely, sophisticated nanotechnology/microfluidics-based systems have been developed that can manage complex tasks such as the integration of lysing[11-12] and separation[13-14] steps and also target amplification through polymerase chain reaction.[11,15-16] Such advances have led to the development of integrated sample-in-answer-out systems for complex samples.[11,17] Unfortunately, the addition of multiple steps in one device is chiefly enabled through the incorporation of pumps, valves and electrical components and controllers, which increases their expense and operational complexity. To solve this problem, microfluidic methods must be developed that can be inexpensively and simply

implemented while allowing for basic flow manipulations such as actuation and valving that facilitate multi-step functions.

A multitude of microfluidic pumps and valves have been designed over the years,[18-19] many of which, including peristaltic[20-21] and electroosmotic[22] pumps, are very useful for research applications. They however often require complex microfabrication and integration of external components such as controllers and power supplies. To mitigate these issues, some devices have utilized stimuli-responsive materials either by treating the channels or the fluid medium to control flow autonomously in response to changes in the environment. Many of them utilize hydrogels that can either swell or change phase inside the channel to impede flow. For example, pH-actuated valves were pioneered by Beebe *et al*.[23] using a copolymerization of acrylic acid, 2-hydroxyethyl methacrylate, and ethylene dimethacrylate that swells or shrinks depending on the solution's pH. Recently, the field of optofluidics,[24] which shows promise in the area of point-of-care diagnostics,[3,25-26] has led to the employment of optical stimulation to guide flow. Liu *et al*.[27] for instance used a laser to heat gold nanoparticles near the liquid-air interface, which produced flow through an evaporation-condensation-coalescence process. Krishnan *et al*.[28] demonstrated dynamic flow reconfiguration through photo-thermally heating a Pluronic F127 solution, which created gelation regions that would redirect flow. While these techniques extended fluid control to within structurally simple microfluidic designs, the need to change the fluid medium during operation or modify it with additives such as Pluronic or nanoparticles requires pre- and post-processing steps and additional equipment, increasing the cost and difficulty of use.

A simple method to guide flow that does not involve altering the fluid or integrating traditional on-chip microvalves would minimize expense and fabrication complexity. Towards this goal, researchers have applied the thermoresponsive polymer poly(N-isopropylacrylamide) (PNIPAAm) in microfluidic environments to create externally-controllable valving.[29-31] PNIPAAm is a frequently used "smart" polymer due to its strong response to temperature, in that it transitions between expanded coils and compact globules as the temperature is varied around its lower critical solution temperature (LCST) of 32°C.[32-33] This is caused by the formation of H-bond networks below the LCST and the breakdown of those networks above the LCST, thereby making PNIPAAm hydrophilic at low temperatures and hydrophobic at high temperatures. In addition, it has been modified to achieve dramatic volume changes,[34-35] in which the material swells below the LCST and shrinks above the LCST. These properties have led to the application of PNIPAAm in drug delivery,[36-37] tissue engineering,[38-39] and microfluidics.[29,40] Within microfluidics, it has been modified in various ways to actuate[29] and valve[30] flows through temperature-controlled swelling. The hydrogel-based actuator developed by Harmon *et al*.[29] can manipulate flow without needing to alter the fluid, making it compatible with arbitrary fluid samples. The need to integrate Teflon spacers, resistive heaters and a secondary fluid layer however makes it fairly complex to fabricate and operate. A simpler design was created by Chen *et al*.,[30] in which a porous PNIPAAm-based monolith filled the microfluidic channel. Below the LCST, the monolith swells and closes the pores, while above the LCST, the pores open to allow fluid to be pumped through. A disadvantage of this design is that although the pores are open at high temperatures, the monolith surface would also be in the hydrophobic state. This means that it would not be able to passively drive flow through the device, but would

necessitate an external pump. In addition, small pore sizes may be incompatible with samples that include cells or other large molecules. Taking advantage of the inherent hydrophobicity of PNIPAAm at high temperatures to valve flow, Chunder *et al*.[31] designed open channels with valving capability by grafting glass surfaces using a layer-by-layer deposition of poly(allylamine hydrochloride) and silica nanoparticles, although heating was still produced through integrated microheaters.

In this paper, we create a simple device that passively pumps flow at room temperature and actively valves flow based on photo-thermal heating, thereby eliminating the need for external pumps, integrated valves or complex fabrication steps. We graft PNIPAAm via UV polymerization on PDMS microfluidic devices. The resulting channels are hydrophilic at room temperature and therefore passively pump flow via capillary action. When a specific region is heated to above 40°C, it impedes further flow. Light produced from a projector is reflected and focused onto the chip, where a thin layer of carbon black above the channel structure converts it into heat, valving flow at that location (Fig. 3.1a). We first optimize the grafting procedure to produce uniform surfaces on both pure PDMS and a carbon black-PDMS (CB-PDMS) tri-layer (Fig. 3.1b) and characterize the contact angle over a range of temperatures. We then extend the process to the inside of microfluidic channels and measure the passive capillary-driven flow rate as a function of temperature. Finally, we use a custom projector system to demonstrate light-driven flow control and calculate flow switching speed. To show its potential applicability towards integrated point-of-care devices, we present a bifurcating microfluidic design in Fig. 3.1c, where the inlet channel splits into two large chambers, with each chamber representing a

separate step of a multistage process. In step one, projector light is incident on the left or right channel, heating that region and valving off the flow, while flow continues down the adjacent hydrophilic path. In step two, the user removes the light, allowing flow to penetrate into the previously closed chamber (see Movie 3.S1). Our light-controlled capillary flow technique is capable of performing multiple flowing steps without the need for complex fabrication, external syringe pumps, integrated valves or modification of the fluid. Further, based on intensity measurements of our projected image, we assert that this technique could be extended to operate under sunlight without the need for any components other than a simple photomask and a lens. This in essence would afford inexpensive and power-free actuation and valving control, making it advantageous for point-of-care diagnostics in low-resource settings.

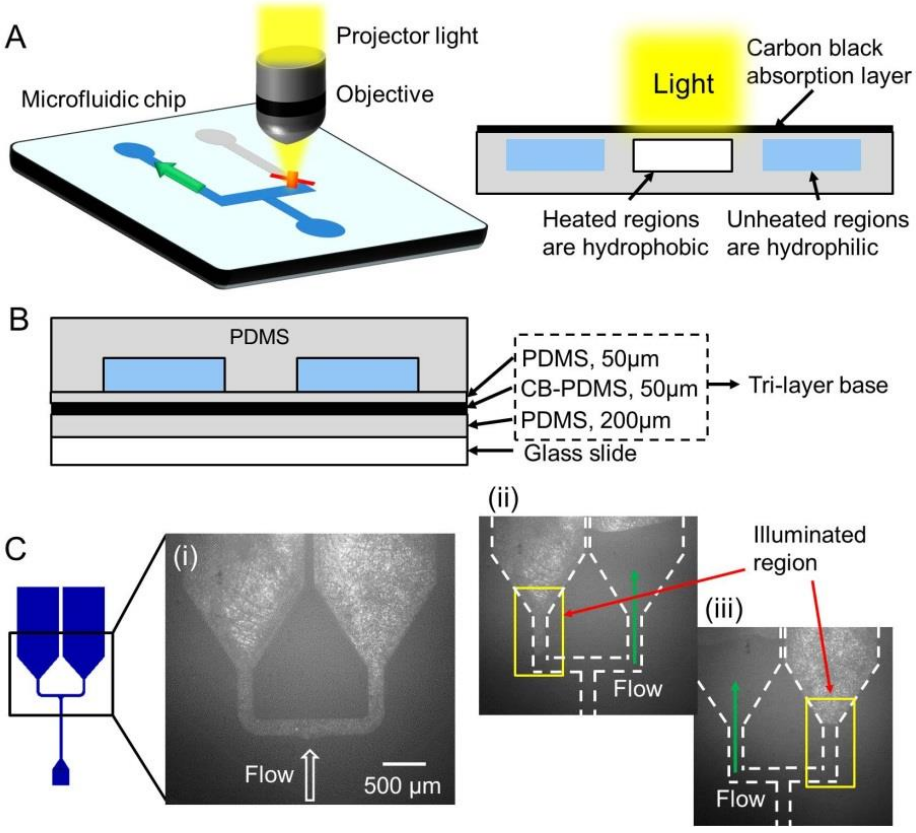

Figure 3.1. Light-governed flow actuation and manipulation. (a) Schematic of light-controlled microfluidic device. Light from a projector is focused through an objective onto an area of the channel, making that region hydrophobic. Flow cannot proceed down the heated path, but is instead drawn into the adjacent hydrophilic channel. (b) Microfluidic design, including the carbon black-PDMS tri-layer base, which is needed to graft PNIPAAm onto the surface. (c) Image of 2-chamber microfluidic device. The projected light, marked by yellow rectangles, is incident on either the (ii) left or (iii) right channel, preventing flow into that chamber while allowing flow to penetrate the adjacent one. (see Movie 3.S1)

3.3 Results and Discussion

To graft PNIPAAm onto PDMS, we followed the UV-mediated polymerization procedure developed by Schneider *et al*.[41-42] (see experimental section for more details). Briefly, we first ran a solution of 10 wt % benzophenone (BP) in acetone through the microchannel to allow BP to absorb into the PDMS. A degassed monomer solution of 20 wt % NIPAAm in DI water was then loaded into the microchannels and placed under a 100 W mercury arc lamp (Olympus, lens removed) at a bulb-to-chip distance of 14 cm for 15 min. Finally, the microchannels were flushed with ethanol for 1 h followed by rinsing with water for 2 h. We discovered that while this process worked for pure PDMS, the polymer would not graft onto a mixed CB-PDMS surface. After trying several different combinations, we found that a thin PDMS film above the CB-PDMS sheet and a thicker PDMS layer below it was necessary for successful grafting, resulting in the tri-layer base shown schematically in Figure 1b. We believe the thick bottom layer allows for more BP to enter the material and the thin top layer prevents any interference that carbon black may have on the UV-grafting step.

After optimizing the grafting procedure, we observed the surface under a microscope, which showed a highly wrinkled structure (Fig. 3.2a). The topography, measured using a P-10

profilometer, showed peaks about 10 µm wide by 10 µm deep. Under the same grafting procedure, the pure PDMS surface exhibited more densely packed wrinkles at an average of 35 peaks per mm versus 28 for the CB-PDMS tri-layer. We characterized the contact angles of the two surfaces and their response to temperature using a goniometer (Ramé-Hart Instrument Co.). A 10 µL droplet was placed on the surface and images were captured at 10 s intervals. We observed that when the surface is hydrophilic, a droplet exhibits dynamic wetting over the span of about a minute instead of immediately reaching the equilibrium contact angle (Fig. 3.2b, c). While studies have shown that PNIPAAm grafted onto a rough surface increases the change in contact angle,[43] to the best of our knowledge the gradual wetting observed here has not been previously reported for PNIPAAm-grafted surfaces. This wetting phenomenon is affected by both the chemistry and topography of the surface.[44-45] According to studies by McHale *et al*.,[44,46] the relationship between contact angle and time can be characterized by a power function $\theta \propto (t_0+t)^{-n}$, which, while derived using small angle approximations, is reasonably accurate even up to $\theta = 70°$. The exponent n should be 0.3 for a smooth and completely wetting surface and 0.75 if roughness dominates. At 25°C, where evaporation was minimal, we found n to be 0.347 (see Section 3.7), suggesting that roughness does not dominate for these tests. This is sensible as the characteristic wrinkle length is almost three orders of magnitude smaller than the droplet diameter. Due to the dynamic wetting process observed at lower temperatures, the equilibrium contact angle below 40°C is recorded when the advancing velocity reduces to less than 3 µm s^{-1}. Above 40°C, droplets exhibit no dynamic wetting effect, and therefore the contact angle is recorded immediately. As Figure 3.2d shows, the contact angle of the grafted pure PDMS surface changes from 30° at 30°C to 110° at 50°C.

Across the same temperature range, the contact angle of the tri-layer surface exhibits a slightly smaller shift from 40° to 95°, likely due to the less densely grafted surface.

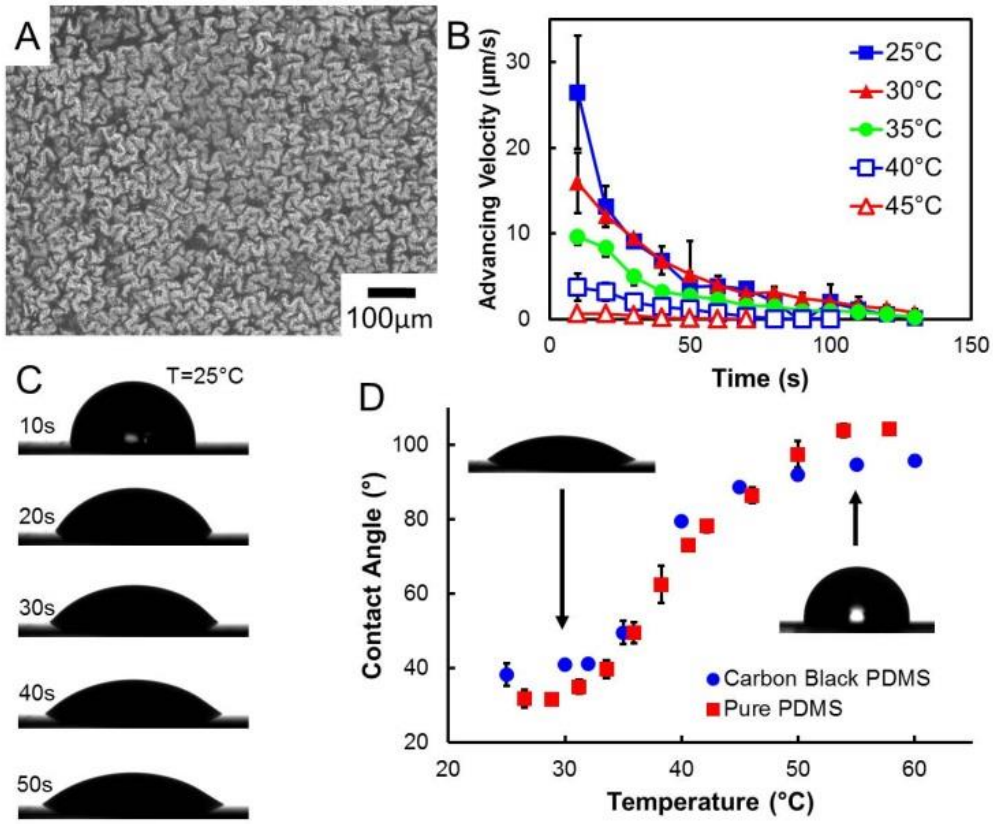

Figure 3.2. PNIPAAm grafted onto PDMS surfaces. (A) Successfully grafted PDMS surfaces produce a wrinkled structure with feature size on the order of 10□m. (B) The advancing interface velocity is plotted with time, showing that hydrophilic surfaces exhibit a wetting time of about a minute. (A) Shape of a droplet at room temperature as it spreads over time. (D) Contact angle of surface as a function of temperature. From 25°C to 40°C, contact angle is defined as when the advancing velocity becomes less than 3□m/s. Above 40°C, contact angle is recorded immediately.

We characterized the flow rate inside the microfluidic channel using the setup shown in Fig. 3.3a. Each test channel with a 0.2 × 1 mm cross section was placed on a hotplate. A CCD camera (PixelCam) attached to a stereoscope was used to visualize the interface location. A 10 µL droplet of DI water was placed at the inlet and the liquid penetration location is recorded. In

each experiment, the hotplate was used to heat the channel to the desired temperature, which was verified by a thermocouple. The contour of the liquid-air interface is marked in Matlab using custom code and the average location is recorded. Results show that the flow rate steadily decreases with increasing temperature up to 40°C, after which it becomes very low (Figure 3.3b, c). A closer examination above 45°C shows that the flow rate slightly increases with temperature. This is caused by the evaporation and condensation of the liquid, in which higher temperatures lead to more droplets forming in front of the interface (Figure 3.3d). Liu *et al*.[27] showed that by creating sharp temperature gradients, which increases the amount of condensation and coalescence, this phenomenon can be exploited to produce flow speeds up to 500 μm s^{-1}. Here, we apply a uniform temperature to a large area, thereby suppressing the flow even at high temperatures. Meanwhile, from room temperature to 40°C, flow can be tuned to a specific speed if necessary. Although droplet formation at the interface prevents a complete cessation of flow at temperatures above 40°C, we are able to achieve significant suppression of flow from 4 μl min^{-1} at room temperature to 0.1 μl min^{-1} at 40°C. If complete cessation of flow is required, it may be possible to use an adverse pressure gradient to counterbalance the small capillary force at 40°C. Based on a contact angle □ of 80° at 40°C, the capillary force calculated using $F = \gamma p \cos(\theta)$ is about 30 μN, where γ is surface tension and p is the channel's perimeter length. This can be offset with a 3 mm decrease in pressure head from the channel to the reservoir, assuming a reservoir cross sectional area of 1 mm^2, which can be designed into the microfluidic system.

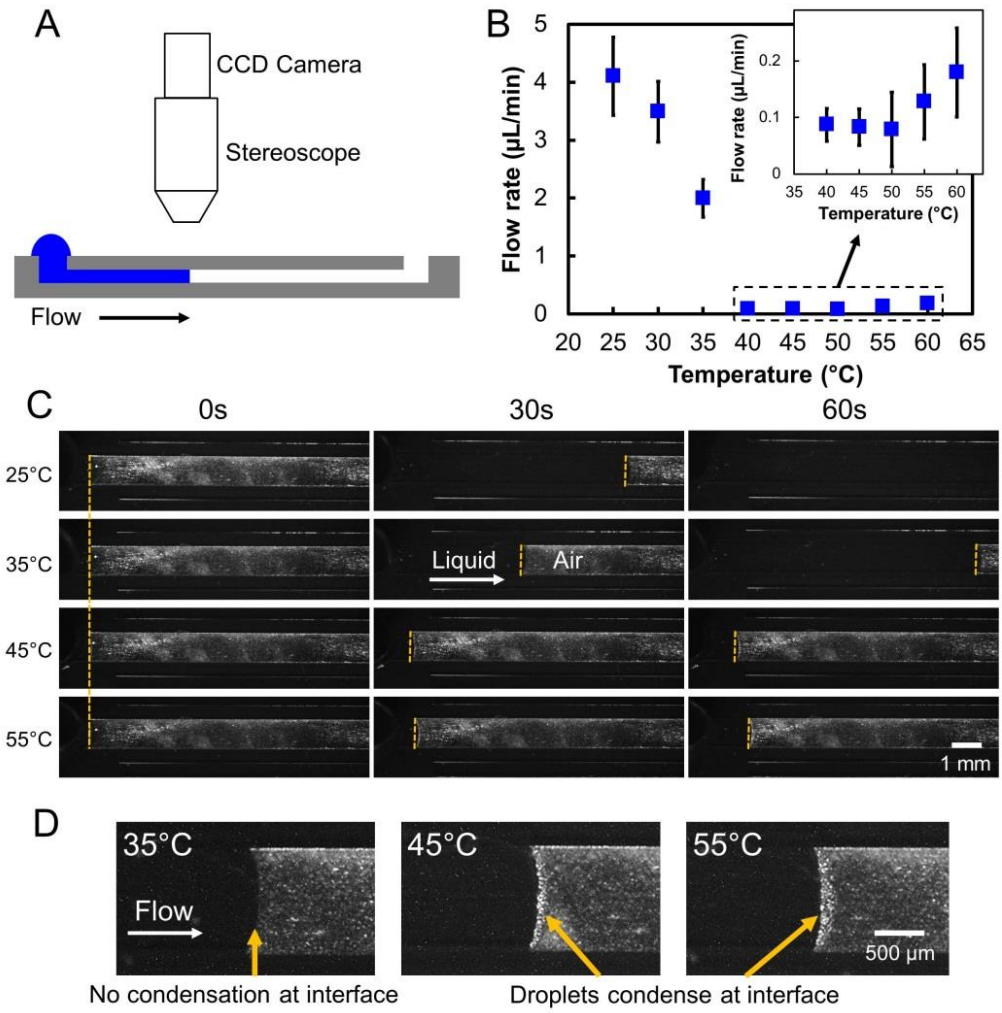

Figure 3.3. Flow rate characterization at various temperatures. (A) Schematic of imaging setup. A 10 □L water droplet is dispensed at the inlet, and the location of the interface is recorded by a CCD camera mounted on a stereoscope. (B) Plots showing average flow rate decreases with increasing temperature up to 40°C, after which the flow rate becomes very low. Inset plot shows that flow rate increases slightly at higher temperatures. (C) Locations of the liquid interface are marked by dashed lines, showing advancement rates at different temperatures. (D) Images showing droplet condensation at higher temperatures.

Following characterization of the flow rate, we proceeded to use a projector setup to demonstrate light-based flow manipulation. A projector (InFocus LP435z) with the projection lens removed was used as the light source, and a lens and mirror system (Thorlabs, Inc.) was set up to reflect and focus the image onto the microfluidic chip (see Krishnan *et al.*[28] for more

details). The images were created using Microsoft PowerPoint, and usually consisted of a white rectangle on a black background. The chip was placed upside down on an inverted microscope (Olympus IX71) and data was recorded using a CCD camera (PixelCam). The photo-thermal behavior of the chip was first characterized using Rhodamine B, a fluorescent dye for which the quantum yield is dependent on temperature. This allows for the use of fluorescence based imaging to perform *in situ* temperature measurements through tracking the intensity of the dye.[47-48] Based on calibrations performed by Samy *et al*.[49] and the generalized equations by Shah *et al*.,[50] we mapped the spatial and temporal changes in intensity to a temperature profile. A rectangular image with dimensions of around 1mm × 1.5mm is able to heat the chip to about 40°C (Fig. 3.4), the temperature needed for valving. Temperature profiles in the few seconds after the image is turned on and off are shown in Fig. 3.4b and indicate that the temperature changes very quickly due to the small size of the heated region. This is consistent with previous measurements by Krishnan *et al*.,[28] who determined a characteristic cooling time of about 2 s for images of similar size.

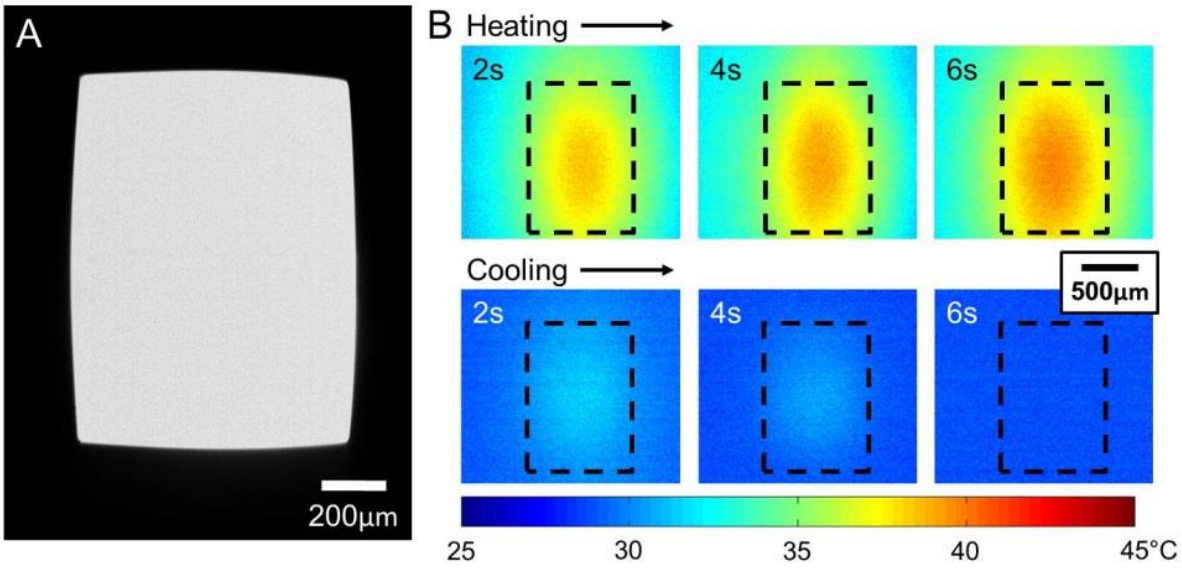

Figure 3.4. Thermal characterization using Rhodamine B. (A) Image size is adjusted to produce temperatures around 40°C. (B) High absorbance of carbon black and low thermal mass of PDMS lead to very fast heating and cooling times.

Finally, we demonstrate actuation and valving of flow using light (Fig. 3.5). Here, the channel inlet is connected to a scintillation vial of water via Tygon tubing, with the vial placed on a z-translation stage to fine-tune the meniscus height as to minimize gravitational effects between the channel and the reservoir. As Fig. 3.5a shows, light is initially shuttered off and liquid steadily flows into the channel. After 20 s, the shutter is opened and the water progression stops. After 30 additional seconds, light is switched off, and flow again continues into the channel. The fluid displacement and velocity through a series of on/off switching is show in Figure 3.5b, where the orange bars represent when light is on and the channel is heated. In Figure 3.5c, we characterize the normalized switching speed of our device. In the left graph, the channel is exposed to the light at the 5 s mark and we observe that flow is switched off within the next 4 s. This together with the Rhodamine B experimental results demonstrate that

the surface chemistry of the channel responds very quickly to the temperature change and that the system response is substantially governed by the heating time. The reaction time here is slightly faster than other recent swelling-based PNIPAAm valving, which require more than 6 s to close.[30,51] Increasing the flow rate however takes about 10 s to reach a steady velocity, likely linked to the gradual dynamic wetting phenomenon that we characterized previously, where a droplet required about a minute to reach a constant contact angle at low temperatures. Although this is slower than those demonstrated in other works, which showed opening times as low as 3 s (Table 3.S1), those values were calculated based on flow driven by syringe pumps,[30,51] whereas our device passively pumps the fluid through capillary action. In fact, because other swelling-based PNIPAAm valves mentioned previously would be hydrophobic when in the heated and shrunken state, some kind of pumping mechanism may be mandatory to achieve higher flow rates through the porous monolith, such as those demonstrated here.

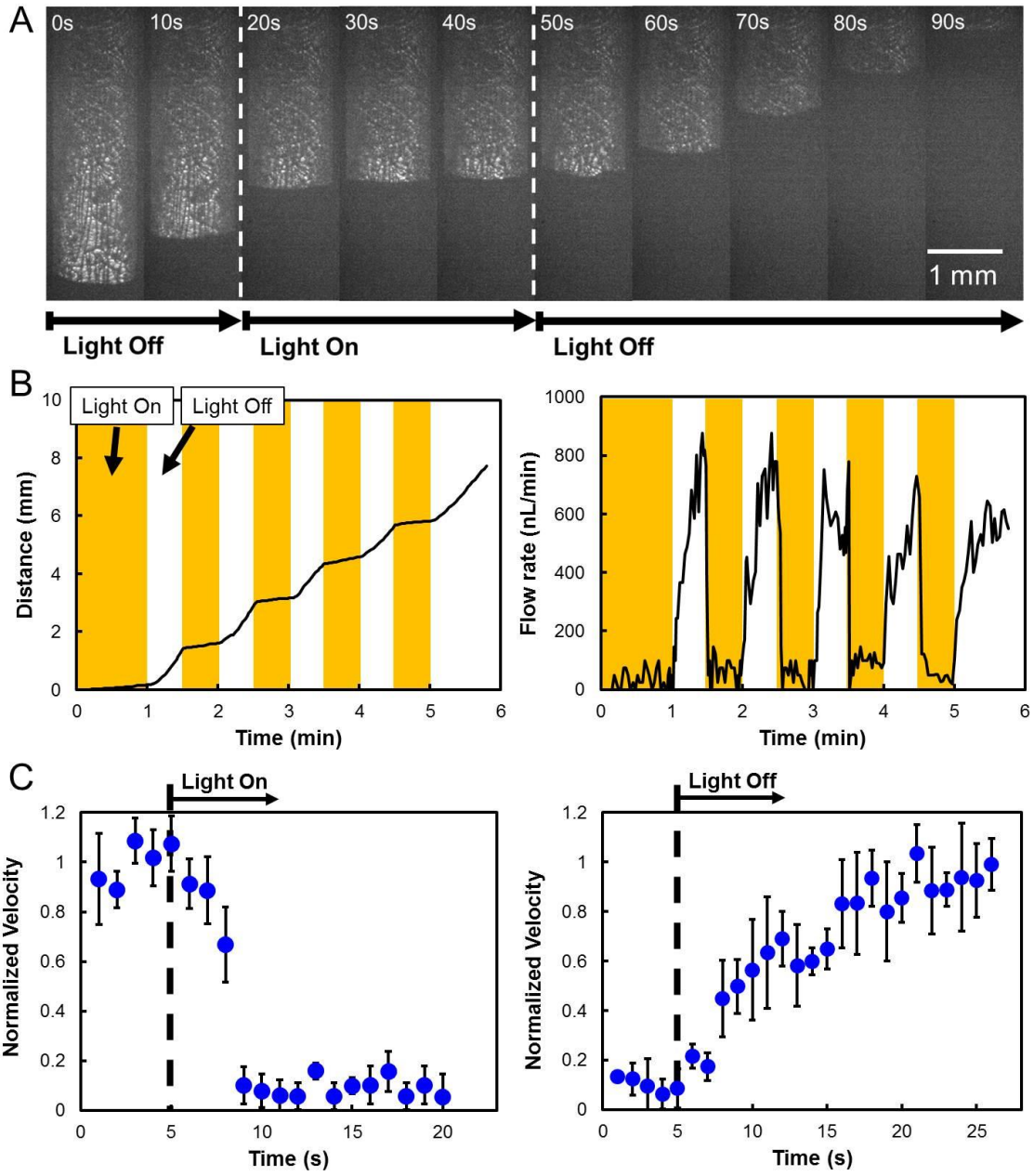

Figure 3.5. Flow actuation and valving demonstration. (A) Time-lapse images of liquid interface show liquid in motion when the light is off, stopping when light is turned on, and flowing again after the light is off. (B) Plot of the (left) location of the interface and (right) flow rate as light is switched on and off. Orange bars represent when light is on. (C) Average normalized velocities during switching of the light. (left) Flow is valved off within 4s of turning light on while (right) it takes about 10s for flow to reach a steady speed.

After characterizing the flow characteristics of this technique, we modified the system to remove the projector and laptop and instead use a simple lamp for heating and aluminum foil for masking. The revised setup is shown in Fig. 3.6. Here, the lamp shines on the entire microfluidic chip, and a sheet of aluminum foil is used to cover one side of a bifurcating channel (Fig. 3.6a). Fig. 3.6b shows the chip at the beginning of the test. A rectangular section of carbon black is placed under the channel, and the foil prevents the left side of this layer from heating. Water placed at the bottom inlet passively enters the channel. As Fig. 3.6c shows, by the time that water fills the left chamber, it still has not entered the right one. This test demonstrates the feasibility of using a general external light source such as a lamp or sunlight to control direction of flow without requiring any complex infrastructure.

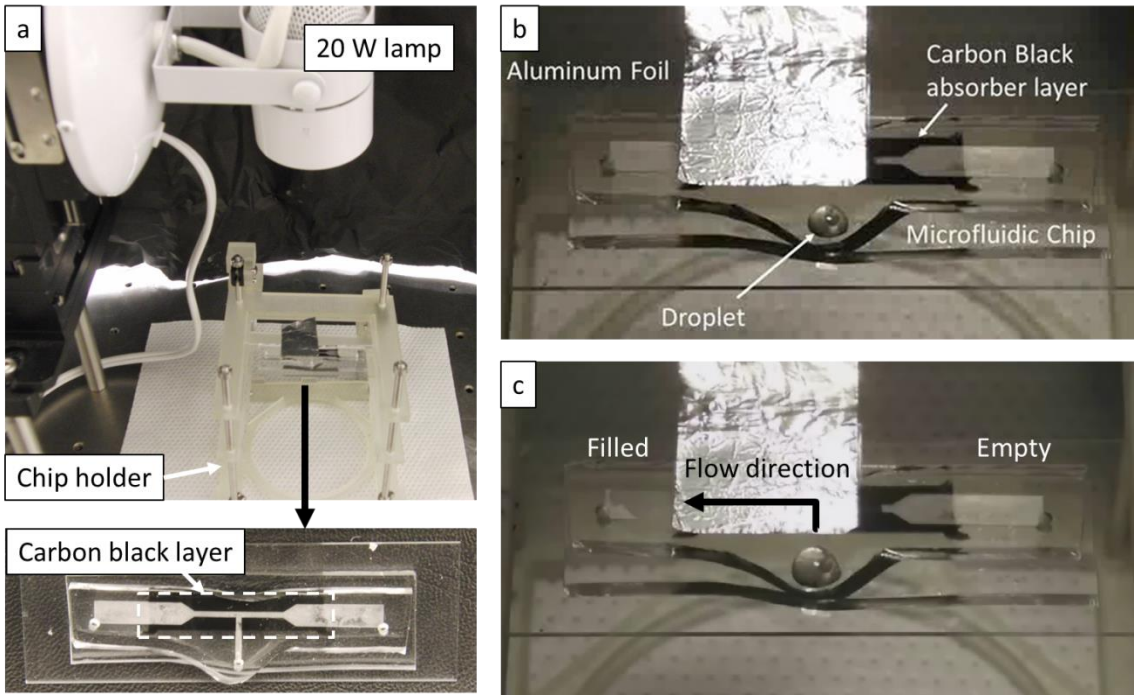

Figure 3.6. Lamp-guided flow. (a) Simplified flow guiding system using a lamp instead of a projector and laptop. (b) Masking on the chip is done by a sheet of aluminum foil. (c) By shining the lamp on the chip, the right channel is heated and valved off. Flow only enters the left chamber. (see Movie 3.S2)

To determine the feasibility of using solar-thermal energy to control such a device, it is important to consider the power requirements of the technique and also how variations in solar intensity, for example due to cloud coverage, could affect such a system. We first measured the power of the incident projector image using a power meter (Thorlabs PM100D, Sensor S121C) and a spectrometer (Ocean Optics HR4000) and calculated a value of 22.5 mW. Dividing this by the image area of about 1.5 mm^2, we arrive at an intensity of around 1.5×10^4 W m^{-2}. Although this is an order of magnitude higher than solar intensity, which is about 10^3 W m^{-2}, the total power required, and therefore temperature, can be obtained using sunlight in two simple ways. Increasing the area that light is incident on the chip or utilizing a lens to concentrate the light can be used either exclusively or in combination to obtain the desired total power from sunlight and achieve the temperatures necessary for valving. Therefore, it should be possible to design a microfluidic chip to function using only a lens to heat certain regions and a photomask to block the areas that must remain hydrophilic. A fully operational system would conceivably not require any complex components and would only need the user to periodically reposition the photomask. The ability to adjust the degree to which sunlight is concentrated would also allow the device to maintain usability despite potentially low solar intensities. For example, if on a cloudy day only 10% of maximum sunlight reaches the Earth's surface, a lens can be used to concentrate this sunlight by ten times to reach the same total power absorbed by the carbon black layer. Another concern is how variation of solar intensity due to motion of clouds would affect the device during use. We believe this problem can be considerably assuaged as long as the microfluidic system is designed such that regions that require valving remain at a temperature above 40°C. As determined in Fig. 3.3, flow is

essentially valved off above 40°C regardless of the actual temperature. This suggest that as long as a channel remains above 40°C, variations in solar intensity would not notably change the flow rate, and therefore minute-to-minute changes in cloud coverage should not be an issue.

3.4 Conclusion

We have developed a novel light-driven capillary flow technique that requires a very simple infrastructure, circumventing the need for external pumps and pre-fabricated valves. Unlike other PNIPAAm-functionalized valves that utilize physical swelling of monoliths, here we exploit changing the material's wetting property to actively switch the speed and direction of flow. This allows for an open hydrophilic channel at room temperature, which facilitates passive pumping, and hydrophobic valving of flow above 40°C using photo-thermal energy. The resulting system is able to valve on and off flow within a few seconds, which is comparable to other recent works that do require pumps or heaters. Similar to the simple microfluidics approaches discussed previously, our light-activated valving scheme is both easy to fabricate and simple to operate. In addition, it allows for potentially complex functions by supporting active flow guiding at user-defined locations and times. Finally, unlike other flow actuation techniques, this approach does not require the modification of the fluid medium or the construction of porous monoliths, which adds complexity to fabrication and may not be compatible with certain samples. From the intensity measurements of the projector image, we calculate that the same amount of heating using sunlight can be achieved by either increasing the incident light's area or by focusing the light via lensing. Based on these power calculations,

it should be possible to extend our technique to use solar energy to guide flow using only a lens and a photomask, representing a step towards power-free point-of-care diagnostics.

3.5 Experimental Section

3.5.1 Materials

PDMS (Sylgard 184 silicone elastomer) base and curing agent were purchased from Dow Corning. PNIPAAm and BP were purchased from Sigma-Aldrich. Rhodamine B was dissolved in DI water at a concentration of 1mM and stored in a refrigerator. The dye was diluted to a 50 µM concentration using carbonate buffer at a pH of 9.6 (Sigma Aldrich) prior to use.

3.5.2 Fabrication

Microfluidic Channel Fabrication: The PDMS channel was formed by spinning SU-8 2075 photoresist (Microchem) on silicon wafers at 1300 rpm for 30 s to obtain a 200 m thick film. The wafers were patterned through a chrome photomask (designed in L-Edit) using the ABM Contact Aligner at the Cornell Nanoscale Science and Technology Facility (CNF) and placed in SU-8 developer to remove unexposed material. PDMS (Sylgard 184 silicone elastomer) base and curing agent were used in a 10:1 ratio, poured over the SU-8 master and cured at 80°C.

The base of the device consisted of three layer (Figure 3.1b). First, a 200 µm thick PDMS layer was spin-coated onto a glass slide at 500 rpm for 45 s and cured at 80°C for 1 h. Above this, the photo-thermal absorption layer consisting of carbon black, PDMS A and PDMS B in a 0.01 : 1 : 0.05 weight ratio was spin coated at a rate of 1500 rpm to achieve a 50 µm-thin film and again

cured at 80°C. Finally, pure PDMS was spin-coated on top of the carbon black layer at 1500 rpm and cured at 80°C for an additional 50 µm-thin layer. This process is necessary because if either the 200 µm bottom layer or the 50 µm top layer is not present, NIPAAm could not be successfully grafted onto the surface. The tri-layer base is finally plasma bonded with the channel layer to create the microfluidic device.

UV-initiated graft polymerization of PNIPAAm: Grafting the channel surface was achieved by following the procedure developed by Schneider *et al*.[41-42], which we applied here to NIPAAm instead of poly(acrylic acid). A solution of 10 wt % BP in acetone was flowed through the microchannel by a syringe pump at 20 µL/min for 10 min and then flushed out with air. The chip was then vacuum-dried for 10 min inside a desiccator. A monomer solution of NIPAAm was prepared beforehand by mixing 20 wt % NIPAAm in DI water and initially degassed for 2 h and then for at least 30 min before each use to remove dissolved oxygen. The monomer solution was then loaded into the microchannels via a syringe pump, which was stopped once the entire device has been filled. The microfluidic chip was then placed on top of an ice pack under a 100 W mercury arc lamp (Olympus, lens removed) at a bulb-to-chip distance of 14 cm. Because the carbon black layer absorbs the UV light, an ice pack must be used to maintain the chip at a temperature below the LCST, which prevents phase transition and aggregation of the monomers.[52] The device is kept under UV illumination for 15 min. Afterwards, the microchannels are flushed with ethanol for 1 h followed by rinsing with water for 2 h. We recommend for any work with NIPAAm to be restricted under a fume hood as much as possible because it produces a strong odor that may last several days otherwise. The UV exposure time

of 15 min is fairly sensitive as we found that exposure times less than this produced increasingly less uniform surfaces while exposing for longer allowed aggregates to form inside the channel, which obstructed flow. The grafting is observable by eye, and successful grafting produces a uniform milky-white color on the channel (see Section 3.7). It may be possible for the procedure to be made more robust by reducing the incident UV intensity, either by using filters or increasing the lamp-to-chip distance and exposing for a longer time.

3.5.3 Photo-thermal valving experiments

The CB-PDMS absorber layer prevented visualization of the image during experiments because the light could not penetrate the carbon black. Therefore, the projector image was positioned and focused to the center of the screen before placing the microfluidic device on the microscope. During the flow/valving experiments, a shutter in front of the image was set to open and close in 30 s intervals. This was synchronized with when image recording started so that we could determine the frames at which the image is either blocked or exposed onto the chip.

3.6 Acknowledgements

The authors acknowledge funding from the National Science Foundation. The authors also appreciate access to the Cornell Nanoscale Science and Technology Facility (CNF) and the Nanobiotechnology Center (NBTC).

3.7 Supporting Information

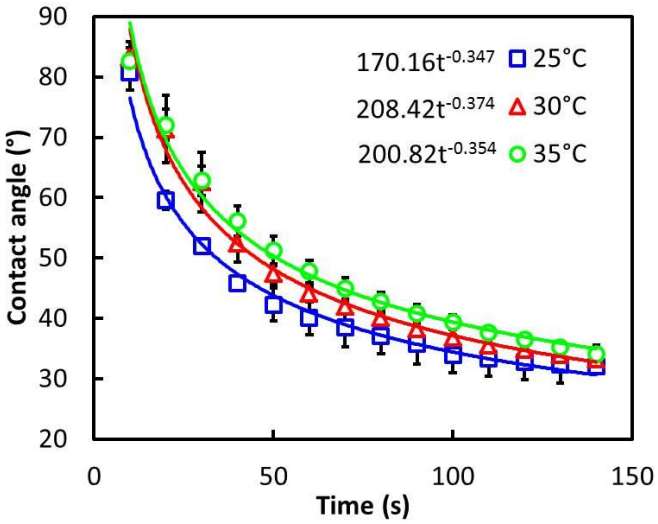

Figure 3.S1. **Dynamic contact angle change over time.** Data from 25°C to 35°C is plotted and fitted to a power law. The resulting exponents are around -0.35, which suggest that roughness does not dominate under these conditions.

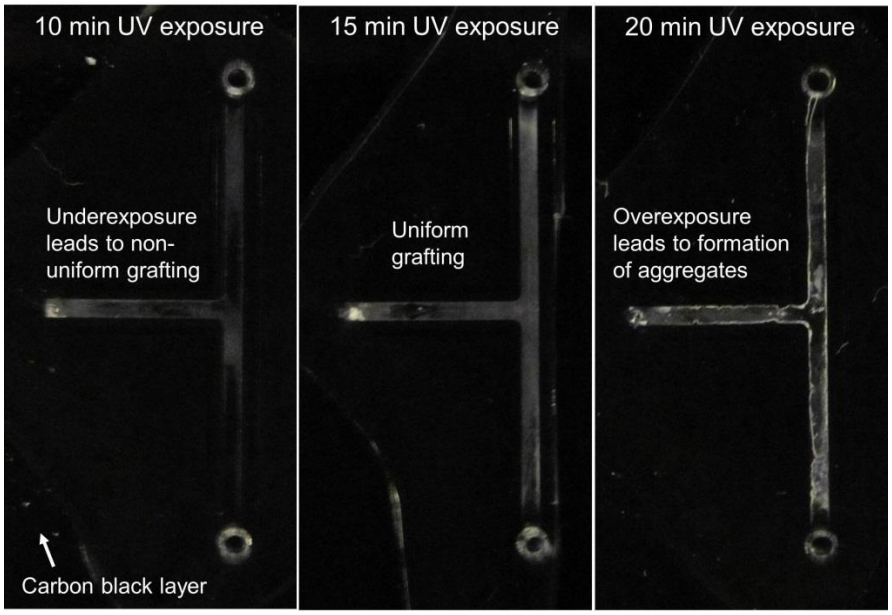

Figure 3.S2. Images of three chips exposed under UV for different durations. (Left) 10 min exposure results in non-uniformly grafted surface. (Center) 15 min exposure provides relatively uniform surface. (Right) 20 min exposure leads to formation of unwanted aggregates, which impede flow.

Table 3.S1 Comparison of light-guided flow technique to other microfluidic flow actuation techniques.

Work	Method	Powered pumping?	Alter fluid?	Opening time	Closing time	Flow rate	Notes
Harmon *et al.* 2003	PNIPAAm with heaters	Yes	No	1 min	1 min	*1 nL/min – 100 µL/min	Heat controlled peristaltic pump, complex fabrication
Sershen *et al.* 2005	PNIPAAm-co-AAm with laser	Yes	No	30 min	30 min	-	First demonstration of optothermal valving
Liu *et al.* 2006	Laser-heated nanoparticles	No	Yes	-	-	10 nL/min	High level of flow control
Martinez *et al.* 2008	Paper microfluidics	No	No	-	-	1 µL/min	Low level of flow control
Chen *et al.* 2008	PNIPAAm with heaters	Yes	No	4 s	6.2 s	5 µL/min	Heat-induced swelling/deswelling
Krishnan *et al.* 2009, 2012	Pluronic F127	Yes	Yes	~1 s	~1 s	40 nL/min	Optothermally-induced gellation, leakage issues
Jiang *et al.* 2012	**surface grafted PNIPAAm**	**No**	**No**	**10 s**	**4 s**	**1 µL/min**	**Optothermally-induced surface chemistry change**

3.8 Supplementary videos

Movie 3.S1 Light-guided flow actuation. A bifurcating channel is grafted with PNIPAAm, and a projector image is shined on the left channel to render its surface hydrophobic. As water enters the system, it is drawn into the right chamber but does not enter the left one. After the light is turned off, water fills the left chamber as well.

Movie 3.S2 Lamp-guided flow with minimal infrastructure. The same effect seen in Movie 3.S1 is shown here, however now the light source is a general purpose lamp, and the masking is done by a sheet of aluminum foil. The region covered by the foil does not absorb the lamp light and remains a hydrophilic surface to draw water through.

REFERENCES

1 Yager, P. et al. Microfluidic diagnostic technologies for global public health. Nature 442, 412-418 (2006).

2 Weigl, B., Domingo, G., LaBarre, P. & Gerlach, J. Towards non- and minimally instrumented, microfluidics-based diagnostic devices. Lab Chip 8, 1999-2014 (2008).

3 Myers, F. B. & Lee, L. P. Innovations in optical microfluidic technologies for point-of-care diagnostics. Lab Chip 8, 2015-2031 (2008).

4 Yeo, L. Y., Chang, H. C., Chan, P. P. Y. & Friend, J. R. Microfluidic Devices for Bioapplications. Small 7, 12-48 (2011).

5 Pelton, R. Bioactive paper provides a low-cost platform for diagnostics. Trac-Trend. Anal. Chem. 28, 925-942 (2009).

6 Martinez, A. W., Phillips, S. T., Whitesides, G. M. & Carrilho, E. Diagnostics for the Developing World: Microfluidic Paper-Based Analytical Devices. Anal. Chem. 82, 3-10 (2010).

7 Posthuma-Trumpie, G. A., Korf, J. & van Amerongen, A. Lateral flow (immuno) assay: its strengths, weaknesses, opportunities and threats. A literature survey. Anal. Bioanal. Chem. 393, 569-582 (2009).

8 Dungchai, W., Chailapakul, O. & Henry, C. S. Electrochemical Detection for Paper-Based Microfluidics. Anal. Chem. 81, 5821-5826 (2009).

9 Gubala, V., Harris, L. F., Ricco, A. J., Tan, M. X. & Williams, D. E. Point of Care Diagnostics: Status and Future. Anal. Chem. 84, 487-515 (2012).

10 Chin, C. D. et al. Microfluidics-based diagnostics of infectious diseases in the developing world. Nat. Med. 17, 1015-U1138 (2011).

11 Easley, C. J. et al. A fully integrated microfluidic genetic analysis system with sample-in-answer-out capability. Proc. Natl. Acad. Sci. USA 103, 19272-19277 (2006).

12 Church, C., Zhu, J. J., Huang, G. H., Tzeng, T. R. & Xuan, X. C. Integrated electrical concentration and lysis of cells in a microfluidic chip. Biomicrofluidics 4 (2010).

13 Wu, D. P., Qin, J. H. & Lin, B. C. Electrophoretic separations on microfluidic chips. J. Chromatogr. A 1184, 542-559 (2008).

14 Strychalski, E. A., Henry, A. C. & Ross, D. Expanding the Capabilities of Microfluidic Gradient Elution Moving Boundary Electrophoresis for Complex Samples. Anal. Chem. 83, 6316-6322 (2011).

15 Heyries, K. A. et al. Megapixel digital PCR. Nat. Methods 8, 649-U664 (2011).

16 Manage, D. P. et al. On-chip PCR amplification of genomic and viral templates in unprocessed whole blood. Microfluid. Nanofluid. 10, 697-702 (2011).

17 Ferguson, B. S. et al. Genetic Analysis of H1N1 Influenza Virus from Throat Swab Samples in a Microfluidic System for Point-of-Care Diagnostics. J. Am. Chem. Soc. 133, 9129-9135 (2011).

18 Laser, D. J. & Santiago, J. G. A review of micropumps. J. Micromech. Microeng. 14, R35-R64 (2004).

19 Iverson, B. D. & Garimella, S. V. Recent advances in microscale pumping technologies: a review and evaluation. Microfluid. Nanofluid. 5, 145-174 (2008).

20 Unger, M. A., Chou, H. P., Thorsen, T., Scherer, A. & Quake, S. R. Monolithic microfabricated valves and pumps by multilayer soft lithography. Science 288, 113-116 (2000).
21 Yobas, L., Tang, K. C., Yong, S. E. & Ong, E. K. Z. A disposable planar peristaltic pump for lab-on-a-chip. Lab Chip 8, 660-662 (2008).
22 Piyasena, M. E., Newby, R., Miller, T. J., Shapiro, B. & Smela, E. Electroosmotically driven microfluidic actuators. Sensor. Actuat. B-Chem. 141, 263-269 (2009).
23 Beebe, D. J. et al. Functional hydrogel structures for autonomous flow control inside microfluidic channels. Nature 404, 588-590 (2000).
24 Psaltis, D., Quake, S. R. & Yang, C. H. Developing optofluidic technology through the fusion of microfluidics and optics. Nature 442, 381-386 (2006).
25 Brennan, D., Justice, J., Corbett, B., McCarthy, T. & Galvin, P. Emerging optofluidic technologies for point-of-care genetic analysis systems: a review. Anal. Bioanal. Chem. 395, 621-636 (2009).
26 Fan, X. D. & White, I. M. Optofluidic microsystems for chemical and biological analysis. Nat. Photonics 5, 591-597 (2011).
27 Liu, G. L., Kim, J., Lu, Y. & Lee, L. P. Optofluidic control using photothermal nanoparticles. Nat. Mater. 5, 27-32 (2006).
28 Krishnan, M. & Erickson, D. Optically induced microfluidic reconfiguration. Lab Chip 12, 613-621 (2012).
29 Harmon, M. E., Tang, M. & Frank, C. W. A microfluidic actuator based on thermoresponsive hydrogels. Polymer 44, 4547-4556 (2003).
30 Chen, G. F., Svec, F. & Knapp, D. R. Light-actuated high pressure-resisting microvalve for on-chip flow control based on thermo-responsive nanostructured polymer. Lab Chip 8, 1198-1204 (2008).
31 Chunder, A., Etcheverry, K., Londe, G., Cho, H. J. & Zhai, L. Conformal switchable superhydrophobic/hydrophilic surfaces for microscale flow control. Colloid. Surface. A 333, 187-193 (2009).
32 Rzaev, Z. M. O., Dincer, S. & Piskin, E. Functional copolymers of N-isopropylacrylamide for bioengineering applications. Prog. Polym. Sci. 32, 534-595 (2007).
33 Sun, T. L. & Qing, G. Y. Biomimetic Smart Interface Materials for Biological Applications. Adv. Mater. 23, H57-H77 (2011).
34 Zhang, J. T., Bhat, R. & Jandt, K. D. Temperature-sensitive PVA/PNIPAAm semi-IPN hydrogels with enhanced responsive properties. Acta Biomater. 5, 488-497 (2009).
35 Zhang, X. Z. & Chu, C. C. Fabrication and characterization of microgel-impregnated, thermosensitive PNIPAAm hydrogels. Polymer 46, 9664-9673 (2005).
36 Zhang, X. Z., Lewis, P. J. & Chu, C. C. Fabrication and characterization of a smart drug delivery system: microsphere in hydrogel. Biomaterials 26, 3299-3309 (2005).
37 Yavuz, M. S. et al. Gold nanocages covered by smart polymers for controlled release with near-infrared light. Nat. Mater. 8, 935-939 (2009).
38 Da Silva, R. M. P., Mano, J. F. & Reis, R. L. Smart thermoresponsive coatings and surfaces for tissue engineering: switching cell-material boundaries. Trends Biotechnol. 25, 577-583 (2007).

39 Tekin, H. et al. Responsive Microgrooves for the Formation of Harvestable Tissue Constructs. Langmuir 27, 5671-5679 (2011).
40 Chen, J. K. & Li, J. Y. Synthesis of tethered poly(N-isopropylacrylamide) for detection of breast cancer recurrence DNA. J. Colloid Interf. Sci. 358, 454-461 (2011).
41 Schneider, M. H., Willaime, H., Tran, Y., Rezgui, F. & Tabeling, P. Wettability Patterning by UV-Initiated Graft Polymerization of Poly(acrylic acid) in Closed Microfluidic Systems of Complex Geometry. Anal. Chem. 82, 8848-8855 (2010).
42 Schneider, M. H., Tran, Y. & Tabeling, P. Benzophenone Absorption and Diffusion in Poly(dimethylsiloxane) and Its Role in Graft Photo-polymerization for Surface Modification. Langmuir 27, 1232-1240 (2011).
43 Sun, T. L. et al. Reversible switching between superhydrophilicity and superhydrophobicity. Angew. Chem. Int. Edit. 43, 357-360 (2004).
44 McHale, G., Shirtcliffe, N. J., Aqil, S., Perry, C. C. & Newton, M. I. Topography driven spreading. Phys. Rev. Lett. 93 (2004).
45 Gao, N. & Yan, Y. Y. Characterisation of surface wettability based on nanoparticles. Nanoscale 4, 2202-2218 (2012).
46 McHale, G., Newton, M. I. & Shirtcliffe, N. J. Dynamic wetting and spreading and the role of topography. J. Phys.-Condens. Mat. 21 (2009).
47 Ross, D., Gaitan, M. & Locascio, L. E. Temperature measurement in microfluidic systems using a temperature-dependent fluorescent dye. Anal. Chem. 73, 4117-4123 (2001).
48 Erickson, D., Sinton, D. & Li, D. Q. Joule heating and heat transfer in poly(dimethylsiloxane) microfluidic systems. Lab Chip 3, 141-149 (2003).
49 Samy, R., Glawdel, T. & Ren, C. L. Method for microfluidic whole-chip temperature measurement using thin-film poly(dimethylsiloxane)/Rhodamine B. Anal. Chem. 80, 369-375 (2008).
50 Shah, J. J., Gaitan, M. & Geist, J. Generalized Temperature Measurement Equations for Rhodamine B Dye Solution and Its Application to Microfluidics. Anal. Chem. 81, 8260-8263 (2009).
51 Li, Z. M., He, Q. H., Ma, D. & Chen, H. W. On-chip integrated multi-thermo-actuated microvalves of poly(N-isopropylacrylamide) for microflow injection analysis. Anal. Chim. Acta 665, 107-112 (2010).
52 Ebara, M., Hoffman, J. M., Stayton, P. S. & Hoffman, A. S. Surface modification of microfluidic channels by UV-mediated graft polymerization of non-fouling and 'smart' polymers. Radiat. Phys. Chem. 76, 1409-1413 (2007).

CHAPTER 4

SOLAR THERMAL POLYMERASE CHAIN REACTION FOR SMARTPHONE-ASSISTED MOLECULAR DIAGNOSTICS[3]

4.1 Abstract

Nucleic acid-based diagnostic techniques such as polymerase chain reaction (PCR) are used extensively in medical diagnostics due to their high sensitivity, specificity and quantification capability. In settings with limited infrastructure and unreliable electricity, however, access to such devices is often limited due to the highly specialized and energy-intensive nature of the thermal cycling process required for nucleic acid amplification. Here we integrate solar heating with microfluidics to eliminate thermal cycling power requirements as well as create a simple device infrastructure for PCR. Tests are completed in less than 30 min, and power consumption is reduced to 80 mW, enabling a standard 5.5 Wh iPhone battery to provide 70 h of power to this system. Additionally, we demonstrate a complete sample-to-answer diagnostic strategy by analyzing human skin biopsies infected with Kaposi's Sarcoma herpesvirus (KSHV/HHV-8) through the combination of solar thermal PCR, HotSHOT DNA extraction and smartphone-based fluorescence detection. We believe that exploiting the ubiquity of solar thermal energy as demonstrated here could facilitate broad availability of nucleic acid-based diagnostics in resource-limited areas.

[3] Reprinted from Li Jiang, Matthew Mancuso, Zhengda Lu, Gunkut Akar, Ethel Cesarman, and David Erickson, "Solar thermal polymerase chain reaction for smartphone-assisted molecular diagnostics," Scientific Reports 4, Article number: 4137

4.2 Introduction

Polymerase chain reaction (PCR)[1] is widely used in nucleic acid-based diagnostics due to its high sensitivity, specificity and quantification capability[2-5]. Unfortunately, regions with minimal infrastructure and unreliable electricity often have limited access to such tools partly due to the relatively complex and energy-intensive nature of the thermal cycling process required for DNA amplification[3-5]. The need for diagnostic tests appropriate for point-of-care (POC) applications can be illustrated by Kaposi's Sarcoma (KS)[6,7], a cancer caused by Kaposi's Sarcoma herpesvirus (KSHV). In sub-Saharan Africa, KS is associated with significant morbidity and mortality in adults and children[8] and may be difficult to diagnose for several reasons. Various cutaneous lesions can clinically mimic KS, and overlapping histological features can make it challenging to distinguish KS from several other angioproliferative diseases[9]. In addition, serological tests for KSHV antibodies are unreliable because a KSHV infection is not necessarily sufficient for KS development, and over half of the population in endemic regions is serologically positive for this virus[7]. Similarly, performing viral detection in peripheral blood is inaccurate as not all KS patients have KSHV viremia while HIV+ patients without KS can exhibit KSHV viremia[10]. Performing PCR on viral DNA extracted from skin biopsies has demonstrated high sensitivity and specificity[6], however high power and specialized equipment needs have been substantial obstacles against implementing PCR in POC settings.

Typically, PCR involves repeatedly cycling a sample through 95°C (denaturation), 60°C (annealing) and 72°C (extension) to achieve an exponential increase in target DNA. One of the lowest power devices was demonstrated by Wheeler *et al.*[11], which expended 370 mW using

convective PCR. Since then, works that have used smaller sample volumes or isothermal techniques have shown minimal improvement in power consumption. Additionally, such techniques often lead to trade-offs between simplicity, speed, reaction stability, throughput and power consumption[12-16]. Based on these works, a standard 5.5 Wh smartphone battery fully committed to heating such a system would last between 8 to 15 h. It is also important to note here that compared to these low power PCR techniques, both commercially available integrated nucleic acid-based devices as well as those found in recent literature typically require at least an order of magnitude more power. For example, the isothermal Gene-Z system developed by Stedtfeld *et al*.[17] uses a lithium polymer battery that needs to be recharged after 4 h of operation. Based on the battery's power capacity, we estimate that the system consumes about 10 W during use. A 5.5 Wh smartphone battery would therefore enable 30 min of use before being depleted. Another example is the rapid PCR technique developed by Maltezos *et al*.[18], which achieved ultrafast thermal cycling speed of about 3 s per cycle but consumed 400 W. A smartphone battery in this case would enable 1 min of use. In our system, solar thermal energy is utilized to drive nucleic acid amplification in a microfluidic chip. Using a smartphone for temperature sensing, the power consumption is reduced to 80 mW, representing a 2-orders of magnitude improvement compared to other state-of-the-art systems. An evaluation of techniques developed in the literature and commercially available devices is presented in Table 4.S1.

4.3 Results

4.3.1 Development and verification of solar thermal PCR

With recent advancements in the field of optofluidics[19], sunlight is finding a number of novel applications in both energy[20,21] and global health[22]. Here we create solar thermal PCR, which eliminates the energy burden for nucleic acid amplification by employing sunlight to perform thermal cycling. Fig. 4.1a shows the device, which holds a 75 mm diameter glass lens and a movable 50 mm diameter PCR chip. These components are held on a 100° tilting stage, allowing the lens and chip to be positioned to face the sun throughout the day. Alignment between the chip and the sun is achieved by ensuring that the bright circle that the sun makes overlaps with the chip. Typically, the bright circle is several millimeters larger than the chip region that is heated, allowing for a relatively large tolerance in alignment. On the chip, the focused sunlight passes through a ring-shaped mask and is converted into heat by an absorber layer. Due to the masking of light in specific regions, three temperature zones at 95°C (denaturation), 72°C (extension) and 60°C (annealing) are created along the radius of the chip. A microfluidic channel then repeatedly guides a sample through these three zones for 35 cycles. The channel geometry dictates an approximate residence time ratio of 1:3:1 (denaturation:extension:annealing), effectively creating the thermal conditions that induce PCR. This microfluidic technique, known as continuous-flow PCR[23,24], has exhibited fast reaction speeds[24], minimal cross-contamination[25], high throughput[26], and facilitates microfluidic device integration[13], making it highly attractive for POC applications. Three thermocouples in the chip are connected by a microcontroller (Fig. 4.1b) to a smartphone and a custom app measures the on-chip temperatures throughout the test (Fig. 4.1c and Fig. 4.S1). Above the thermocouples is the mask, comprised of three nested aluminum foil rings (Fig. 4.1d). Below the thermocouples is a disposable piece containing the light absorber and the microfluidic channel (Fig. 4.1e). The

absorber is made from a carbon black and PDMS mixture, which was shown previously to allow no light transmission within the visible spectrum at the same concentration and thickness as the present work[27]. In addition, carbon black powder was shown to have excellent broadband absorption[28] across the spectrum. We therefore assume the solar thermal energy conversion of the carbon black itself is nearly 100% efficient because the vast majority of the absorbed light energy is necessarily converted into heat. To characterize the effect of the PDMS on the absorber's photo-thermal efficiency, we measured the intensity of sunlight after passing through a clear 1 mm thin PDMS film using a powermeter. The 1 mm PDMS thickness is consistent with the thickness of the PDMS above the carbon black layer. The power lost through the film was measured to be 5%. This is supported by Cai et al.[29], which showed excellent transmittance of PDMS below 1200 nm. The entire absorber therefore is estimated to be about 90% to 95% efficient. Details on device fabrication are available in Section 4.7.

To demonstrate solar thermal PCR in the range of KSHV DNA counts expected from a punch biopsy, we amplified plasmid samples with starting DNA concentrations ranging from 10^8 to 10 copies/µL, shown in Fig. 4.1f. A 164-base pair (bp) segment of the KSHV gene vCyclin was selected as the target because the sequence is unique and conserved among different strains (Table 4.S2). Bands appeared for all samples when analyzed by gel electrophoresis (Fig. 4.S2). PCR dependence on flow rate was also analyzed to determine the fastest speed with which a test can be performed. We conducted experiments using 10 µL samples with cycling times ranging from 5 s/cycle to 50 s/cycle. This range corresponded to total reaction times of 6 min to 55 min (Fig. 4.1g), which was defined as the time taken between when the front end of the

sample enters the chip and when the back end exits the chip. Band intensity increased significantly near 20 s/cycle (Fig. 4.S2), showing that a 10µL sample can be amplified and extracted within 30 min. Details on DNA count estimation and plasmid extraction are available in Section 4.7.

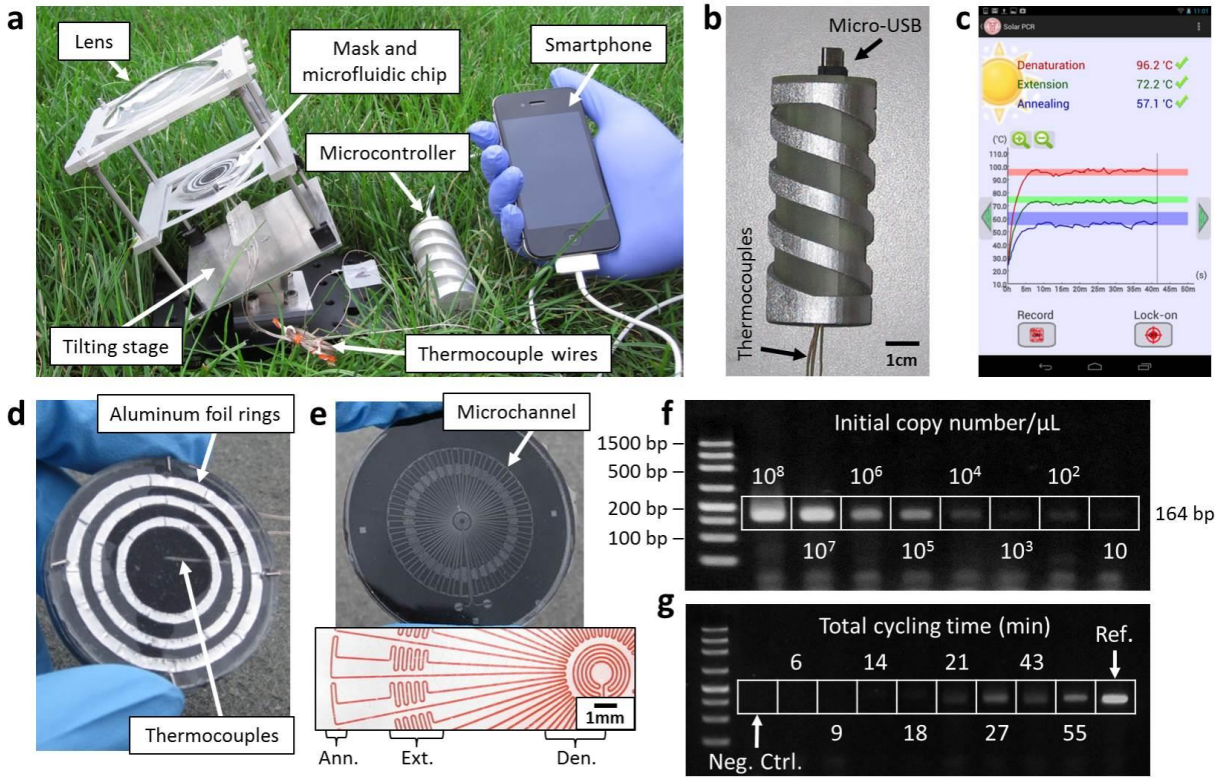

Fig. 4.1. Solar thermal PCR system. a, the benchtop component holds the lens, the PCR chip and a rotational stage. **b**, Thermocouples on the chip are connected by a microcontroller to a smartphone. **c**, a screenshot shows the app recording the temperatures over time. **d**, the top of the PCR chip contains the mask and the thermocouples. **e**, the bottom includes the absorber layer and the microfluidic channel, with marked regions for annealing, extension and denaturation (inset). **f**, amplification over a range of concentrations. **g**, amplification over a range of cycling speeds. The typical extension rate of *Taq* polymerase is 60-100 nucleotides/s at 72°C. Thus, 3 s should be sufficient for full extension of a 164 bp product. The design of our channel suggests that a minimum reaction time of 10 s/cycle is required. The band intensity began decreasing for reaction times faster than 20 s/cycle, and no band was observed for reactions faster than 10 s/cycle. Intensity values were normalized by a reference sample that was run in a conventional thermal cycler for 2 h.

4.3.2 Demonstration of solar thermal PCR under a variety of ambient conditions

Although changes in solar intensity and ambient temperature can affect on-chip temperatures, we mitigate the issue by simply adjusting the distance between the lens and the chip, illustrated in Fig. 4.2a. This adjustment is done manually based on temperature feedback provided by the app. Changing the lens-to-chip distance in turn changes the intensity of the sunlight absorbed by the chip, which compensates for different ambient temperatures and allows the system to function under a range of conditions. Based on simulations (Fig. 4.S3), we designed the masking rings such that the thermal profile generated by the masked light exhibits plateaus near 95°C, 72°C and 60°C for a given solar intensity and ambient temperature (Fig. 4.2b). The chip can then be lowered to increase solar heating on cooler days and raised to reduce heating on warmer days. Fig. 4.2c shows temperatures obtained in April (10°C ambient) and May (27°C ambient) of 2013 in Ithaca, NY using the same mask. For these measurements, the lens-to-chip distance was first set to 85 mm to quickly heat the chip. Once temperatures near PCR requirements were reached, the distance was reduced to 79 mm in April or 68 mm in May. Through this process, on-chip temperature changes were minimized to 3°C for denaturation and extension and 6°C for annealing. Simulations suggest that over the range of 0°C to 30°C roughly 75% to 50% of peak insolation (1000 W/m^2) is sufficient for PCR (Fig. 4.2c (iii)).

After having developed the solar thermal PCR system to work under a range of conditions, we demonstrated that PCR can be performed for approximately 12 h each day during the summer months. Fig. 4.2d shows on-chip temperatures in July from 7 AM to 7 PM. By setting the lens-

to-chip distance at 85 mm, the necessary temperatures were usually obtained within 3 min, while longer times were required in the morning when ambient temperature is cooler and sunlight is less intense. For the data presented, temperatures varied from 25°C in the morning to 32°C in the early afternoon. Fig. 4.2e shows that as the day warmed in the morning, the denaturation temperature decreased while the extension and annealing temperatures increased. The trends were reversed in the late afternoon as ambient temperature cooled. For these experiments, the lens-to-chip distance and the tilt were both readjusted for each new test, however no adjustment was required within each test after PCR temperatures were reached. In practice, a set of different masks can be provided to the user, each having been optimized for a specific temperature range. Fig. 4.2f demonstrates that PCR can be successfully performed for most of the daylight hours, although larger thermal fluctuations, particular for tests at 12:00 PM and 6:00 PM, may have caused reduced amplification efficiency, as shown by the decrease in band intensity (see Fig. 4.S4 and Fig. 4.S5).

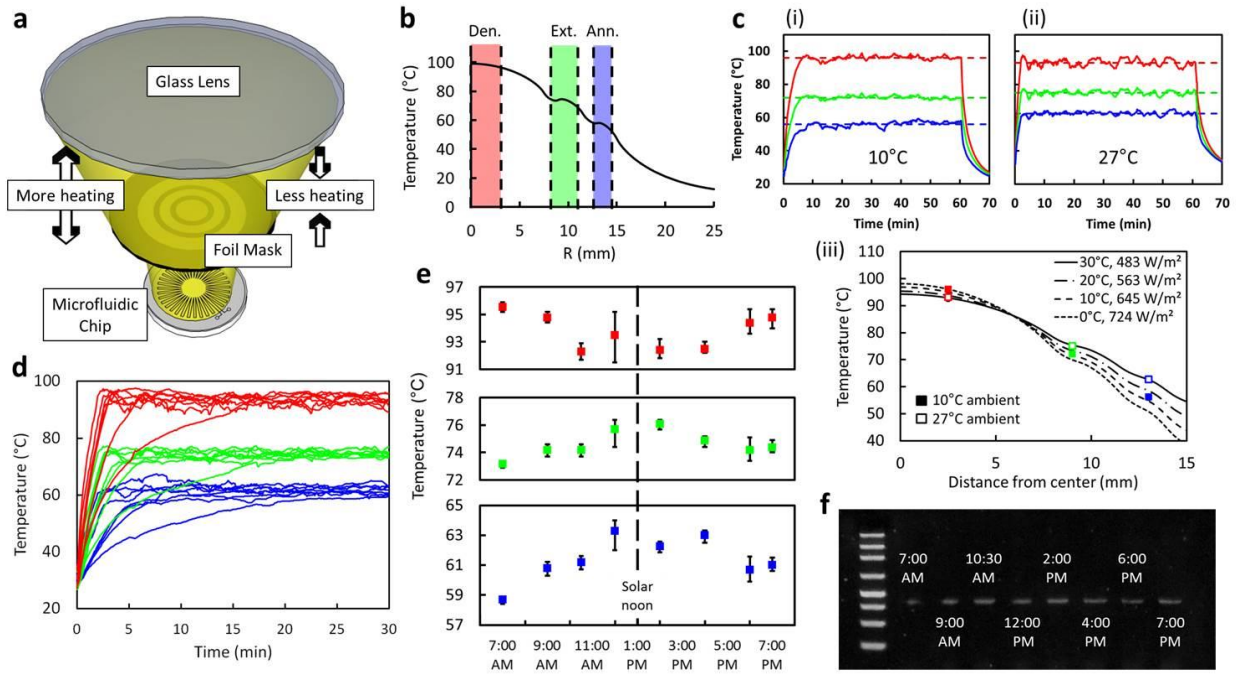

Fig. 4.2. Thermal characterization and demonstration of solar thermal PCR. a, schematic showing the ability to change the solar intensity by changing the lens-to-chip distance. **b**, a simulation showing the plateaued temperature profile at the plane of the microchannel. **c**, measurements in (i) April and (ii) May demonstrate the ability to achieve similar on-chip temperatures using the same mask. (iii) Simulations provide thermal profiles from 0°C to 30°C ambient temperature. **d**, Thermal measurements from 7 AM to 7 PM show relatively consistent values. **e**, averaged temperature data shows day-long trend. **f**, PCR tests show that hourly changes in ambient temperature still allowed for product amplification. For Fig. 2c, d, and e, the red, green, and blue color curves respectively refer to the denaturation, extension, and annealing temperatures measured in the app.

In the field, clouds could manifest in a number of forms that affect PCR efficiency. To examine the influence of clouding in a controlled manner, we designed a solar simulator using a 100 W LED. Optical lenses were set up to collimate the light and create similar temperatures on the chip. To mimic clouding, the light was blocked 5 min after the PCR process began for a duration that ranged from 15 s to 4 min. The resulting thermal profiles are shown in Fig. 4.3a. The DNA melting temperature of 86°C, calculated using the nearest neighbor method, served as a

threshold for the denaturation step to define the percent of time that the sample spends below acceptable conditions for PCR. These were calculated to range from 2% (15 s light obstruction) to 33% (4 min light obstruction) for tests with a total flow-through time of 27 min. The band intensities shown in Fig. 4.3b, c suggest an exponential decay as the duration of simulated clouding increases. Details on the LED setup are available in Supplementary Information.

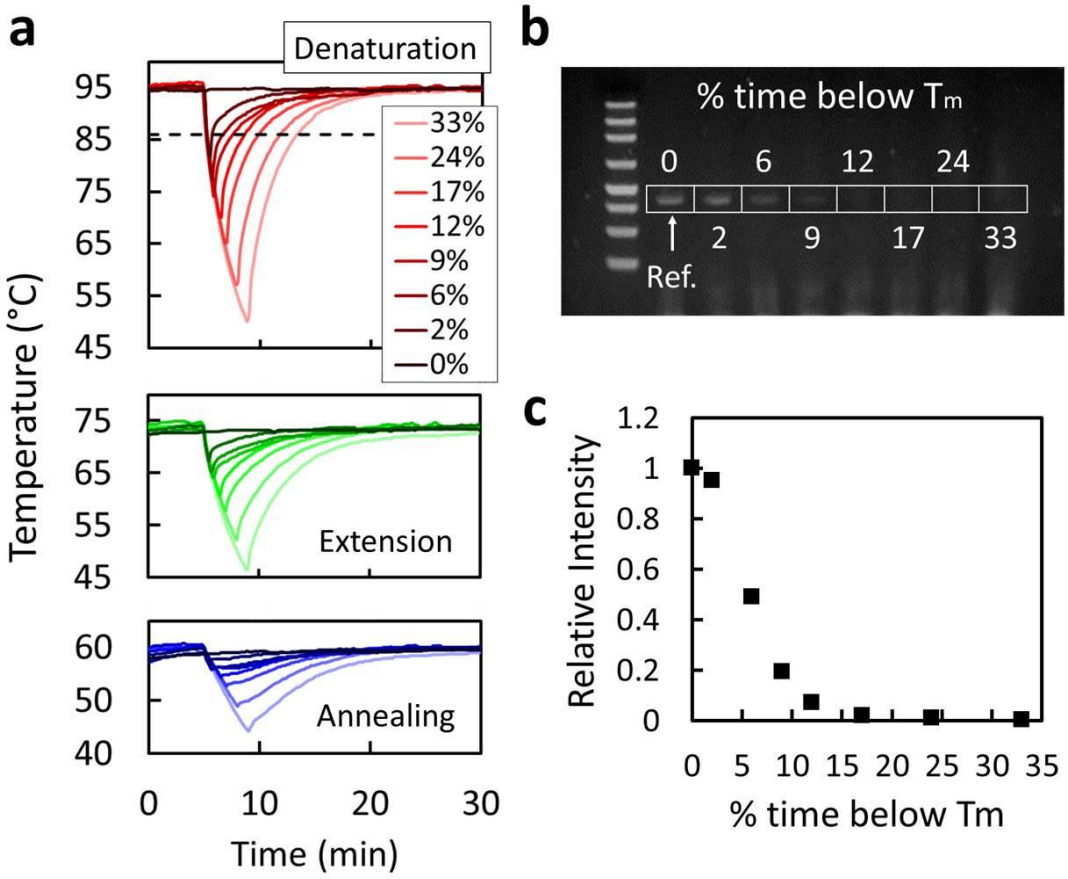

Fig. 4.3. Characterization of simulated cloud coverage and flow rate. a, temperature variation for denaturation, extension and annealing due to blocking of the light. Simulated clouding times ranged from 0 s (darkest curve) to 4 min (lightest curve) for a total test time of 27 min. The percentages represent the percent of time that each test spent in non-ideal PCR conditions, which for these tests was defined as when the denaturation temperature dropped below the dashed line. **b**, gel electrophoresis and **c**, corresponding band measurements show diminishing intensities as a function of the duration of simulated cloud coverage.

4.3.3 Sample-to-answer analysis of human skin biopsies

To demonstrate compatibility with solid tissue processing in the absence of specialized equipment, we analyzed human skin biopsies both with and without KS involvement by combining solar thermal PCR with single-tube HotSHOT[30] DNA extraction and smartphone fluorescence detection. Fig. 4.4a shows a smartphone-powered blue LED incident on a PDMS chip containing 4 samples. Each sample includes SYBR Green dye, which preferentially binds to double-stranded DNA and emits green light when excited by blue light. The chip shown in Fig. 4.4a, b contains samples processed from two KS biopsies (1, 2), a skin biopsy with mycosis fungoides but without KS (3), and a negative control (NC). Samples 1 - 3 were mixed with dry room-temperature PCR reagents and primers and amplified by solar thermal PCR, while NC was mixed with a conventional refrigerated PCR reagent kit and run in a thermal cycler. An app compared the average fluorescent signals of the three test samples to NC, providing the user with the correct diagnosis for each (Fig. 4.4c). In practice, an intensity threshold could be determined based on multiple tests to provide on-site diagnosis. By tracking the battery depletion of the smartphone over a number of PCR tests, we calculate a power consumption of 80 mW, which is two orders of magnitude lower than commercial products (Table 4.S1). For a 5.5 Wh smartphone battery, this would enable a battery life of 70 h, compared to about 15 h for techniques in literature and 1 h for commercial devices.

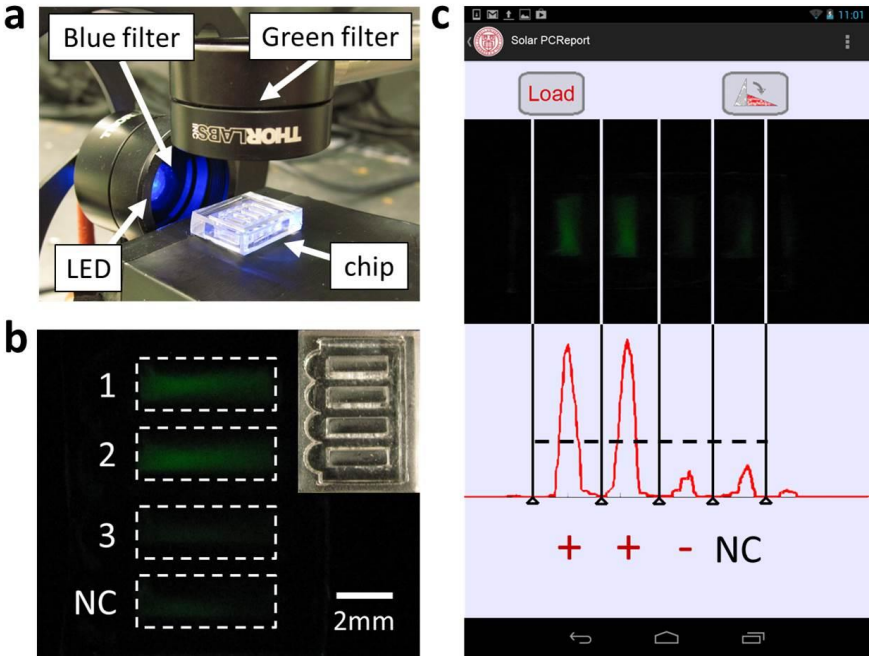

Fig. 4.4. Integration of HotSHOT cell lysis, solar thermal PCR and smartphone-based detection applied to mouse tail biopsies. a, fluorescence detection setup includes a blue filter between the LED and the chip and a green filter between the chip and the camera. **b**, PDMS chip (inset) containing 4 tests: solar thermal PCR performed using KSHV+ samples (1, 2) and a KSHV- sample (3) and traditional PCR using negative control (NC). **c**, a screenshot of the app that analyzes the fluorescence signals, showing high intensities for samples 1 and 2 and low intensities for sample 3 and NC.

4.4 Discussion

Solar thermal PCR as described here supports a number of qualities beneficial to POC nucleic acid based diagnostics. Sunlight-driven DNA amplification removes the power requirements for thermal cycling and enables a 100-fold reduction in power consumption compared to state-of-the-art devices, allowing it to be powered by a smartphone battery for 70 h. Tests can be performed in less than 30 min, potentially enabling rapid diagnostics in regions where long travel distances to clinics make follow-up meetings with patients difficult. The system is also highly efficient in energy conversion and supports minimal infrastructure by removing a

number of electrical components such as microheaters and actuators. We demonstrated DNA amplification under a range of ambient conditions and successfully analyzed human skin biopsies by combining solar thermal PCR with HotSHOT DNA extraction and smartphone-based detection. Compared to battery or solar panel-powered systems, solar thermal PCR offers advantages in power consumption and simplicity without compromising PCR performance. Such a strategy could be developed into an integrated device completely powered by sunlight and a smartphone, leading to greater accessibility of DNA diagnostics in resource-limited settings.

4.5 Methods

4.5.1 PCR sample preparation.

A 70µL volume of DI water containing 4.3% w/v polyvinylpyrrolidone (PVP) (Sigma-Aldrich, 437190) is mixed with PCR reagents (Invitrogen, N8010055) including 10µL of 10X PCR buffer, 0.2-mM dNTPs, 10 Units/100 µL of *Taq* polymerase, 1 µM of forward and reverse primers and 1 µL of target DNA. PVP is used here to inhibit *Taq* adsorption onto the PDMS surface[24,31].

4.5.2 Solar thermal PCR procedure.

The channel was first passivated with a 7.5 mg/mL bovine serum albumin (Sigma-Aldrich, A7888) solution for 2 h to further inhibit *Taq* adsorption, and flushed with DI water at 1 µL/min for 30 min to remove unbound particles. During the test, a 20µL paraffin oil plug (VWR, BDH3338) was pumped through the chip, followed by a 10 µL sample, and then another oil plug. The two plugs prevent sample evaporation caused by heating[32].

Unless specified, samples contained an initial DNA concentration of 10^5 copies/μL and tests were conducted with a syringe pump (New Era, NE-1000) set at 1 μL/min. Due to absorption of the oil into the PDMS, the actual flow rate was calculated to be 0.8 μL/min based on the time the samples took to go from the inlet to the outlet.

4.5.3 Sample preparation for smartphone fluorescence detection.

The negative control included 25 μL of *Power* SYBR Green PCR master mix (Invitrogen, 4368577) combined with 15 μL of DI water, 1 μM of forward and reverse primers and 10 μL of KSHV- solution. Tests 1-3 used High Yield PCR EcoDry Premix (Clontech, 639278) mixed with 15 μL of 5% w/v PVP in DI water, 10 Units/100 μL of *Taq* polymerase, 1 μM of forward and reverse primers, and 10 μL of KSHV+ biopsy solution (samples 1 and 2) or KSHV- solution (sample 3). After amplification, 10 μL of the products were added to 10 μL SYBR Green solution and injected into the chambers.

4.6 Acknowledgements

We would like to thank Michael Kalontarov for 3D-printing components of the solar thermal PCR system. This work was supported by the US National Science Foundation through Grant no. NSF-CBET-0846489 ‘‘CAREER: Optofluidics - Fusing Microfluidics and Photonics” and a seed grant for Collaborations Between Cornell University-Ithaca and Weill Cornell Medical College Faculty. M. Mancuso would like to acknowledge a National Science Foundation Graduate Research Fellowship under Grant no. DGE-0707428. This work was performed in part at the Cornell NanoScale Facility, a member of the National Nanotechnology Infrastructure Network,

which is supported by the National Science Foundation (Grant ECS-0335765) and at the Nanobiotechnology Center (NBTC), an STC Program of the National Science Foundation under Agreement no. ECS-9876771.

4.7 Supplementary Information

4.7.1 Benchtop system design

The platforms holding the lens and the microfluidic chip were designed in AutoCAD and 3D-printed (Stratasys, Object500 Connex). The bottom hinge, which allows for 100° rotation of the stage, was machine shopped at Cornell's Laboratory of Atomic and Solid State Physics (LASSP). The assembled system includes: 1x 75 mm lens (Thorlabs, LA1002), 4x cage assembly rod (Thorlabs, SR4), 4x cage assembly rod (Thorlabs, SR05), 4x rod adapter (Thorlabs, SRSCA), 4x thread adapter (Thorlabs, MSA8), 1x breadboard (Thorlabs, MB1015/M), 1x cage rod cross coupler (Thorlabs, S1A), and 1x micrometer head (Thorlabs, 150-801ST).

4.7.2 Microfluidic chip design

The PCR chip is 50 mm in diameter and 5 mm in thickness and is comprised of three parts. The top part holds three thermocouples (Omega, 5TC-TT-K-36-36) placed immediately below the three aluminum foil rings. These are secured in place inside 2 mm of PDMS (10:1 ratio of base to curing agent). The bottom piece contains the absorber layer and the microfluidic channel. The absorber is a mixture of carbon black, PDMS base and PDMS curing agent in a 0.02:1:0.05 weight ratio. This is spin-coated onto a 40 mm diameter glass cover slip (Warner Instruments, 64-1500) at 1800 rpm to achieve a film thickness of 100 µm. A clear 50 µm thick PDMS layer is

spin-coated above the carbon black layer to prevent any potential interactions between PCR reagents in the channel and the carbon black. The microfluidic channel, formed using standard photolithography technique, is plasma bonded to the PDMS above the absorber to enclose the channel. The microfluidic piece is then placed with the top section containing the mask and thermocouples. At this point, the chip is 5 mm thick and 40 mm in diameter. A final 10 mm thick PDMS ring is wrapped around the chip, securing it to the benchtop platform and also providing additional insulation. Because these three pieces are all separate, the microfluidic section is easily replaced after each test.

To make the microfluidic channel, SU-8 2075 photoresist (Microchem) is spun on a silicon wafer at 2200 rpm for 30 s to obtain a 100 µm thick film. The SU-8 is then patterned through a chrome photomask (designed in L-Edit, written with the Heidelberg Mask Writer DWL2000) using an ABM Contact Aligner. Uncured SU-8 is removed using SU-8 developer. PDMS is poured over the SU-8 master to a thickness of 3 mm and cured at 80°C for 2 h. The channel cross section is 100 µm × 100 µm and is 1.2 m in length. As a fluid element passes through the channel, it first encounters an initialization zone near 95°C at the center of the chip of approximately 30 mm in length. It then passes through 35 cycles of the denaturation, annealing and extension zones. Each cycle corresponds to a 32 mm long channel section, which radially spans 10° of space, adding up to 350°. The last 10° is dedicated to a final extension step before the fluid exits.

4.7.3 Microcontroller and app design

The microcontroller includes an Arduino Micro board base (Nexuscyber Electronics, ATmega32u4) and three thermocouple breakout amplifiers (Adafruit Industries, MAX31855K) which are each connected with a K-type thermocouple from the chip. To reduce the noise, a 0.01µf capacitor (AllElectronics Corporation, 103D50) is added across each thermocouple lead. Among the 8 pins of the breakout amplifiers, T+ and T- are used to detect slight changes in voltage between thermocouple leads, while the rest process the reading from the thermocouple and transmit the data through a serial interface. The Arduino Micro reads the serial data from the amplifiers and output it to the smartphone.

The Android app is developed in Eclipse with the plug-in Android Development Tools (ADT) and Android SDK. Coding with Arduino 1.0.5 is required for serial data transmission between the MAX31855K amplifier and the Arduino Micro.

4.7.4 KSHV target selection and primer design

Within the KSHV genome, part of the DNA that codes for vCyclin was chosen as our target sequence. vCyclin and its associated RNA are expressed during both the latent and lytic viral phases[13]. Specific primers for this sequence were chosen using BLAST Primer Design[14], and ordered from Invitrogen (Grand Island, NY). Sequence information can be found in Table 4.S2.

4.7.5 DNA count estimation and plasmid culturing and extraction

For Kaposi's sarcoma, the KSHV DNA count varies from case to case depending on the amount of connective tissue versus cells acquired in a skin biopsy. Approximately 10^6 cells can be

obtained in a 3 mm punch biopsy of skin lesions, and we estimate that on average there is 1 copy of KSHV DNA per cell. Therefore, we assume a typical biopsy to contain 10^6 copies of KSHV DNA.

With the exception of the skin biopsies used in Fig. 4 of the paper, all tests were performed using vCyclin plasmid. In order to get multiple copy of vCyclin plasmid, MAX Efficiency DH5α Competent Cells (Invitrogen, 18258-012) are used for transformation. The transformation procedure is as follows: 1) Thaw competent cells on wet ice. 2) Gently mix cells, then aliquot 100 µL into chilled Eppendorf tubes. 3) Add 1 µL of plasmid to the cells, gently mix by pipetting up and down. 4) Incubate the cells on ice for 30 min. 5) Heat-shock cells for 45 s in a 42°C water bath. 6) Place the cells on ice for 2 min. 7) Add 0.9 mL room temperature SOC Medium (Invitrogen, 15544-034). 8) Shake at 225 rpm, 37°C for 1 h. 9) Spread 50 to 100 µL of this culture on LB plates with 100 µg/mL ampicilin. 10) Incubate overnight at 37°C. After overnight incubation single colonies are picked up and inoculated in 3mL of LB medium containing ampicilin with vigorous shaking at 37°C for 14 to 16 h. After the incubation DNA is extracted using QIAprep Spin Miniprep Kit (QIAGEN, 27106).

4.7.6 Thermodynamics modeling

COMSOL Multiphysics was used to create a 2D rectangular model of the heat transfer inside the PCR chip (Extended Data Fig. 3). Inside the system, we solved for the steady state heat transfer equation

$$0 = \vec{\nabla} \cdot k\vec{\nabla}T + Q \qquad (4.1)$$

where k is the thermal conductivity, T is the temperature and Q is the volumetric heat flux. Axial symmetric boundary condition was applied on the left side, corresponding to r = 0. On the top, bottom and ride sides we applied convective and radiation boundary conditions

$$\boldsymbol{n} \cdot \left(-k\vec{\nabla}T\right) = h(T - T_{ext}) + \varepsilon\sigma(T^4 - T_{ext}^4) \qquad (4.2)$$

Where h is the heat transfer coefficient, T_{ext} is the external temperature, ε is the emissivity, and σ is the Stefan-Boltzmann coefficient.

In the model, this was simplified as three ring-shaped heat sources placed at the same locations as where light passes through the foil rings mask. The placement and dimensions of the rings can be adjusted to support the range of ambient temperatures that is expected for the test. In our design, the rings were placed at $8 \le r \le 9.5;\ 11.5 \le r \le 13; 14 \le r \le 17$, where r is the radius in mm. In the model, this corresponds to heat sources placed at $0 \le r \le 8;\ 9.5 \le r \le 11.5; 13 \le r \le 14$. Using the Beer-Lambert law, we calculated the volumetric heat flux Q generated through the absorber, which is given by

$$Q = \alpha I_f e^{-\alpha z} \qquad (4.3)$$

where α is the absorption coefficient, I_f is the focused light intensity incident on the chip, and z is the depth into the absorber. The absorption coefficient for the PDMS-carbon black mixture was previously calculated[15] to be 0.18 μm^{-1}. The incident light intensity I_f is calculated using

$$I_f = I_0 \left(\frac{1}{1 - L_c/f}\right)^2 \qquad (4.4)$$

where I_0 is the unfocused solar intensity, L_c is the distance between the lens and the chip, and f is the focal length of the lens. The thermocouples and the microchannel are assumed to have negligible effect on the heat transfer in the chip due to their relatively small size compared to the bulk of the system.

4.7.7 LED solar simulator setup

Fig. 4.S5 shows the solar simulator setup. The system includes a kit containing a 100 W white LED, AC driver and lens (Topledlight, BY-HP100WWH, BY-DR100WW) and a cooling fan aluminum heatsink (Topledlight, BY-HS100). We found that the provided lens did not fully collimate the light, and therefore added two additional lenses (Thorlabs, LA1740, LA1238) at 7 cm in front of the LED. The solar thermal PCR system was secured sideways on a translation stage (Thorlabs, LT3) and placed at 20 cm beyond the additional lenses.

4.7.8 Method for power consumption calculation and comparison to state-of-the-art

For characterizing the power consumption we ran experiments using a Galaxy S4 smartphone (9.88 Wh battery capacity) and a Nexus 7 tablet (16 Wh battery capacity). In Table 4.S1, these battery capacities are divided by the power consumption of several academic works and commercial devices to calculate the projected battery life.

We calculated power consumption in our system based on the percentage of battery drained over a series of tests. During these tests the app is opened periodically to monitor the temperatures. On average, for each test (1 sample, 30 min) this resulted in a total of 3 min of

screen time to include thermal measurements and fluorescent detection and 27 min in stand-by. Tests were repeated until 5% of the battery for each device was consumed. For the Galaxy S4, this took about 12 tests (6 h), whereas the Nexus 7 required 15 tests (7.5 h). By dividing the amount of energy used over the time period, we arrived at power consumptions of 80 mW for the Galaxy S4 and 100 mW for the Nexus 7. The maximum number of hours on stand-by reported for the devices is 370 h for the Galaxy S4 and 300 h for the Nexus 7. Thus, we calculate stand-by power consumption values of 27 mW for the Galaxy S4 and 53 mW for the Nexus 7. Therefore, the microcontroller and screen collectively consume around 50 mW, enabling 128 h and 155 h of battery life for the galaxy S4 and the Nexus 7, respectively. The 50 mW power consumption of the app was used to calculate a 74 h battery life for an iPhone 5 (5.45 Wh battery capacity, 24 mW standby power consumption).

The above calculating was performed for one test, however there are advantages to how our system would scale with the number of tests as well. One consideration is in running parallel tests using multiple devices. For traditional machines the power consumption would scale linearly with the number of devices. The advantage of our technique is that one smartphone/tablet can be connected to different PCR systems to measure the temperature. This would mean that if the app is being used continuously for different devices, the stand-by power consumption could be eliminated and that each test may require as little as 50mW. The other way to analyze power requirements is with running multiple tests in one chip. Here our system differs from other devices in that the samples would be run in series within the same channel instead of in parallel in multiple tubes/wells. The power consumption would remain

the same but the total energy required would increase with the number of samples because it would take longer for the samples to pass through the chip. Specifically, the energy consumption would scale linearly with the testing time, and therefore the exact amount of energy required would depend on the sample volume. It may be possible to adapt our system to perform high throughput PCR with small sample volumes, in which case running a number of samples would require a minimal increase in energy.

There is some difficulty in comparing power consumption of our device to that of other systems, with the issue being that the powers reported for the academic works or devices are not applied to perform the same functions. For example, most of the academic works report power consumption for heating alone. The Palm PCR reports power consumption required for PCR, which includes heating and mechanical actuation within the device. In our system we do not need to supply any power for heating, and therefore a strict comparison of heating alone would mean that we completely eliminate power requirements. The 80mW reported in our device includes PCR and fluorescence detection. In addition, although the HotSHOT sample processing was performed using a heater for the experiments in this paper, it only requires heating and could foreseeably also be powered by sunlight – something that we are currently developing. Therefore, one of the advantages of our technique is that the entire sample-to-answer process can be predominately performed by solar thermal energy. For these reasons, we believe the order of magnitude comparison between our system and bench top devices such as the Liat Analyzer is a more appropriate, albeit for now imperfect, analysis.

4.7.9 HotSHOT DNA isolation from tissue samples

The HotSHOT procedure includes two reagents. The first is an alkaline lysis reagent with 25mM NaOH, 0.2 mM disodium EDTA at a pH of 12 prepared by dissolving the salts in water without adjusting the pH. The second is a neutralizing reagent with 40 mM Tris-HCl at a pH of 5 prepared by dissolving Tris-HCl in water without adjusting the pH.

KS and control tissue samples were archival, from the Pathology Laboratory of Weill Cornell Medical College/The New York Presbyterian Hospital, and obtained with proper institutional review board approval. These were stored as fresh-frozen specimens in OCT embedding media. Frozen sections were used to determine involvement by KS by histological examination of an H&E stained slide as well as by immunohistochemistry for KSHV LANA. The specimens used in Fig. 4.4 of the text were skin punch biopsies (3 mm), and the negative control was a skin biopsy with mycosis fungoides but without KS. After collecting the samples in a tube, 75 µL alkaline lysis reagent is added to the samples and heated to 95°C for 30 min. After heating, samples are cooled to 4°C, and 75 µL neutralizing reagent is added to each sample. Following this, 10 µL of the final preparation was mixed with the respective PCR reagents, as detailed in Methods Summary.

4.7.10 Smartphone fluorescent detection setup

A PDMS chip containing 4 chambers was designed to each hold 20 µL volumes of the samples. A cylindrical lens 2 mm in diameter was molded in the PDMS in front of each chamber to focus the incident light. A 3.4 W blue LED (Sparkfun Electronics, COM-08860) was used as the light

source. A blue filter (Thorlabs, FGB25) was placed in front of the LED to reduce light at undesired wavelengths. A green filter (Thorlabs FGV9) is placed above the PDMS chip, perpendicular to the direction that the LED excites the samples. An image of the excited samples is taken in the dark through the green filter. The app then plots the fluorescent signal intensity across each sample, resulting in high peaks for the KSHV+ samples and low peaks for the KSHV- sample and the negative control.

Table 4.S1. Projected battery life of PCR devices using smartphone/tablet battery

Paper/device	Sample volume (μL)	Power Consumption (mW)	# of samples	Sample length (bp)	Battery life (h)		
					iPhone 5[10]	Galaxy S4[11]	Nexus 7[12]
Academic works, power consumption assessed for heating only							
PCR amplification (multiple temperatures)							
Liu *et al.*[1]	0.012	460	1	199	12	21	35
Krishnan *et al.*[2]	15	360	1	191	15	27	44
Wheeler *et al.*[3]	75	370	1	90	15	27	44
Neuzil *et al.*[4]	20	3,000	1	-	2	3	5
Isothermal amplification							
Jenkins *et al.*[5]	25	700	1	-	8	14	23
Smith *et al.*[6]	30	450	1	-	12	21	35
Commercial devices/Pipeline products							
Palm PCR F1-12[7] (Ahram Biosystems, Inc.)	20	5,000	<12	< 2000	1	2	3
*Liat analyzer[8,9] (IQuum, Inc.)	10 - 50	10,000	1	-	0.5	1	1.5
Solar thermal PCR	10	App: 50	1	164	74	128	155
		Stand-by: 24[10] / 27[11] / 53[12]					

Table 4.S2. Probe and Target Sequences for KSHV

Name	Sequence
KSHV Probe 1 (22 bp)	AGGATCTGTTCCACTGCCGCCT
KSHV Probe 2 (22 bp)	ACTGGCTCATTGCCCGCCTCTA
KSHV Target (164 bp)	AGGATCTGTTCCACTGCCGCCTGTAGAACGGAAACATCGCATCCCAATATGCTTGC CAGCTGAGGAACTACCCCACCCGAGTGGGTATCCTGCGGAATGACGTTGGCAGG AACCAACAGCGCACAGCCTGCAGCGCTGATAATAGAGGCGGGCAATGAGCCAGT

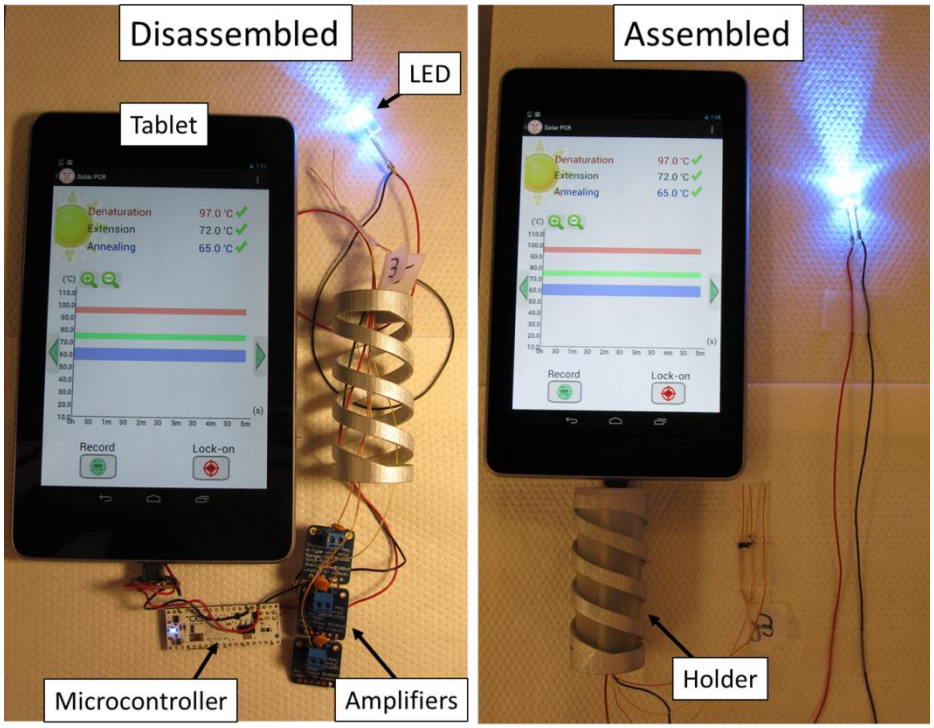

Fig. 4.S1. Disassembled view of electronic components. The electronics include an Arduino Micro microcontroller and three thermocouples amplifiers. A tablet is shown here to power the thermocouple readings during PCR and light a 3.4 W LED for fluorescent detection.

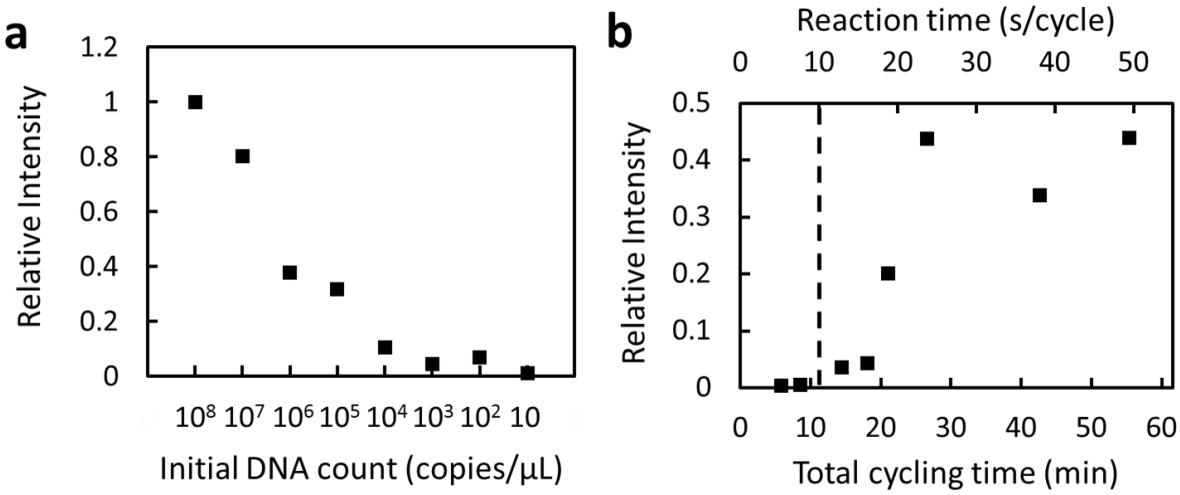

Fig. 4.S2. Measurements of fluorescence intensities. a, data for varying DNA concentrations corresponds to Fig. 1f in paper. **b**, data for flow rate corresponds to Fig. 1g in paper. Dashed line represents the theoretical minimum cycling speed for the extension step.

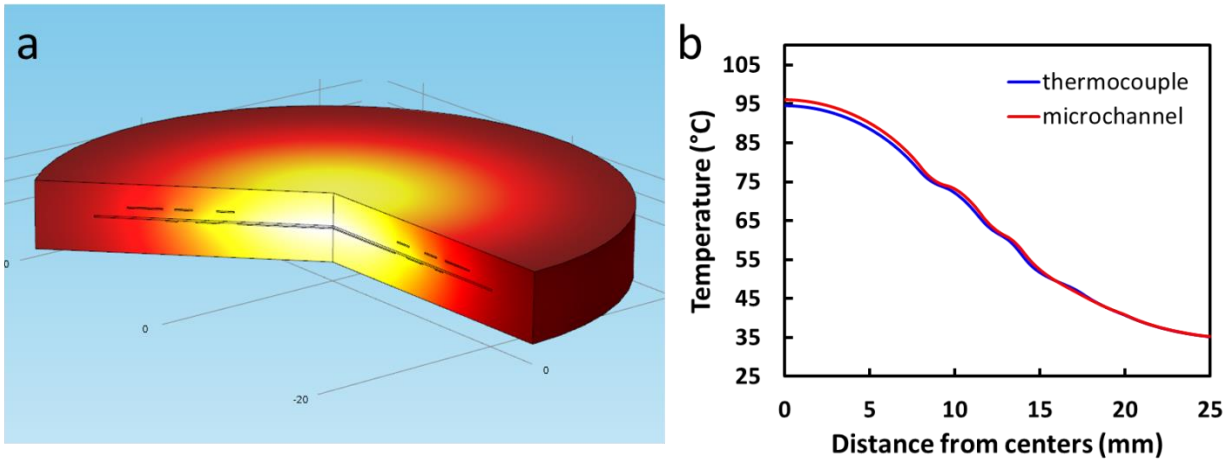

Fig. 4.S3. Comsol simulation of solar thermal PCR chip. a, heat transfer model includes the PDMS, foil mask and glass cover slip. **b**, in our design the thermocouples are 500 µm above the absorber, while the microfluidic channel is 250 µm below the absorber. The plot of temperature values at these two locations show little different, suggesting that thermocouple measurements are adequate for temperature sensing in the channel.

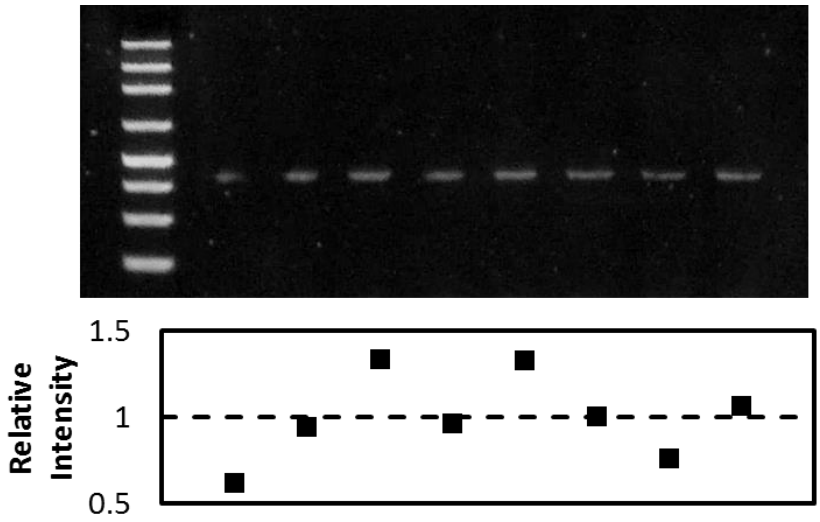

Fig. 4.S4. Analysis of band intensity versus time of day . Gel image is the same as Fig. 2f. Relative band intensities were analyzed using imageJ, with a value of 1 set as the average brightness. It is difficult to discern any particular trend from these tests, although it may be important to note that tests 4 (12:00 PM) and 7 (6:00 PM) could be less bright due to the higher thermal fluctuation associated with those tests, as shown by the larger standard deviation displayed in Fig. 2e.

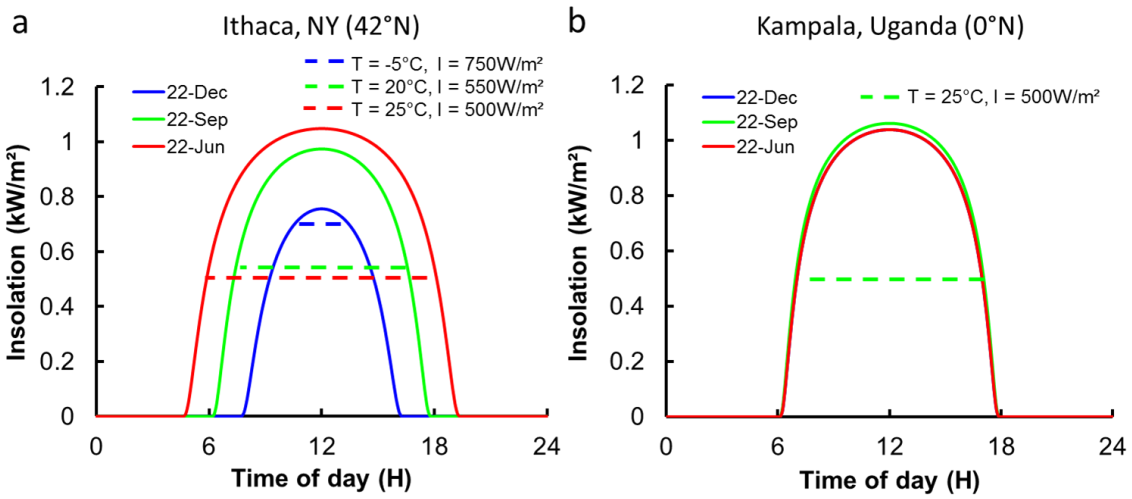

Fig. 4.S5. Availability of sunlight compared to PCR requirements. Insolation values were calculated for the winter solstice (Dec. 22), equinox (Sep. 22) and summer solstice (Jun. 22) for Ithaca, NY (42°N) and Kampala, Uganda (0°N). The average temperatures during each period were used to estimate the minimum solar intensity required for thermal cycling. **a,** in the summer in Ithaca, solar thermal PCR can be powered for about 12 h each day. **b,** in Uganda, where insolation values are much more uniform, solar thermal PCR can be powered for 10 h each day throughout the year.

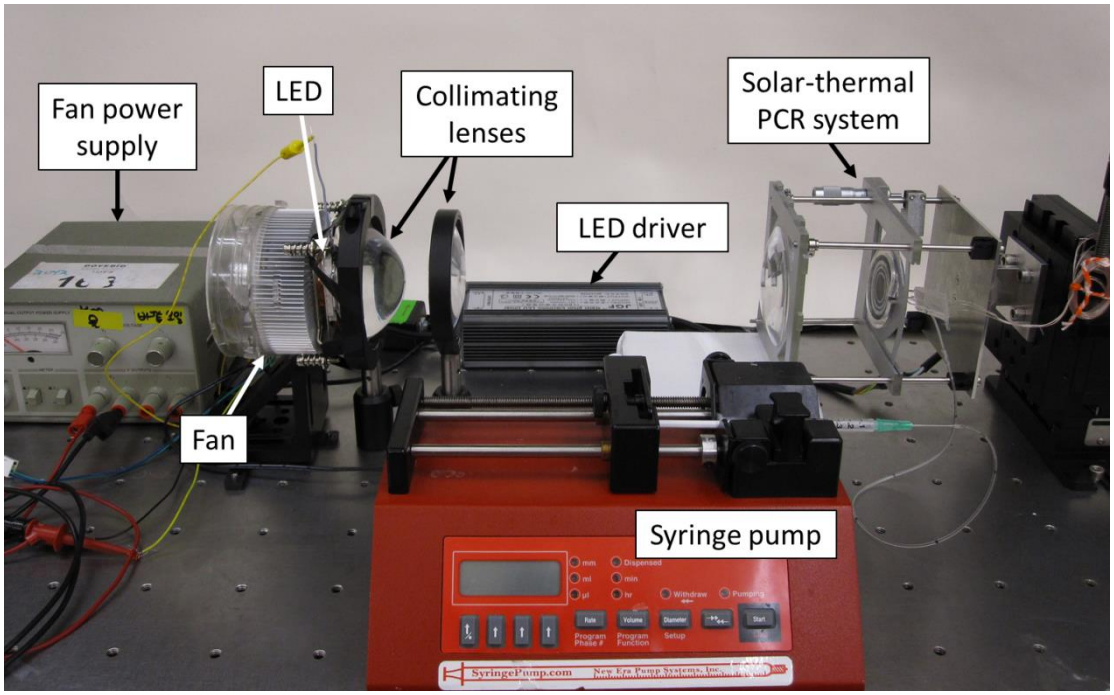

Fig. 4.S6. Solar simulator. The setup includes a 100 W white LED, a cooling fan and aluminum heat sink, and collimating lenses to simulate solar illumination in the lab.

REFERENCES

1 Saiki, R. K. *et al.* Primer-directed enzymatic Amplification of DNA with a Thermostable DNA-polymerase. *Science* **239**, 487-491 (1988).

2 Niemz, A., Ferguson, T. M. & Boyle, D. S. Point-of-care nucleic acid testing for infectious diseases. *Trends Biotechnol.* **29**, 240-250 (2011).

3 Chin, C. D., Linder, V. & Sia, S. K. Commercialization of microfluidic point-of-care diagnostic devices. *Lab Chip* **12**, 2118-2134 (2012).

4 Ahmad, F. & Hashsham, S. A. Miniaturized nucleic acid amplification systems for rapid and point-of-care diagnostics: A review. *Anal. Chim. Acta* **733**, 1-15 (2012).

5 Yager, P., Domingo, G. J. & Gerdes, J. in *Annu. Rev. Biomed. Eng.* Vol. 10 107-144 (2008).

6 Chang, Y. *et al.* Identification of Herpesvirus-like DNA-sequences in AIDS-associated Kaposi's-sarcoma. *Science* **266**, 1865-1869 (1994).

7 Mesri, E. A., Cesarman, E. & Boshoff, C. Kaposi's sarcoma and its associated herpesvirus. *Nat. Rev. Cancer* **10**, 707-719 (2010).

8 Sinfield, R. L. *et al.* Spectrum and presentation of pediatric malignancies in the HIV era: Experience from Blantyre, Malawi, 1998-2003. *Pediatr. Blood Cancer* **48**, 515-520 (2007).

9 Requena, L. & Sangueza, O. P. Cutaneous vascular proliferations. Part II. Hyperplasias and benign neoplasms. *J. Am. Acad. Dermatol.* **37**, 887-919 (1997).

10 A Review of Human Carcinogens: Biological Agents. *IARC Monog. Eval. Carc.* **Vol. 100B**, (2012).

11 Wheeler, E. K. *et al.* Convectively driven polymerase chain reaction thermal cycler. *Anal. Chem.* **76**, 4011-4016 (2004).

12 de Mello, A. J. DNA amplification: does 'small' really mean 'efficient'? *Lab Chip* **1**, 24N-29N (2001).

13 Zhang, C. S., Xu, J. L., Ma, W. L. & Zheng, W. L. PCR microfluidic devices for DNA amplification. *Biotechnol. Adv.* **24**, 243-284 (2006).

14 Gill, P. & Ghaemi, A. Nucleic acid isothermal amplification technologies - A review. *Nucleos. Nucleot. Nucl.* **27**, 224-243 (2008).

15 Craw, P. & Balachandran, W. Isothermal nucleic acid amplification technologies for point-of-care diagnostics: a critical review. *Lab Chip* **12**, 2469-2486 (2012).

16 Chang, C. M. *et al.* Nucleic acid amplification using microfluidic systems. *Lab Chip* **13**, 1225-1242 (2013).

17 Stedtfeld, R. D. *et al.* Gene-Z: a device for point of care genetic testing using a smartphone. *Lab Chip* **12**, 1454-1462 (2012).

18 Maltezos, G. *et al.* Exploring the limits of ultrafast polymerase chain reaction using liquid for thermal heat exchange: A proof of principle. *Appl. Phys. Lett.* **97**, 264101 (2010).

19 Monat, C., Domachuk, P. & Eggleton, B. J. Integrated optofluidics: A new river of light. *Nat. Photonics* **1**, 106-114 (2007).

20 Erickson, D., Sinton, D. & Psaltis, D. Optofluidics for energy applications. *Nat. Photonics* **5**, 583-590 (2011).

21 Tachibana, Y., Vayssieres, L. & Durrant, J. R. Artificial photosynthesis for solar water-splitting. *Nat. Photonics* **6**, 511-518 (2012).

22 Chen, Y. F. *et al.* Optofluidic opportunities in global health, food, water and energy. *Nanoscale* **4**, 4839-4857 (2012).
23 Zhang, Y. H. & Ozdemir, P. Microfluidic DNA amplification-A review. *Anal. Chim. Acta* **638**, 115-125 (2009).
24 Kopp, M. U., de Mello, A. J. & Manz, A. Chemical amplification: Continuous-flow PCR on a chip. *Science* **280**, 1046-1048 (1998).
25 Dorfman, K. D. *et al.* Contamination free continuous flow microfluidic polymerase chain reaction for quantitative and clinical applications. *Anal. Chem.* **77**, 3700-3704 (2005).
26 Schaerli, Y. *et al.* Continuous-Flow Polymerase Chain Reaction of Single-Copy DNA in Microfluidic Microdroplets. *Anal. Chem.* **81**, 302-306 (2009).
27 Krishnan, M. & Erickson, D. Optically induced microfluidic reconfiguration. *Lab Chip* **12**, 613-621 (2012).
28 Han, D., Meng, Z., Wu, D., Zhang, C. & Zhu, H. Thermal properties of carbon black aqueous nanofluids for solar absorption. *Nanoscale Res. Lett.* **6**, 457 (2011).
29 Cai, D. K., Neyer, A., Kuckuk, R. & Heise, H. M. Optical absorption in transparent PDMS materials applied for multimode waveguides fabrication. *Opt. Mater.* **30**, 1157-1161 (2008).
30 Truett, G. E. *et al.* Preparation of PCR-quality mouse genomic DNA with hot sodium hydroxide and tris (HotSHOT). *Biotechniques* **29**, 52-54 (2000).
31 Kim, J. A. *et al.* Fabrication and characterization of a PDMS-glass hybrid continuous-flow PCR chip. *Biochem. Eng. J.* **29**, 91-97 (2006).
32 Wu, W., Kang, K. T. & Lee, N. Y. Bubble-free on-chip continuous-flow polymerase chain reaction: concept and application. *Analyst* **136**, 2287-2293 (2011).

References for Table 4.S1

1 Liu, J., Enzelberger, M. & Quake, S. A nanoliter rotary device for polymerase chain reaction. *Electrophoresis* **23**, 1531-1536 (2002).
2 Krishnan, N., Agrawal, N., Burns, M. A. & Ugaz, V. M. Reactions and fluidics in miniaturized natural convection systems. *Anal. Chem.* **76**, 6254-6265 (2004).
3 Wheeler, E. K. *et al.* Convectively driven polymerase chain reaction thermal cycler. *Anal. Chem.* **76**, 4011-4016 (2004).
4 Neuzil, P. *et al.* Rapid detection of viral RNA by a pocket-size real-time PCR system. *Lab Chip* **10**, 2632-2634 (2010).
5 Jenkins, D. M., Kubota, R., Dong, J., Li, Y. & Higashiguchi, D. Handheld device for real-time, quantitative, LAMP-based detection of Salmonella enterica using assimilating probes. *Biosens. Bioelectron.* **30**, 255-260 (2011).
6 Smith, M. C., Steimle, G., Ivanov, S., Holly, M. & Fries, D. P. An integrated portable hand-held analyser for real-time isothermal nucleic acid amplification. *Anal. Chim. Acta* **598**, 286-294 (2007).
7 *Ahram Biosystems Inc.*, http://www.ahrambio.com/products_palmpcr_F1-12.html (2013).

8 HIV/AIDS Diagnostic Technology Landscape 3rd Edition. *UNITAID,* http://www.unitaid.org/images/marketdynamics/publications/UNITAID-HIV_Diagnostic_Landscape-3rd_edition.pdf (2013).

9 *IQuum*, http://www.iquum.com/products/analyzer.shtml (2013).

10 Apple iPhone 5 – Full phone specifications. *GSMArena*, http://www.gsmarena.com/apple_iphone_5-4910.php (2013).

11 Samsung I9500 Galaxy S4 - Full phone specifications. *GSMArena*, http://www.gsmarena.com/samsung_i9500_galaxy_s4-5125.php (2013).

12 Asus Google Nexus 7 - Full phone specifications. *GSMArena*, http://www.gsmarena.com/asus_google_nexus_7-4850.php (2013).

13 Cai, X. *et al.* Kaposi's sarcoma-associated herpesvirus expresses an array of viral microRNAs in latently infected cells. *P. Natl. Acad. Sci. U. S. A.* **102**, 5570-5575 (2005).

14 Altschul, S. F. *et al.* Gapped BLAST and PSI-BLAST: a new generation of protein database search programs. *Nucleic Acids Res.* **25**, 3389-3402 (1997).

15 Krishnan, M. & Erickson, D. Optically induced microfluidic reconfiguration. *Lab Chip* **12**, 613-621 (2012).

CHAPTER 5

KS-DETECT: A SOLAR-POWERED AND SMARTPHONE INTEGRATED SYSTEM FOR DIAGNOSIS OF KAPOSI'S SARCOMA IN LIMITED RESOURCE SETTINGS

5.1 Abstract

One of the most significant challenges of improving global health is providing high-tech diagnostics to the developing world. With the exception of a few centralized healthcare facilities, most resource-limited regions do not have the infrastructure to support modern healthcare technologies. For people who are not close to such facilities or do not have the means to receive the best available care, they face long delays between developing a disease and receiving treatment, which significantly reduces the chance for survival. In particular, we have focused on Kaposi's sarcoma (KS), an AIDS-related cancer caused by KS herpesvirus (HHV-8). In sub-Saharan Africa, KS is one of the most prevalent cancers and is associated with significant morbidity and mortality in adults and children. In order to provide early near-patient diagnosis, new diagnostic devices must be usable in remote settings, where reliable electricity is rarely available. In such cases, sunlight may emerge as a more practical means to supply the necessary power, not only through solar cells but through solar thermal energy as well. Here we describe development of the KS-Detect system, a portable device that utilizes our solar thermal PCR technique to detect DNA targets. Smartphone technology is significantly integrated into the system, providing temperature reading, flow control, and fluorescence detection capabilities in the field. We have performed preliminary trials using KS-Detect in Kenya and Uganda, and will discuss our findings and future directions for the system.

5.2 Introduction

Kaposi's sarcoma (KS) is a cancer of lymphatic endothelial origin caused by Kaposi's sarcoma-associated herpesvirus (KSHV; also known as human herpesvirus 8 (HHV-8))[1]. The prevalence of KS has increased dramatically since the spread of HIV. For example, in the United States it was estimated that KS incidence increased by a factor of 20,000 to 50,000 for HIV-infected individuals as compared to the general population[2]. Although incidence of AIDS-related KS has declined in developed countries since the implementation of antiretroviral therapies (ARTs)[3], it is still one of the most common cancers in many parts of sub-Saharan Africa[4]. In addition, KS patients in such limited resource settings have very poor survival rates. Data collected in Malawi[5], South Africa[6] and Nigeria[7] for instance report that 25% to 30% of patients died within 1 year of receiving diagnosis, even after ARTs were administered. For regions that do not have access to ARTs, mortality one year after diagnosis increases to 60% to 70%[8,9].

Early diagnosis and treatment are key factors in increasing survivability of KS patients. Although data is limited, studies have found 3- to 5-fold decrease in death rate for patients with T0 stage tumors (KS limited to the skin and/or lymph nodes with minimal oral involvement) as compared to those with T1 stage tumors (extensive oral disease, tumor-associated edema/ulceration, or visceral involvement)[10, 11]. Moreover, it was recently shown that patients with T0 KS treated with combination ART (cART) alone exhibited 5-year survival of over 90% and progression-free survival of 77%[12]. Unfortunately, due to the limited resources of many developing countries, obstacles such as high cost of tests, lack of transportation, loss of contact with patients, miscommunication, and misdiagnosis significantly prolong the time required between initial

diagnosis and treatment. Specifically, a recent study found that pathologists in Kenya and Uganda who only had access to routine H&E staining achieved 72% sensitivity and 84% specificity when assessing skin biopsies for KS[13].

In Chapter 4 I showed how solar energy could be utilized to power PCR for disease diagnostics when traditional sources of power are not available. In order to create a powerful and user-friendly diagnostic platform, however, additional attributes such as a convenient user interface and disease tracking capability would be necessary. Smartphone technology could play a significant role in this, as it contains a number of features that would provide key advantages for diagnostics in limited resource settings. We have outlined some of these advantages in a recent commentary paper[14], which discussed the role of smartphone lab-on-a-chip technologies in application areas of nutrition monitoring and disease diagnostics. Particularly for disease diagnostics, we envision (1) facilitating early-stage diagnosis, (2) maintaining communication and monitoring of patients, and (3) enabling tracking of disease outbreaks to be key benefits that would be brought by smartphone-integrated systems (Fig. 5.1). Therefore, through the integration of sunlight and smartphones, the KS-Detect system utilizes two of the most ubiquitous resources around the world to meet the needs of developing world diagnostics.

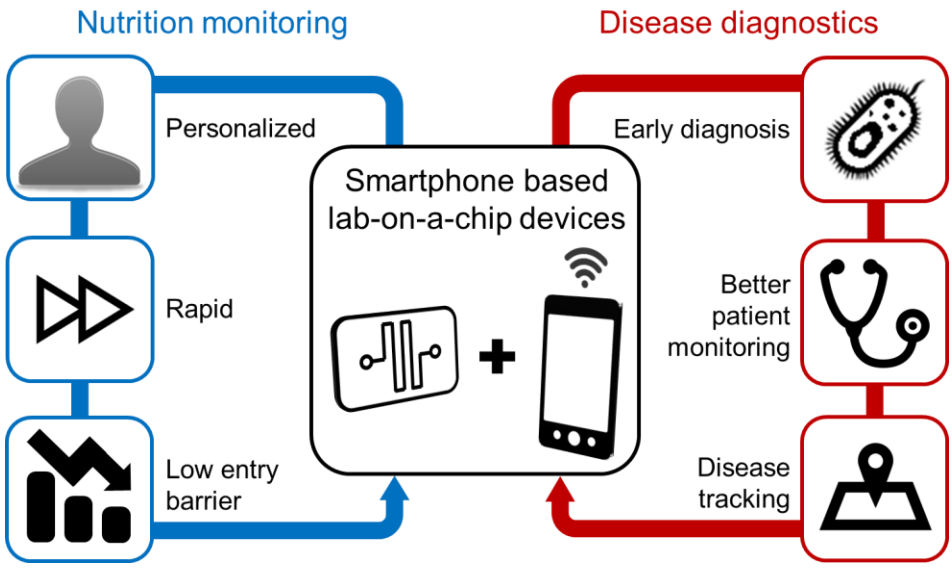

Fig. 5.1. Smartphone based LOC technology could provide a number of important advantages for health monitoring and diagnostics. Key benefits for nutrition monitoring include personalized and rapid care with a low barrier to entry while for disease diagnostics it offers early diagnosis, better patient monitoring, and spatiotemporal tracking capability.

5.3 Results and Discussion

5.3.1 Technical details of the KS-Detect system

In order to provide early and accurate diagnosis of KS and improve survivability of KS patients in developing nations, a diagnostic system must offer several key features, including: portability, accuracy, low cost, system simplicity, durability, rapidity of results, and ability to operate with limited medical infrastructure. We believe the KS-Detect system as described herein meets these requirements. The KS-Detect device is a nucleic acid-based diagnostic tool that provides sample-to-answer analysis of skin biopsies by combining HotSHOT DNA extraction[15], solar thermal PCR for low power DNA amplification[16], and smartphone-based fluorescent detection of the amplified DNA. The system, shown in Fig. 5.1a,b, measures 15 cm x 15 cm x 25 cm and weighs approximately 2 kg. The user follows a protocol to perform each test, illustrated in Fig.

5.1c. Briefly, the procedure consists of 6 general steps: 1. A new microfluidic cartridge is inserted into the device; 2. The solar thermal PCR platform is tilted to face the sun, and solar energy is concentrated through a lens to heat the microfluidic cartridge; 3. The on-chip temperatures are read by a smartphone/tablet device via a custom app. After about 3 min of heating, PCR-appropriate temperature will be reached; 4. The post-HotSHOT sample is then pumped through the system using a micro-pump, which is also controlled by the smartphone; 5. After about 30 min, the sample exits the device and is collected and mixed with SYBR Safe dye; 6. The amplified sample is excited by a blue LED, and the smartphone analyzes the green fluorescence signal to deliver a positive or negative result. Fig. 5.2d shows screenshots of the app and each particular function, including thermal sensing, micro-pump control, and fluorescence analysis.

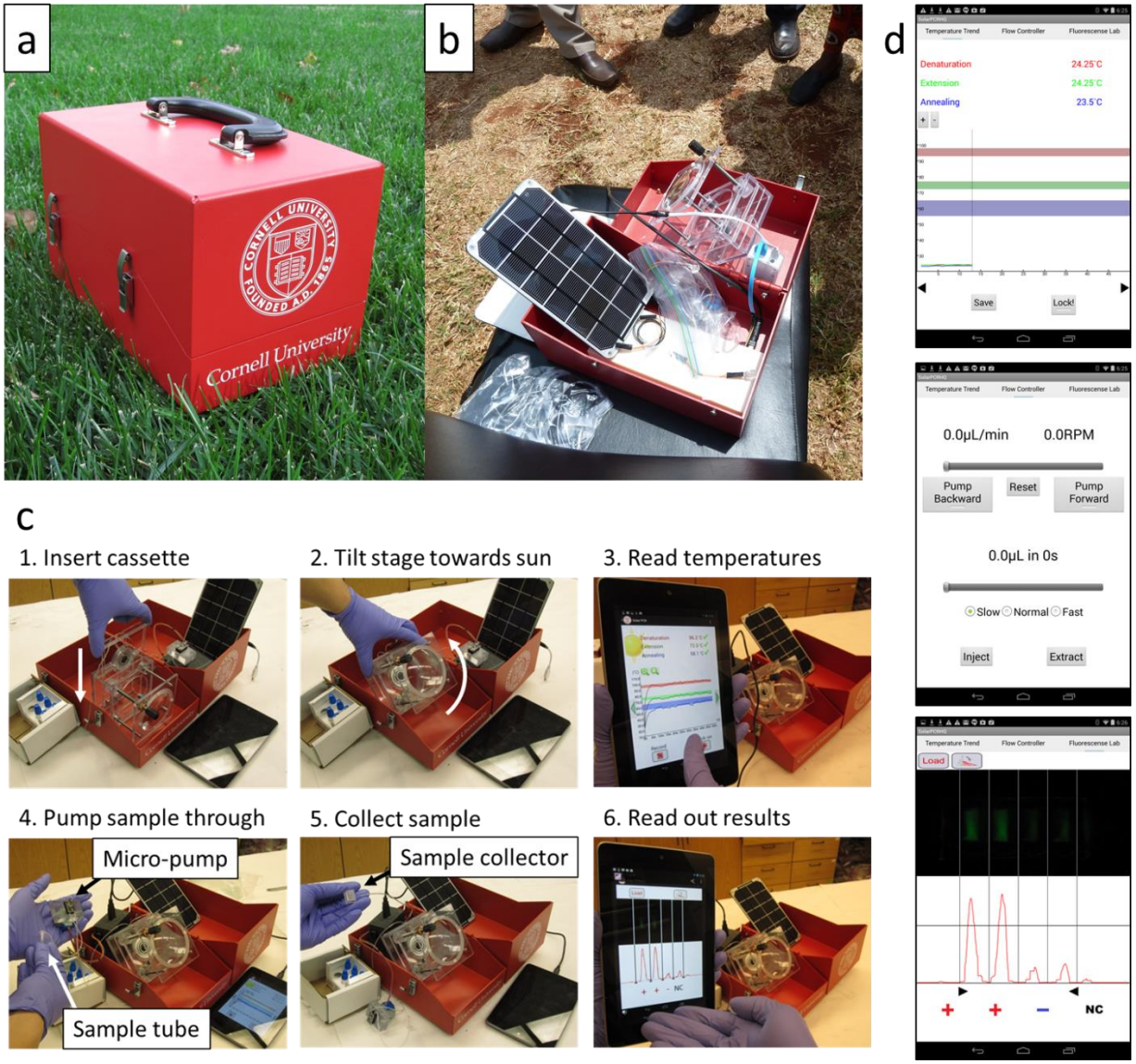

Fig. 5.2. KS-Detect prototype. (a) The system measures 15 cm x 15 cm x 25 cm and weighs about 2 kg. (b) Field demonstration of the device at a local clinic in Kenya. (c) A schematic of the 6-step process for performing a test. (d) The app consists of 3 screens that the user can cycle between, including (top) thermal sensing and recording, (middle) micro-pump control, and (bottom) fluorescence detection.

5.3.2 Preliminary trials in Kenya and Uganda

This device was taken to Kenya and Uganda in February 2014 to perform preliminary field testing. As shown in Fig. 5.3a, we also took an indoors version of the system in case some days

were cloudy. While there, we tested 5 patient biopsies, which are labeled in Table 5.1. The results of test sample 1 are shown in Fig. 5.3b.

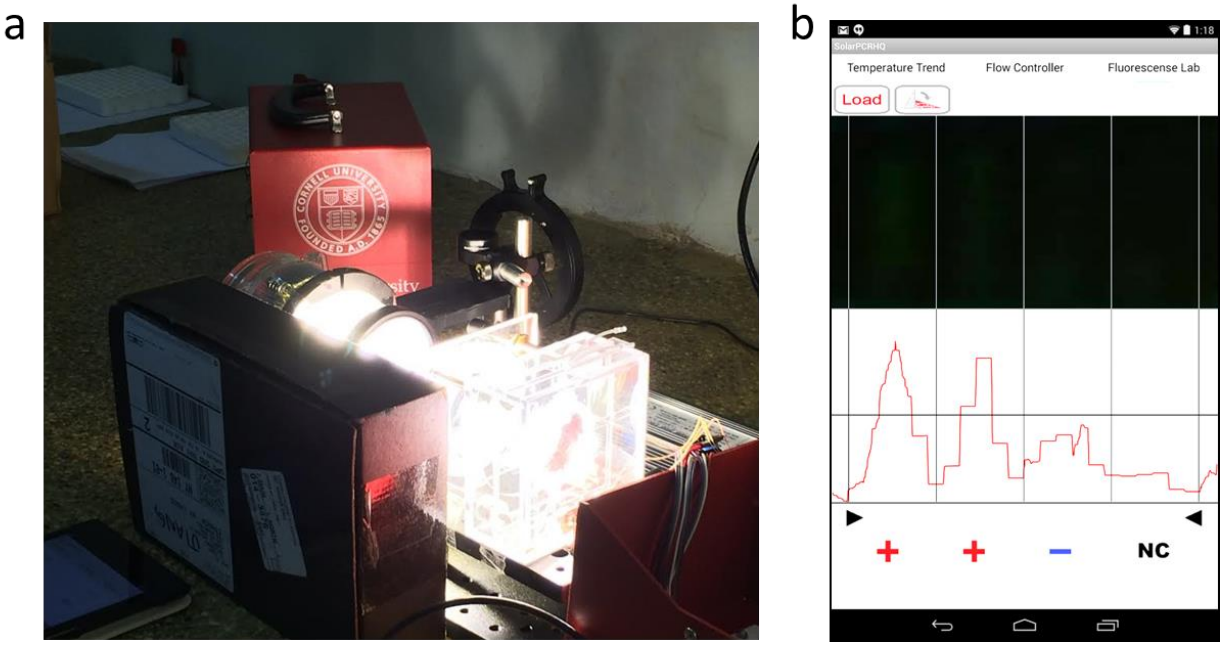

Fig. 5.3. Preliminary results taken in Africa. (a) On cloudy days, the solar simulator was used indoors to run tests. (b) Fluorescence data taken after processing fresh biopsies from patients who came to the hospital on the same day. The leftmost and rightmost samples are the positive and negative controls, respectively. The middle two samples were separate cuts from the same biopsy.

Table 5.1 shows the results of all 5 tests, which fall into 3 categories. As shown in Fig. 5.3b, Sample 1A/1B was inconclusive because we obtained both a positive and a negative result from the same biopsy. Clinical testing determined that the sample was in fact negative for KS. Samples B and N were determined to be positive by both KS-Detect as well as traditional PCR. Unfortunately, I discovered afterwards that the fluorescence signal produced after using KS-Detect was caused by nonspecific binding of non-target DNA. Finally, samples K and S were determined to be negative using KS-Detect, while we have not yet obtained clinical results for

either sample. It turns out that the negative results in these cases were due to the fact that the samples had been fixed in formalin, which prevents HotSHOT from being able to extract any DNA. Thus we did not have the correct means to process these samples for PCR anyway.

Table 5.1 Sample results obtained in Africa

Sample	KS-Detect Result	Clinical result	notes
1A/1B	Inconclusive	Negative	Tissue bisected to form 1A and 1B
B	Positive	Positive	Positive result due to nonspecific binding
N	Positive	Positive	Positive result due to nonspecific binding
K	Negative	Unknown	Fixed in formalin
S	Negative	Unknown	Fixed in formalin

Fig. 5.4 shows gel images of the KS-Detect amplified products for several samples as well as the positive control. As can be seen here, while positive control was done correctly, KS-Detect did not amplify the target DNA when it tested samples B and N but produced nonspecific binding instead. After further study, it was found that the incorrect amplification was likely due to inhibitors within the biopsy, which significantly reduced amplification efficiency even when using a traditional PCR thermocycler. Recent tests have suggested that increasing the amount of *taq* polymerase in the sample could overcome problems caused by the inhibitors, although further analysis must be conducted to determine how significantly the amplification efficiency can be improved.

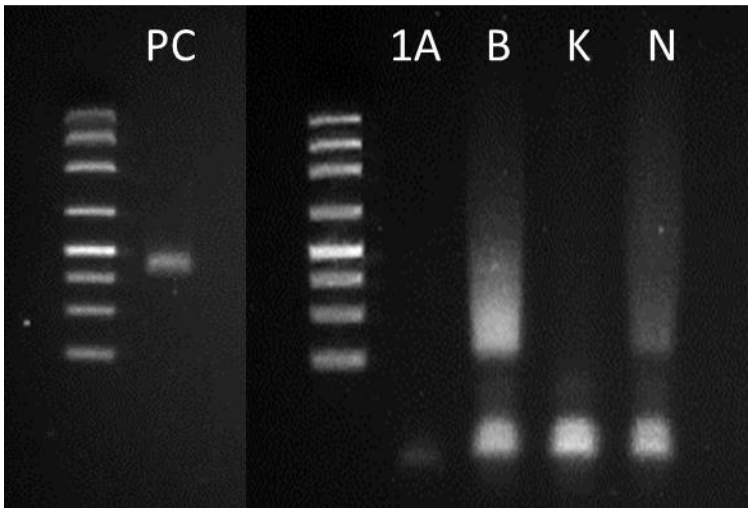

Figure 5.4. Gel images of samples tested in Africa. Although samples B and N are positive for KS, the KS-Detect system did not correctly amplify the target sequence (shown by PC) but instead amplified nonspecific DNA to produce the fluorescence signal.

REFERENCES

1 Mesri, E. A., Cesarman, E. & Boshoff, C. Kaposi's sarcoma and its associated herpesvirus. Nature Reviews Cancer 10, 707-719 (2010).

2 Gallo, R. C. Biomedicine - The enigmas of Kaposi's sarcoma. Science 282, 1837-1839 (1998).

3 Semeere, A. S., Busakhala, N. & Martin, J. N. Impact of antiretroviral therapy on the incidence of Kaposi's sarcoma in resource-rich and resource-limited settings. Current Opinion in Oncology 24, 522-530 (2012).

4 Parkin, D. M. et al. Part I: Cancer in indigenous Africans-Burden, distribution, and trends. Lancet Oncology 9, 683-692 (2008).

5 Makombe, S. D. et al. Outcomes of patients with Kaposi's sarcoma who start antiretroviral therapy under routine programme conditions in Malawi. Tropical Doctor 38, 5-7 (2008).

6 Uldrick, T. et al. Prognosis of patients with AIDS-associated Kaposi's sarcoma receiving antiretroviral therapy +/- chemotherapy in Kwazulu-Natal, South Africa: an analysis of 1-yr survival data from NCT00380770. Infectious Agents and Cancer 4, P41 (2009).

7 Agaba, P. et al. Four year survival in untreated AIDS related-Kaposi sarcoma (AIDS-KS) in Jos, Nigeria. Infectious Agents and Cancer 4, P3 (2009).

8 Olweny, C. L. M. et al. Treatment of AIDS-associated Kaposi's sarcoma in Zimbabwe: Results of a randomized quality of life focused clinical trial. International Journal of Cancer 113, 632-639 (2005).

9 Mwanda, O. W., Fu, P., Collea, R., Whalen, C. & Remick, S. C. Kaposi's sarcoma in patients with and without human immunodeficiency virus infection, in a tertiary referral centre in Kenya. Annals of Tropical Medicine and Parasitology 99, 81-91 (2005).

10 Nasti, G. et al. AIDS-related Kaposi's sarcoma: Evaluation of potential new prognostic factors and assessment of the AIDS Clinical Trial Group staging system in the HAART era - the Italian Cooperative Group on AIDS and Tumors and the Italian Cohort of Patients Naive from Antiretrovirals. Journal of Clinical Oncology 21, 2876-2882 (2003).

11 El Amari, E. B. et al. Predicting the evolution of Kaposi sarcoma, in the highly active antiretroviral therapy era. Aids 22, 1019-1028 (2008).

12 Bower, M. et al. Prospective Stage-Stratified Approach to AIDS-Related Kaposi's Sarcoma. Journal of Clinical Oncology (2013).

13 Amerson, E. et al. Diagnosing Kaposi's Sarcoma (KS) in East Africa: how accurate are clinicians and pathologists? Infectious Agents and Cancer 7, 1-2 (2012).

14 Erickson et al. Smartphone technology can be transformative to the deployment of lab-on-chip diagnostics. Lab Chip (2014) Advanced Article

15 Truett, G. E. et al. Preparation of PCR-quality mouse genomic DNA with hot sodium hydroxide and tris (HotSHOT). Biotechniques 29, 52-+ (2000).

16 Jiang, L. et al. Solar thermal polymerase chain reaction for smartphone-assisted molecular diagnostics. Sci. Rep. 4 (2014).

CHAPTER 6

CONCLUSIONS

6.1 Summary

My research has resulted in the development of a number of novel optofluidic systems that can perform complex tasks without requiring the complex infrastructure that typically plague similar technologies. Laser-activated bubble latching enables the assembly of arbitrary structures that maintain significant flexibility post-assembly through the exploitation of gas bubble dynamics. I have also advanced the concept of solar-based microfluidics through my works in light-controlled flow actuation and solar thermal PCR. These projects demonstrate the potential for future lab-on-a-chip technologies to be able to perform complex, multi-step processes without the need for complex infrastructure or high power demand. When integrated with smartphone technology, such techniques could develop into very powerful yet self-contained and self-sufficient systems for a range of point-of-care applications.

One of the clearest and most immediate directions for this research is in the area of developing world diagnostics, where there is tremendous need for reliable diagnostic tools that facilitate early detection but limited resources prevent many people from accessing adequate care. By combining the ubiquity of both solar energy and smartphone technology, sophisticated biochemical techniques such as PCR could find their way to remote and resource-limited regions of the developing world and provide fast and reliable diagnostics to those who need it the most.

6.2 Future Work

Broadly speaking, fundamental research in the interactions between sunlight and microfluidics could allow sunlight to be utilized in new ways, offering an alternative to batteries and solar panels and reducing the cost and energy burden for many technologies. For example, thermally responsive materials have been used to immobilize DNA and cells[1,2] as well as facilitate drug delivery[3]. Solar based microfluidics could facilitate the creation of solar-powered analogies to these systems, removing the need for lasers, heaters, and complex system design. Water purification is another clear application of this, as both UV radiation and heat have been shown to be effective in water disinfection[4,5] and microfluidics have demonstrated more efficient purification processes than bulk systems[6,7].

Specific to solar thermal PCR, in addition to overcoming the technical limitations that we currently face in terms of amplification efficiency, it is important to create a fully-integrated sample-to-answer system that also bears in mind the needs and capabilities of the end user. For example, although the system seemed in my mind reasonably well-designed when it was used in the lab, running tests in Africa very quickly and very clearly revealed a number of issues such as excessive tubing, inefficient cartridge replacement, and delicate fluorescence detection that would frustrate users who are not familiar with the device. As the technology continues to improve, it is also critical to continue testing in the field and seeking input from those who are on the ground and have an understanding of the fundamental needs and limitations of the developing world. Only in this way can a concept from the lab be implemented to make a difference in the real world.

6.3 Concluding Remarks

There is an incredibly deep well of technological potential that surrounds solar-powered mobile microfluidics. As smartphone technology continues to advance and penetrate deeper into existing markets, the feasibility and utility of such systems will certainly increase as well. Although my work has only scratched the surface of this research area, I believe it has already shown how powerful and impactful such technologies could be. For example, solar thermal PCR alone could transform the diagnostics landscape, as it is a technology platform that if made robust enough can be applied to the detection of any unique nucleic acid signature by simply switching to the appropriate reagents. Continued development of solar-powered mobile microfluidic technologies will help enable practical solutions to some of the greatest engineering challenges we face today.

REFERENCES

1 Krishnan, M. & Erickson, D. Optically induced microfluidic reconfiguration. Lab on a Chip 12, 613-621 (2012).

2 Thilsted, A. H., Bazargan, V., Piggott, N., Measday, V. & Stoeber, B. Flow manipulation and cell immobilization for biochemical applications using thermally responsive fluids. Biomicrofluidics 6 (2012).

3 Qiu, Y. & Park, K. Environment-sensitive hydrogels for drug delivery. Advanced Drug Delivery Reviews 64, 49-60 (2012).

4 Thurston-Enriquez, J. A., Haas, C. N., Jacangelo, J., Riley, K. & Gerba, C. P. Inactivation of feline calicivirus and adenovirus type 40 by UV radiation. Applied and Environmental Microbiology 69, 577-582 (2003).

5 Malato, S., Fernandez-Ibanez, P., Maldonado, M. I., Blanco, J. & Gernjak, W. Decontamination and disinfection of water by solar photocatalysis: Recent overview and trends. Catalysis Today 147, 1-59 (2009).

6 Kim, S. J., Ko, S. H., Kang, K. H. & Han, J. Direct seawater desalination by ion concentration polarization. Nature Nanotechnology 5, 297-301 (2010).

7 Lei, L. et al. Optofluidic planar reactors for photocatalytic water treatment using solar energy. Biomicrofluidics 4 (2010).